PHYSICS AND ENGINEERING OF ORGANIC SOLAR CELLS: ELECTRICAL P-TYPE DOPING WITH PHOSPHOMOLYBDIC ACID

A Dissertation
Presented to
The Academic Faculty

by

Felipe A. Larrain

In Partial Fulfillment
of the Requirements for the Degree
Doctor of Philosophy in the
School of Electrical and Computer Engineering

Georgia Institute of Technology
August 2020

PHYSICS AND ENGINEERING OF ORGANIC SOLAR CELLS: ELECTRICAL P-TYPE DOPING WITH PHOSPHOMOLYBDIC ACID

Approved by:

Dr. Bernard Kippelen, Advisor
School of Electrical and Computer Engineering
Georgia Institute of Technology

Dr. Thomas K. Gaylord
School of Electrical and Computer Engineering
Georgia Institute of Technology

Dr. Azadeh Ansari
School of Electrical and Computer Engineering
Georgia Institute of Technology

Dr. Stephen Barlow
School of Chemistry and Biochemistry
Georgia Institute of Technology

Dr. Carlos Silva
School of Chemistry and Biochemistry
School of Physics
Georgia Institute of Technology

Date Approved: July 6th, 2020

ACKNOWLEDGEMENTS

First, I would like to thank my advisor Dr. Bernard Kippelen for his guidance and constructive feedback throughout these years. I am grateful for the opportunity I was given to work in organic photovoltaics, for the cutting edge equipment and resources he provided and the many educational instances in which he supported me (poster presentations, conferences, seminars, etc.). Through my interactions with him I have become a better researcher, a more rigorous thinker and a better communicator.

Also, I would like to thank my committee members, Dr. Ansari, Dr. Silva, Dr. Gaylord and Dr. Barlow. I appreciate their advice and willingness to serve in my committee.

This work was funded in part by the Department of the Navy, Office of Naval Research Awards No. N00014-14-1-0580 and N00014-16-1-2520, through the MURI Center CAOP, Office of Naval Research Award N00014-04-1-0313, by the Department of Energy through the Bay Area Photovoltaic Consortium under Award Number DE-EE0004946, by the Air Force Office of Scientific Research Award FA9550-16-1-0168 and by CONICYT through the program 'Becas Chile'.

Besides my advisor, committee and funding agencies, I would like to thank current and former group members of the Kippelen group for the countless brainstorming discussions, the feedback, the collegial attitude and the many laughs I had with all of you. In particular, I would like to thank current group member Victor A. Rodriguez-Toro for being a great teammate, a good friend and for introducing me to dancing salsa. Also, I

would like to thank former group member Dr. Vladimir Kolesov. I am grateful for his assistance, training and valuable advice during several years of my Ph.D. Furthermore, my Ph.D. program would have been entirely different without the Principal Research Scientist of the group, Dr. Canek Fuentes-Hernandez. I thank him for his willingness to help, the uncountable insights and feedback he gave me, for sharing his vision about the future of organic electronics and overall, for being not only an invaluable resource to do research but also a good friend.

Also, I would like to thank the many collaborators that contributed to this work, including Dr. Carlos Borca, Dr. Michael Toney and current and former members of the group of Dr. John Reynolds and Dr. Seth Marder.

I take this opportunity to also thank Mr. Frank Lambert, Szilard Liptak and all graduate and undergraduate students I met while working on a project to power a dental and medical clinic in rural Haiti. I cannot say it was easy, but working in that project was life changing. I will never forget the many lessons the project taught me about the impact that even a small amount of power can have in people's lives, or the remarkably transformative force that students can summon if organized together around a positive goal.

I must say that I would not have started nor finished this Ph.D. without the unconditional support of my family. I owe more than I can express to my parents, and I am particularly thankful for their emotional, spiritual and on occasions, financial support. Also, my brother and sisters have been important pillars in my life and I am grateful for their continuous care for me throughout this process.

I would like to finish by expressing my gratitude to a very special woman who was part of my life at the end of my Ph.D. and taught me loads about myself. My deepest gratitude to you, Laura.

This dissertation is dedicated to all of you.

TABLE OF CONTENTS

LIST OF TABLES

LIST OF FIGURES

LIST OF SYMBOLS AND ABBREVIATIONS

μ	Charge Carrier Mobility
1,2-DCB	1,2-Dichlorobenzene
4T	Quarterthiophene
A	Activity Coefficient Term
AM 1.5G	Air Mass 1.5 Global (Irradiance Standard)
BTP-4F or Y6	2,2'-((2Z,2'Z)-((12,13-bis(2-ethylhexyl)-3,9-diundecyl-12,13-dihydro-[1,2,5]thiadiazolo[3,4-e]thieno[2",3'':4',5']thieno[2',3':4,5]pyrrolo[3,2-g]thieno[2',3':4,5]thieno[3,2-b]indole-2,10-diyl)bis(methanylylidene))bis(5,6-difluoro-3-oxo-2,3-dihydro-1H-indene-2,1-diylidene))dimalononitrile
CB	Chlorobenzene
CdTe	Cadmium Telluride
CIGS	Copper-Indium-Gallium-Selenide
CPX	Ground Charge-Transfer Complex
CS	Charge-Separated State
CT	Charge-Transfer State
DOS	Density of States
e	Elementary Charge
E	Energy
EA	Electron Affinity
E_C	Conduction Band Energy Level
E_F	Fermi Level Energy
E_{Fm}	Metal Electrode Work Function
E_g	Energy Gap
EPBT	Energy Payback Time
EQE	External Quantum Efficiency (η_{EQE})
E_V	Valence Band Energy Level
F4TCNQ	2,3,5,6-tetrafluorotetracyanoquinodimethane
F6TCNQ	2,2′-(perfluoronaphthalene-2,6-diylidene)dimalononitrile
FF	Fill Factor
F_n	Quasi Fermi Level Energy for Electrons
F_p	Quasi Fermi Level Energy for Holes
FTIR	Fourier Transform Infrared Spectroscopy
GaAs	Gallium Arsenide
g_C	Density of States in the Conduction Band of an Inorganic Semiconductor
$g_{e\text{-}O}$	Density of States in the Manifold of Electron-Transport Levels of an Organic Semiconductor
$g_{h\text{-}O}$	Density of States in the Manifold of Hole-Transport Levels of an Organic Semiconductor
GIWAXS	2-D Grazing-Incidence Wide-Angle X-ray Scattering

g_V	Density of States in the Valence Band of an Inorganic Semiconductor
HOMO	Highest Occupied Molecular Orbital
HOPG	Highly Ordered Pyrolytic Graphite
ICBA	Indene-C_{60} Bisadduct
IE	Ionization Energy
IEN	Institute of Electronics and Nanotechnology
IP	Ionization Potential
IPA	Ion Pair Formation
IR	Infrared
ITIC	3,9-bis(2-methylene-(3-(1,1-dicyanomethylene)-indanone))-5,5,11,11-tetrakis(4-hexylphenyl)-dithieno[2,3-d:2',3'-d']-s-indaceno[1,2-b:5,6-b']dithiophene
ITO	Indium Tin Oxide
J_{Max}	Current Density at Maximum Power
J_{SC}	Short Circuit Current Density
k	Wavenumber
k_B	Boltzmann constant (8.617 x 10^{-5} eV K^{-1})
k_{CS}	Generation Rate of Charge-Separated States
k_{CT}	Generation Rate of Charge-Transfer States
LCOE	Levelized Cost of Electricity
LED	Light Emitting Diode
LUMO	Lowest Unoccupied Molecular Orbital
m^*	Effective Mass of a Fermion
MCF	Material Characterization Facility
MeO-TPD	N,N,N',N'-tetrakis(4-methoxyphenyl)-benzidine
NFPA	National Fire Protection Association
n_I	Density of Holes in the Conduction Band of an Inorganic Semiconductor
NMR	Nuclear Magnetic Resonance
n_O	Density of Electrons in the Manifold of Electron-Transport Levels of an Organic Semiconductor
N_{Ph}	Photon Flux Density
OPV	Organic Photovoltaic Device
OSC	Organic Semiconductor
P3HT	Poly(3-hexylthiophene-2,5-diyl)
PBDB-T or PCE12	Poly[(2,6-(4,8-bis(5-(2-ethylhexyl)thiophen-2-yl)-benzo[1,2-b:4,5-b']dithiophene))-alt-(5,5-(1',3'-di-2-thienyl-5',7'-bis(2-ethylhexyl)benzo[1',2'-c:4',5'-c']dithiophene-4,8-dione)]
$PC_{71}BM$	[6,6]-Phenyl-C71-butyric acid methyl ester
PCDTBT	poly[N-9'-heptadecanyl-2,7-carbazole-alt-5,5-(4',7'-di-2-thienyl-2',1',3'-benzothiadiazole)]
PCE	Power Conversion Efficiency
PEDOT:PSS	Poly(3,4-ethylenedioxythiophene) polystyrene sulfonate
PEIE	Polyethylenimine Ethoxylated

PffBT4T-2OD (PCE11)	Poly[(5,6-difluoro-2,1,3-benzothiadiazol-4,7-diyl)-alt-(3,3’’’-di(2-octyldodecyl)-2,2’;5’,2’’;5’’,2’’’-quaterthiophen-5,5’’’-diyl)]
p_I	Density of Holes in the Valence Band of an Inorganic Semiconductor
P_{In}	Optical Input Power
PMA	12-Molybdophosphoric Acid Hydrate
p_O	Density of Holes in the Manifold of Hole-Transport Levels of an Organic Semiconductor
POM	Polyoxometalate
PTA	Phosphotungstic Acid Hydrate
PTB7	[[4,8-bis[(2-ethylhexyl)oxy]benzo[1,2-b:4,5-b']dithiophene-2,6-diyl][3-fluoro-2-[(2-ethylhexyl)carbonyl]thieno[3,4-b]thiophenediyl]]
PTFE	Polytetrafluoroethylene
PV	Photovoltaics
RRa	Regiorandom
RRe	Regioregular
S_0	Ground State
S_1	Singlet Excited State
Si	Silicon
SIMS-ToF	Secondary Ion Mass Spectrometry Time-of-Flight
SLAC	Stanford Linear Accelerator Center
T	Temperature
T_1	Triplet Excited State
UNFCC	United Nations Framework Convention on Climate Change
UV-Vis-NIR	Ultraviolet, visible and near infrared spectroscopy
V_{Max}	Voltage at Maximum Power
V_{OC}	Open Circuit Voltage
WF	Work Function
XPS	X-Ray Photoelectron Spectroscopy
ΔF^0	Helmholtz Free Energy
ΔU^0	Activation Energy of a Process
λ	Wavelength
σ	Electrical Conductivity

SUMMARY

Variations to a solution-based technique to electrically *p*-type dope conjugated polymer films using 12-molybdophosphoric acid (also referred to as phosphomolybdic acid or PMA) are reported and applied to simplify the fabrication of organic photovoltaic devices.

From an engineering perspective, solution-based electrical *p*-type doping using PMA was improved by making the doping solution stable in air while keeping its ability to produce electrical *p*-type doping profiles down to a limited depth from the surface of organic semiconducting films. Furthermore, degradation studies reveal a superior stability of organic photovoltaic devices doped using the updated method, compared to devices fabricated using the original technique. Last, the scope of applications of the method was extended by making it compatible with state-of-the-art conjugated polymer films.

Engineering advances on the application of PMA doping to organic photovoltaics were supported by basic science studies that contributed to improve the understanding of the doping process. First, ^{31}P NMR and FTIR experiments indicate that the Keggin structure of PMA appears to be preserved throughout the doping process. Next, morphology studies on PMA doped P3HT films using GIWAXS along with UV-Vis-NIR spectroscopy and sheet resistance measurements in regioregular and regiorandom P3HT films suggest that PMA dopes both crystalline and amorphous phases and, while it alters P3HT crystals, it causes no distortion to the π-π stacking.

Last, the apparent solvent-dependent nature of the original doping technique was investigated. To this end, the free volume of conjugated polymer films and its role in solution-based electrical *p*-type doping using PMA were studied. Results show that increasing free volume is important to provide enough diffusivity for the PMA Keggin structure to penetrate into the polymer film. The infiltration of dopant and solvent molecules into the available space of these films provides a possible explanation to the previously observed solvent dependency of the technique. As such, the effectiveness of PMA doping critically depends on a charge transfer process, as evidenced in previous work, but also on the available free volume of the conjugated polymer film, as reported here.

No fundamental limit was found pertaining the application of this method to emerging conjugated polymers and bulk heterojunctions of state-of-the-art organic photovoltaic devices.

CHAPTER 1. INTRODUCTION

1.1 Organic Photovoltaics: Value-Added Renewable Energy

1.1.1 Renewable energies to satisfy the global energy demand

The total energy consumption of the world is expected to increase to ca. 160 PWh (that is, 160 10^{15} Wh) by 2050, as outlined in the 2018 edition of the World Energy Outlook (Figure 1-1) [1]. Yet, there are many ways to transform the current global energy system to address such demand. A growing body of research concludes that decarbonization followed by electrification of the global energy infrastructure is a least-cost pathway to a thriving sustainable economy [2].

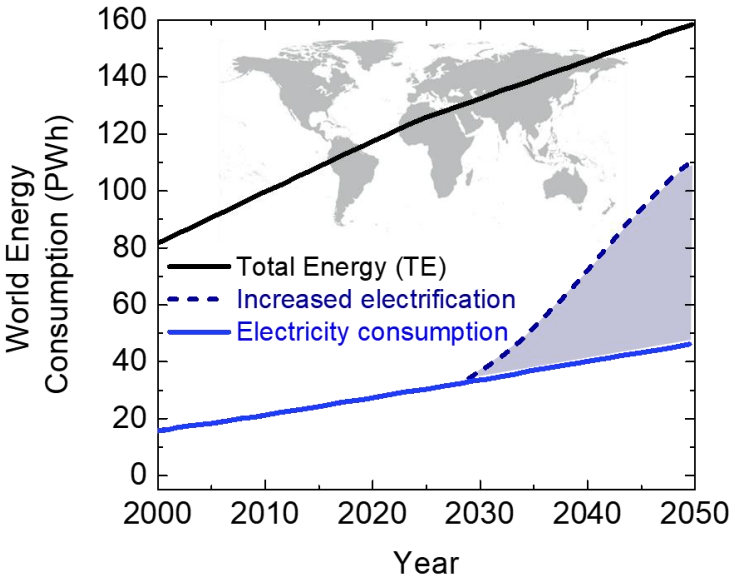

Figure 1-1. Sustained Development v/s New Policies Scenarios, World Energy Outlook 2018 [1].

On the one hand, decarbonization is required for the global energy system to become sustainable. While current energy production is dominated by non-renewable fossil-based sources [1], future economic growth is expected to incorporate sustainable energy sources, especially considering the increasing impact of climate change throughout society. As of 2020, within the United Nations Framework Convention on Climate Change (UNFCC), 189 countries have ratified the agreement made in Paris in 2015 to limit mean global warming below 2 °C above pre-industrial levels [3].

On the other hand, electrification of almost all parts of the energy system along with increased penetration of renewable energies could promote economic growth in both urban and rural areas [2]. Yet, increased electrification requires: (1) from the consumption side, to adopt electricity-based technologies in heating, transportation, desalination and industrial sectors, and (2) from the generation side, to supply 'clean' (that is, as low as possible greenhouse gas emissions) and cost-competitive electricity. An electricity generation technology that may meet these requirements is solar photovoltaics (PV).

1.1.2 Photovoltaics: cost-competitive electricity

Historically, large-scale deployment of photovoltaics was held back due to non-competitive price of PV electricity, compared to other electricity generation technologies. This is no longer the case. As of 2020, the levelized cost of electricity (LCOE, that is, the net present cost of electricity generation by a power plant over its lifetime), produced using solar photovoltaics is either comparable or lower than utility-based electricity in most relevant electricity markets of the world (Figure 1-2). This is partly a consequence of the

reduction in the global average price of photovoltaic modules, larger than two orders of magnitude in the last 40 years [4].

The ubiquitous nature of the solar resource along with competitive capital and operational expenditures of photovoltaic plants have propelled their deployment all over the world. Global installed capacity of photovoltaic modules exceeded 500 GW in 2018, and these numbers are projected to double by 2023 [2]. As a consequence, PV may become a key contributor to all segments of the global energy system in the next 30 years.

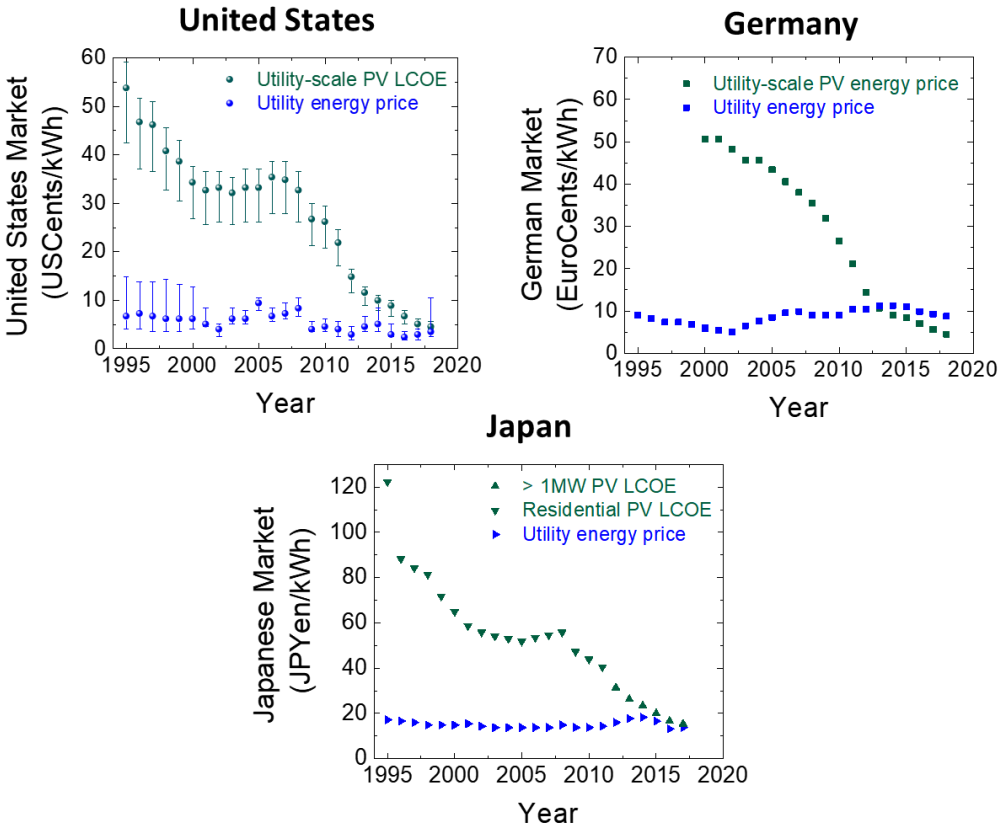

Figure 1-2. LCOE of PV electricity compared to utility-based electricity in the USA, Germany and Japan electricity markets. Error bars in the USA electricity market account for states variability, with the least-cost and highest-cost electricity [1].

1.1.3 Photovoltaic technologies

Photovoltaic solar energy conversion can be traced back to the photogalvanic effect, which was first observed by Edmond Becquerel in 1839 while experimenting with an electrolytic cell consisting of two metal electrodes placed in an electricity-conducting solution [5, 6]. Then, in 1876, William Adams and Richard Day observed the photovoltaic effect in selenium [7]. Yet, it was not until 1954 when Daryl Chapin, Gerald Pearson and Calvin Fuller at Bell labs discovered the silicon-based *p-n* junction solar cell [8]. Besides the LCOE, power conversion efficiency or PCE is another important metric for this technology. It corresponds to the ratio between incoming optical power and output electrical power, and it is used to compare different solar photovoltaic technologies. As an example, the silicon solar cell discovered at Bell labs in 1954 had a PCE of 6%.

Today, solar photovoltaic technologies can be categorized as follows:

1.1.3.1 Crystalline silicon (Si)

Silicon corresponds to the dominant utility-scale photovoltaic technology with 95% of the global market as of 2018 and a global average module price of 0.25 USD/W (2018) [2]. In lab-scale devices, monocrystalline Si solar cells have achieved a power conversion efficiency of 26.1%, while multicrystalline Si devices have shown PCEs up to 23.3% [9]. While Si has a band gap energy of 1.12 eV (which is well matched to the solar spectrum), its absorption coefficient reaches only 10^4 cm^{-1} at 500 nm wavelength and decreases to 5 cm^{-1} at 1100 nm wavelength [10]. This translates into at least an order of magnitude increased thickness to absorb global irradiance, compared to direct band gap

semiconductors. The implications of this and other facts on the energy budget of the fabrication process of Si-based photovoltaics will be discussed later on.

1.1.3.2 Direct band gap semiconductors

This category refers to single-junction and multijunction photovoltaic cells fabricated with GaAs and other III-V semiconductors. With PCEs up to 27.8% in single junctions and up to 39.2% using four junctions (not considering concentrators), this photovoltaic technology is the most efficient in converting sunlight into electricity [9]. Yet, their cost, weight and other features have made it impractical to deploy them at large-scale on earth. As such, they have mostly been applied to space exploration.

1.1.3.3 Inorganic thin film technologies

This category refers to photovoltaic cells and modules fabricated with inorganic alloys such as cadmium telluride (CdTe, 22.1% lab-scale PCE record), copper-indium-gallium-selenide (CIGS, 23.4% lab-scale PCE record), and other [9], with modules in production that have power conversion efficiencies in the 10-18% range. While the toxicity of cadmium, selenium and other key components of these products require vendors to offer the service of module disposal at the end of their lifetime, the product is competing directly against manufacturers of Si photovoltaic modules for utility-scale market share. In fact, the company FirstSolar claims to have PV modules in production with W/kg, temperature coefficients, spectral response and partial shading response comparable or better than crystalline silicon solar modules [11].

1.1.3.4 Emerging technologies

This category refers to cells and solar photovoltaic modules fabricated using quantum dots (16.6% lab-scale PCE record), metal-halide perovskites (25.2% lab-scale PCE record) and organic photovoltaics or OPVs (17.4% lab-scale PCE record) [9].

As of 2020, the application space of these solar photovoltaic technologies remains unclear. While they could be used in utility-scale energy production or space exploration, some of these technologies have particular features that make them uniquely suited for a wider application space. In what follows, such technology features and potential application space will be discussed for the case of organic photovoltaics.

1.1.4 Potential applications for organic photovoltaics

Figure 1-3. Potential applications for organic photovoltaic devices [12-16].

Organic photovoltaic devices are a type of solar cell that contains solid-state organic semiconducting materials placed in between two electrodes, for electron and hole collection [17]. Depending upon the composition of their photoactive layer, they may be

further categorized as either ‘small molecule’ OPVs (if such molecules have well-defined molecular weights) or ‘polymer’ OPVs (which contain organic materials with varying molecular weights made of repeating monomer units). OPVs have gained significant attention from the scientific community because:

a. Since 2015, the advent of new organic semiconducting materials has enabled the demonstration of lab-scale OPV devices with PCEs up to 17% [9].
b. Organic photoactive materials have optoelectronic properties that can be tailored through chemical synthesis.
c. The fabrication of OPV cells and modules is compatible with roll-to-roll solution processing at room temperature, which may favorably impact the monetary investment to scale up their manufacturing and deployment:
    i. Studies have compared the monetary investment of a GW-scale photovoltaic manufacturing facility depending on whether it is based on silicon or organic materials [18, 19]. If organic materials are used, these studies reveal that the investment could be reduced to one third of what is required to install a silicon photovoltaics manufacturing line with comparable output.
    ii. Another important life cycle metric to evaluate the potential of an energy harvesting device is the time it takes to produce the energy invested during its fabrication. This is called energy payback time (EPBT). Assuming realistic manufacturing conditions, roll-to-roll fabrication processes of organic inks at room temperature may give OPVs an advantage against all other photovoltaic technologies, as indicated in Table 1-1.

d. Organic photoactive materials have absorption coefficients that enable optimal optoelectronic performance at a device thickness between 200 nm and 500 nm, which leads to a product with an estimated areal density of 0.16 kg m^{-2} (in an industrial roll-to-roll manufacturing facility), out of which only 0.03 kg m^{-2} correspond to the OPV module [18].

Table 1-1. Energy payback time of solar photovoltaic technologies [18].

Technology	EPBT (years)
Mono and polycrystalline silicon	1.7-4.1
Amorphous silicon	1.1
GaAs	2.4-5
CdTe	0.7-1.6
CIGS	2.0-2.3
OPV	0.2-4

Given the present status of the technology, OPVs have been suggested to provide renewable energy to various applications (see Figure 1-3):

a. Flexible outdoor surfaces, like the sail of a boat or a wearable product. Given the mechanical flexibility and areal density of the final product, OPVs on such surfaces may provide energy to currently inert surfaces [20].

b. Indoor environments, to produce the electrical power needed to enable the sensing, computing, communication and actuation of self-sustainable interactive devices. In fact, OPVs with a bandgap energy of 1.7 eV have reached maximum PCE values of 26% under 1000 lux of a LED light source. Under this LED illumination, 1000 lux corresponded to 302 μW cm^{-2}, leading to the generation of 79 μW cm^{-2} by the OPV. These levels of energy harvesting might enable self-sustainable devices that require only a few cm^2 to generate sufficient power for wireless communication and computing operations [21, 22].

c. Windows, to offset the energy consumption of buildings. As opposed to installing photovoltaics on a roof, if the photovoltaic product can be incorporated to a window without making it fully opaque, the area available to generate electricity increases at least by an order of magnitude. Furthermore, it has been suggested that OPVs could produce a color wheel of architecturally-aesthetic varieties [23].

d. Stand-alone power systems in rural areas. For example, currently ca. 600 million people living in Africa have no access to electricity. This segment of the population relies on dangerous and polluting fuel-based energy sources. Furthermore, the power generation infrastructure signature of developed nations will most likely never be installed because African economies are mostly unable to sustain high capital expenditures with 15-20 years return on investment. Thus, shatter proof and lightweight OPVs compared to conventional solar photovoltaic technologies may turn into a profitable business if produced at a price affordable by Africans [24].

1.2 Objectives

The goals of this Ph.D. research are to expand on the fundamentals of solution-based electrical *p*-type doping of conjugated polymer films with 12-molybdophosphoric acid (also referred to as phosphomolybdic acid or PMA) nanoclusters, and to apply this knowledge to simplify the fabrication of organic photovoltaic devices, in an effort to push OPV technology closer to the marketplace.

In 2016, a technique was pioneered at Georgia Tech to simplify the fabrication of OPVs through spatially confined solution-based electrical *p*-type doping of organic semiconductors. By producing a profile of *p*-type dopants which remain stable for at least 280 h at 60 °C, PMA doping was shown to favor hole collection over a limited region in OPV devices, similar to a *p*-*i*-*n* inorganic solar cell.

Yet, several challenges remained to be addressed before extending the scope and scale of applications of PMA doping to emerging conjugated polymers and other organic electronic device platforms. First, the technique relied on a solvent that is readily capable of detonation, explosive decomposition or explosive reaction at room temperature and atmospheric pressure. Thus, as long as this solvent was used, its applicability to large-scale fabrication would be limited. However, the effectiveness of PMA doping appeared to be dependent on the choice of solvent, and this phenomenon was poorly understood. Furthermore, a rationale behind the formation of the doping profile was missing, nor it was clear whether the dopant profile could be reproduced in emerging organic semiconducting films.

Therefore, from an engineering perspective, secondary objectives of this work are:

i. To improve the original solution-based doping method by making it stable in air while keeping its ability to produce electrical *p*-type doping profiles down to a limited depth from the surface of organic photovoltaic devices, and

ii. To expand the application space of PMA doping to emerging conjugated polymer films, to make the technique compatible with state-of-the-art OPVs.

Last, from a scientific perspective, secondary objectives of this work are:

iii. To provide a potential explanation to the observed solvent dependency of the technique, and

iv. To identify which other variables may be involved in PMA doping and critically influence the formation of the dopant profile down to a limited depth from the surface of semiconducting films, following PMA doping.

1.3 Structure of the Dissertation

This dissertation is organized as follows:

Chapter 1 discusses the potential of organic photovoltaic technology to provide value-added renewable energy to various applications.

Chapter 2 discusses the fundamentals and state of the art of organic semiconductors, electrical doping and organic photovoltaics, particularly focusing on device physics.

Chapter 3 lists key materials required to conduct the experimental work reported throughout the thesis. Furthermore, it describes the methodology used to fabricate and characterize organic thin film samples and organic photovoltaic devices.

Chapter 4 reports on an air-stable variation of the original PMA doping method to electrically *p*-type dope conjugated polymer films and organic photovoltaic devices.

Chapter 5 reports on the characterization of the morphology of PMA doped P3HT films using grazing incidence wide angle x-ray scattering, UV-Vis-NIR spectroscopy and other electrical characterization techniques.

Chapter 6 discusses the free volume of conjugated polymer films and its role in electrical *p*-type doping with PMA, and reports on two variations of the original PMA doping method that make it compatible with state-of-the-art conjugated polymer films.

Finally, Chapter 7 covers the conclusions of this thesis and suggests future work.

CHAPTER 2. FUNDAMENTALS AND LITERATURE REVIEW

2.1 The Development of Conductive Polymers

Controlled electrical doping of inorganic semiconductors is the foundation of modern electronics as Fermi level engineering enables to fine tune the optoelectronic properties of a semiconductor. While many patents were filed with the US Patent and Trade Office in the 1960's and 1970's on methods to dope inorganic semiconductors, their foundations can be traced decades before. Electrical doping of inorganic semiconductors was first formally developed by John Woodyard and coworkers in late 1940's, per their work on nonlinear rectifiers with doped germanium [25-27].

In the case of electrical doping of conjugated polymers, a significant discovery was made in 1976. Then, H. Shirakawa, A. MacDiarmid, A. Heeger and co-workers discovered that semiconducting polyacetylene can achieve 'metallic-like' conductivity (i.e., $\sigma \in [1, 10^4]$ S cm^{-1}) following exposure to bromine, chlorine or iodine vapors. By means of a four-point probe setup, the conductivity of iodinated trans-polyacetylene was measured to increase from 3.2 10^{-6} S cm^{-1} before iodine vapor exposure to 38 S cm^{-1} after 150 min iodine vapor exposure, all at room temperature. Cis-polyacetylene could reach one order of magnitude higher conductivity than trans-polyacetylene following a similar treatment. These films were stable in air for a few hours if kept at 25 °C. As such, polyacetylene halides were the first demonstration of a new class of organic polymers with electrical properties which could be systematically and controllably varied over a wide range (7 orders of magnitude or more), using what was then referred to as 'chemical doping' [28].

This pioneering work was published in 1977 and contributed to establishing the field of electrically conducting polymers, triggering intense research on doped polyacetylene and other conjugated macromolecules. In fact, the highest electrical conductivity achieved

for doped polyacetylene reached 10^5 S cm^{-1} at room temperature, as demonstrated by Naarman and coworkers in BASF [29]. Furthermore, many other conjugated polymers were studied in their un-doped and doped states. A few relevant examples include the demonstration of *p*-type doping of polyaniline, polypyrrole and polythiophene by IBM San Jose, MacDiarmid, Genies, Kobayashi and many others. Similarly, electron-deficient conjugated polymers were shown to undergo chemical *n*-type doping if exposed to a reducing agent, which as expected, increased their electrical conductivity [30-32].

By 1986, and thanks to breakthrough work conducted by Sato, Elsenbaumer, Wudl and others, these materials were made soluble in common organic solvents [33-35]. This opened a path to achieve room-temperature and solution-processable conducting polymers. 'Plastic' optoelectronic devices including lasers, high-sensitivity organic photodiodes, photovoltaic cells, thin-film transistors and all-polymer integrated circuits were now within reach. In each case, these devices could be fabricated from semiconducting and 'metallic-like' polymers processed from solution. This was critical since it made the fabrication of their active layers compatible with large-area, high-throughput processing methods like doctor blading, slot-die coating or inkjet printing.

2.2 Organic Semiconductors

To understand why π-conjugated organic materials exhibit semiconducting properties it is useful to review their electronic structure using tools from quantum mechanics. The first of such tools is Schrödinger equation, which can be written in its time-independent, non-relativistic version as:

$$\hat{H}|\psi(r_1, \dots, r_n; r_A, \dots, r_N) = E\psi(r_1, \dots, r_n; r_A, \dots, r_N) \quad (1)$$

In this expression, $\widehat{H}$ is the Hamiltonian, E is the total energy and ψ is the wavefunction of a system of particles with n electrons and N nuclei. In particular, the square of the wavefunction $|\psi(r_1, \dots, r_n; r_A, \dots, r_N)|^2$ gives the probability of finding electrons and nuclei at positions $(r_1, \dots, r_n; r_A, \dots, r_N)$.

While Schrödinger equation can be solved exactly for a hydrogen atom, it becomes no longer solvable exactly for larger bodies. Thus, two approximations are made. The first one, the Born-Oppenheimer approximation, assumes that it is reasonable to separate the motion of nuclei from that of electrons, keeping the former fixed in space. One important consequence is the possibility to define potential energy surfaces. While nuclei are now fixed, the problem remains unsolvable exactly as it still involves many bodies. Thus, another approximation is made. The interaction between electrons is replaced by an average interaction between each electron and the mean field due to remaining electrons. This is called the Hartree-Fock approximation.

In the context of the Born-Oppenheimer and Hartree-Fock approximations it is possible to simplify Schrödinger equation. The formula can now be written as a system of *n*-coupled one-electron equations. The solution to this system for a single atom yields wavefunctions and wavenumbers corresponding to each electron. These wavefunctions are referred to as "Atomic Orbitals" (AO). Furthermore, wavenumbers associated to each wavefunction correspond to the energy associated to each orbital. Atomic orbitals can be extended to molecules by linearly combining them, as they are mathematical objects. Such linear combinations of atomic orbitals (LCAO) are known as molecular orbitals (MO).

Molecular orbitals are key to explain why π-conjugated organic materials exhibit semiconducting properties. The explanation arises from analyzing the energy levels of MOs as a function of polyene chain size. First, for a methyl radical -CH_3, the un-hybridized $2p_z$ atomic orbital of the carbon atom becomes a π-molecular orbital of the full molecule.

Then, if two methyl radicals are combined assuming perfect coplanarity, that is, when π and σ levels do not mix, an ethylene molecule forms. If their molecular orbitals combine in a bonding fashion (constructive), then they will form a new π molecular orbital equal to $\pi_A + \pi_B$. However, if they combine in an antibonding fashion (destructive), the new molecular orbital will be $\pi^* = \pi_A - \pi_B$. Following this approach, a butadiene molecule can be described as the linear combination of two ethylene molecules, and this procedure can be extended by induction for larger polyenes.

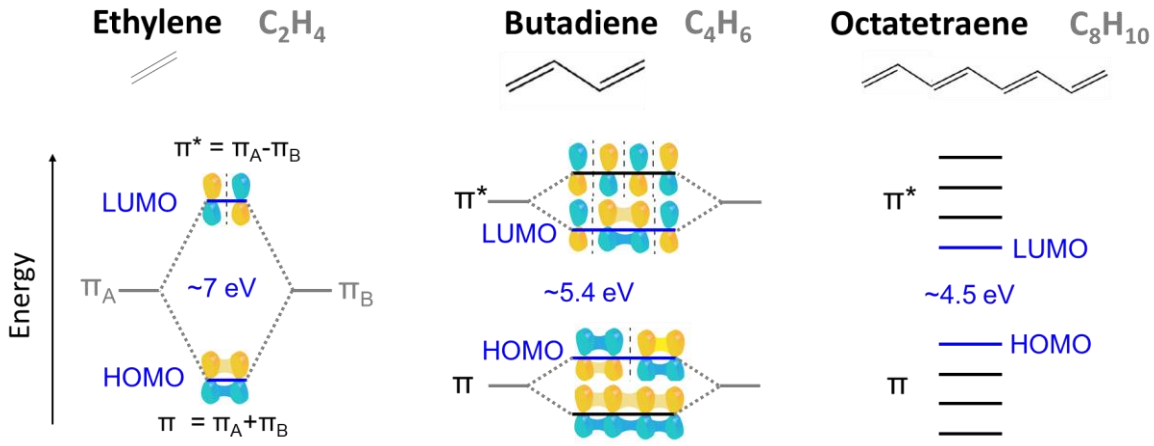

Figure 2-1. Energy of π-molecular orbitals of polyenes as a function of chain size.

As depicted in Figure 2-1, as a function of polyene chain size, two important phenomena occur. First, the energy of the first optical transition comes down as chain size increases. This corresponds to the distance in energy between the lowest unoccupied MO (LUMO or π* molecular orbital with lowest energy), and the highest occupied MO (HOMO or π molecular orbital with highest energy). Second, in an infinitely long conjugated polymer chain, the distance in energy between consecutive π molecular orbitals becomes infinitely small. The same happens with π* molecular orbitals. These phenomena combined enable the appearance of an electronic band structure in large π conjugated molecules like polyacetylene. Thus, such materials exhibit semiconducting properties.

While the π and π* bands of a sufficiently long molecule of polyacetylene correspond to the valence and conduction band of a standard semiconductor, bulk organic π-conjugated solids with an Avogadro number of molecules are hardly just periodic systems with translational symmetry.

Instead, organic π-conjugated materials exhibit a manifold of transport levels close to one another energetically and spatially. Such distribution of localized levels comes from an ensemble of molecules or polymer chain segments, mostly bound to each other through weak Van-der Waals interactions. Impurities due to chemical synthesis or those introduced through processing are abundant, giving rise to additional levels within the transport gap of the material. These levels act as traps for charge carriers and exhibit a large energy difference with respect to the bottom and top of the transport gap (Figure 2-2) [36].

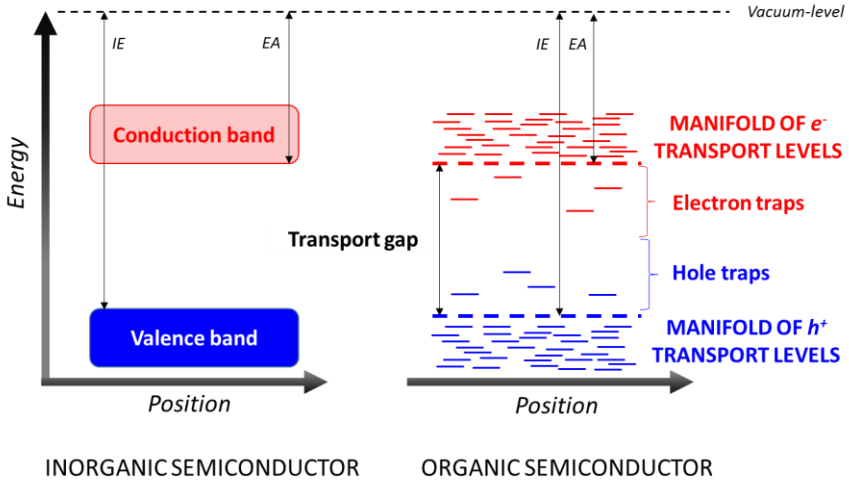

Figure 2-2. Diagram contrasting energy bands of a crystalline inorganic semiconductor to manifolds of transport levels of a non-crystalline organic semiconductor.

2.3 Electrical Doping of Organic Semiconductors

In a doped inorganic semiconductor (e.g., silicon), atoms in the lattice are substituted by an impurity atom, which brings one extra (e.g., phosphorus) or one fewer (e.g., boron) valence electron. These impurities represent new donor or acceptor energy levels "close" to the conduction or valence band (i.e., at a distance in energy that is only a few times k_BT). Therefore, thermal excitation produces highly mobile, delocalized carriers, which leads to controllable changes in electrical conductivity even at low doping ratios, largely retaining the intrinsic charge carrier mobility and crystallinity of the pure host [36].

While the electronic picture for organic π-conjugated systems is very different, as described in 2.2, organic semiconductors can be electrically doped to: (1) increase their electrical conductivity or (2) facilitate charge injection and collection from a metal electrode.

2.3.1 Electrical conductivity enhancement

The increase in electrical conductivity of doped organic semiconductors arises from the addition of charge carriers and their ability to move under the influence of an electric field. Electrical conductivity is:

$$\sigma\left[\frac{S}{cm}\right] = n\left[\frac{1}{cm^3}\right] e[C]\mu\left[\frac{cm^2}{Vs}\right] \quad (2)$$

Since every repeat unit of a conjugated polymer is a potential redox site, these materials may be *n*-type (reduced) or *p*-type (oxidized) doped to a relatively high density of charge carriers *n*. Furthermore, doped films may exhibit increased charge carrier mobility μ compared to their pristine state, for a certain doping level. Dopants contribute to the passivation of deep and shallow trap levels within the transport gap, and free charge

carriers are introduced mostly after such traps are passivated. Yet, an excess of dopant ions may disrupt charge-transport pathways, leading to a decreased charge carrier mobility. As an example, the electrical conductivity as a function of doping level is depicted for an *n*-type electrically doped film of C_{60} (see Figure 2-3, (a)) [37].

2.3.2 Charge injection and/or collection enhancement

Energy level alignment across the interface between a semiconductor and a metal electrode is essential to facilitate charge injection and/or collection. When two materials with different Fermi levels are brought together and let to reach thermal equilibrium, free carriers will flow from one into the other until an equilibrium condition is established (that is, until Fermi levels are flat and equal across the interface). This net carrier flow will set up a positive space charge on one side of the interface and a negative space charge on the other side, which is typically referred to as the "potential barrier". This barrier reduces the ability of carriers to be injected and/or collected from the semiconductor, and appears as a voltage drop in semiconducting devices composed of several semiconductors sandwiched between two metal electrodes (transistors, light-emitting diodes, solar cells, etc.) [38].

Without getting into a detailed description of the phenomena occurring at the interface between metal electrodes and organic semiconductors, it suffices to say that the description of metal-semiconductor interfaces for inorganic semiconductors is applicable for organic semiconductors if the Schottky-Mott law is applicable. This approximation holds for interfaces formed by spin coating polymer films and evaporating organic "small molecules" on metal electrodes, and it also holds for metal-on-polymer surfaces previously passivated by metal species coming from electrical doping (like those relevant to this work). However, it no longer applies to "clean" metal-on-polymer or metal-on-"small molecule" interfaces [39, 40]. These concepts are further discussed in section 2.3.4.

From previous arguments and using a standard semiconductor physics description, it follows that a "good" electrical contact between a metal electrode and an organic semiconductor may be achieved in two ways. One is by matching the work function between the electrode and the organic semiconductor, to reproduce what is referred to as an "ohmic" contact (although the relationship between current and voltage across the interface is not linear). The other is to electrically dope the organic material, to make the potential barrier thin enough for efficient quantum mechanical tunneling. Both approaches are depicted for clarity in Figure 2-3, (b) and (c), when injection and/or collection is desired between a metal and the valence band of an inorganic semiconductor, or a metal and the manifold of hole-transport levels in the organic case [38].

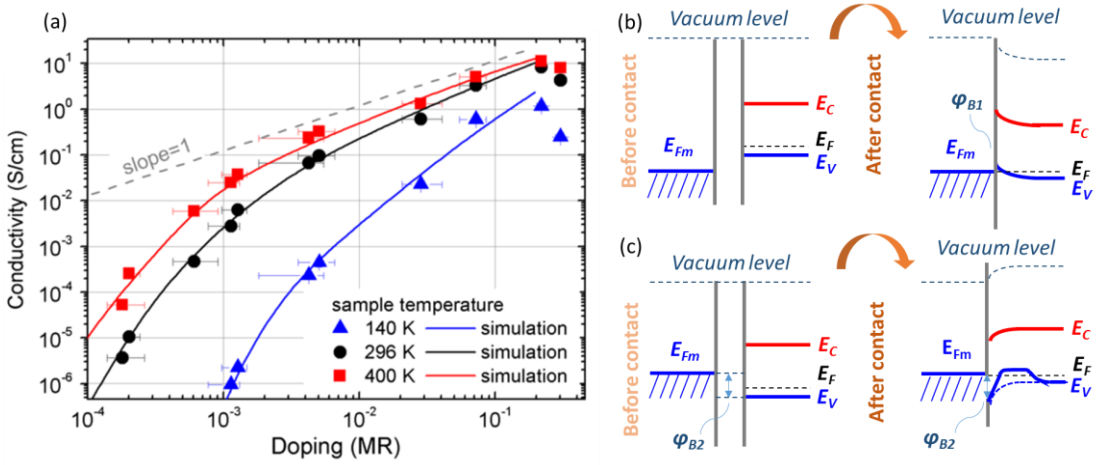

Figure 2-3. (a) Electrical conductivity as a function of doping level for an organic film of C_{60}, directly reproduced from [37]. (b) Energy band diagram across the interface between a metal electrode and a semiconductor, achieving theoretically, 'ohmic' contact to transport holes, without *p*-type doping. (c) Energy band diagram across the interface between a metal electrode and an electrically *p*-type doped semiconductor.

2.3.3 Molecular description of electrical doping of organic semiconductors

As discussed in 2.1, in late 1970's it was shown that exposure of solid films of polyacetylene and other conjugated polymers to I_2 or AsF_5 vapors led to several orders of magnitude increase in their electrical conductivity. However, these films showed poor

thermal stability due to sublimation of dopants at room temperature [41]. Thus, molecular doping emerged as a viable alternative to halides and alkali metals. Larger molecular electron acceptors and donors were developed and used as *p*- or *n*-type dopants on organic, conjugated hosts. Particularly, this section focuses on the case of neutral dopants.

The early notion of doping involves integer charge transference between the dopant molecule and the organic conjugated host if the *EA* of the dopant exceeds the *IE* of the host for *p*-type (this is reproduced in full analogy for *n*-type, assuming IUPAC definition). This mechanism is referred to as 'Ion Pair formation' (IPA) and has been spectroscopically evidenced for various organic semiconductor – dopant systems. In those cases, the absorption spectra of a doped organic film in the UV-Vis-NIR range can be adequately described as the superposition of the absorption features of isolated dopant anions (for *p*-type doping) or cations (for *n*-type doping), and mobile cations (*p*-type doping) or mobile anions (*n*-type doping) along the polymer chain. A prototypical system where these features have been thoroughly studied involves the semiconducting polymer poly(3-hexylthiophene) (P3HT) and the *p*-type dopant 2,3,5,6-tetrafluorotetracyanoquinodimethane (F4TCNQ) [42-44].

From a molecular perspective, the early notion of doping provides a rationale to explain why charge might be transferred between a host and a doping agent. Yet, there are many instances in which the ion pair model does not accurately predict the resulting charge density or even qualitatively describes the doping process. In general, the IPA model is regarded as a model that establishes necessary but not sufficient conditions, since the generation of free holes also requires that the coulombic cation-anion binding is surmounted. For example, IPA fails with MeO-TPD as host (*IP* of 5.00 eV) and F6-TCNNQ (*EA* of 5.60 eV) as *p*-type dopant. Despite the seemingly favourable energetics for efficient transfer of charge carriers between host and dopant, an activation energy of 0.46 eV is required to generate free holes in the MeO-TPD matrix, that is, carriers that are

not coulombically bounded [45, 46]. Another interesting example involves the oligomer quaterthiophene (4T) as host and F4TCNQ as *p*-type dopant. *P*-doped 4T exhibits electronic transitions (per its absorption spectra), that do not coincide with any of the absorption features of 4T cations or F4TCNQ anions [44, 47]. These examples imply that, in general, it is incorrect to assume that all dopants reach a completely ionized state that matches the ion pair formation mechanism.

Another mechanism that leads to mobile carrier density in doped organic semiconductors is the formation of a ground-state charge-transfer complex. From a single-molecule perspective, the frontier molecular orbitals of the host and the dopant hybridize to form a new set of occupied bonding and antibonding orbitals. Since, for example for *p*-type, the HOMO of a host and the LUMO of a dopant do not have to be in resonance, hybridization can occur regardless of the relative energy difference between the host *IE* and the dopant *EA*, although orbital overlap is required, often favoured for flat molecules. This is in direct contradiction to the basic notion of ion pair formation.

The ground-state charge-transfer complex is initially neutral as its bonding orbital, below the *IE* of the host, will be a full level, and its antibonding, above the *IE* of the host, will be empty. A mobile charge might appear if a neutral molecule close to the dopant becomes ionized, turning the charge-transfer complex into an anion, and the host molecule into a cation for *p*-type doping. Ground-state charge-transfer complexes provide a reasonable description of the doping process when charge transfer is fractional. As such, ion pair formation can be considered, conceptually, as the limiting case of a ground-state charge-transfer complex, when electron transfer approaches an integer. Still, it is worth noting that charge-transfer complexes with partial charge transfer require some orbital overlap. On the other hand, some ion pairs involve essentially no orbital overlap. A complete picture, including both ion pair formation and ground-state charge-transfer

complex processes, detailed for both *p*- and *n*-type doping, has been described by Salzmann and co-workers [48].

2.3.4 Review of statistical thermodynamics applied to organic semiconductors

Regardless of whether the doping process occurs dominantly through ion pair or ground-state charge-transfer complex formation (or another molecular description is introduced that more accurately represents the physics or chemistry behind the doping process), electrical doping ultimately modifies the carrier density of an organic semiconducting solid. In other words, it is the overall density of states of the entire organic semiconductor film and its Fermi-Dirac statistics at a certain temperature that which will determine carrier density and consequently, doping efficiency. While a molecular description based on the use of quantum mechanics may prove useful in several situations, an organic thin film contains a number of molecules comparable to that of Avogadro's number. For these many molecules, a rigorous analysis using quantum mechanics quickly becomes unmanageable. Therefore, what follows uses tools from statistical thermodynamics to describe the density of carriers in an un-doped and a doped organic semiconducting film.

2.3.4.1 Thermal equilibrium, Fermi level energy, work function and Fermions

Thermal equilibrium is the condition in which a system is not exchanging energy in the form of heat, work or particle energy between its constituents nor between itself and its surrounding environment. Along these lines, Fermi level energy E_F is defined as the average energy of a particle in thermal equilibrium, in a system with many particles of interest. Finally, fermions are subatomic particles with half-integral spin that follow the Pauli exclusion principle and obey Fermi-Dirac statistics, e.g., electrons [49].

In a semiconductor, the work function $WF = E_{VAC} - E_F$ represents the energy required to free space that prevents an electron at the Fermi level from escaping the solid [50].

2.3.4.2 Fermi-Dirac distribution function for semiconductors

The Fermi-Dirac distribution function is a function that gives the probability of occupation by a fermion of a state with energy E at temperature T. It satisfies three conditions: (a) there can never be more than one particle in the same quantum state per the Pauli Exclusion principle; (b) the probability of occupation depends only on the energy of each particle, and (c) the occupation of states leads to a minimum of free energy at a given temperature T. From purely thermodynamic arguments it can be shown that the distribution for electrons in a semiconductor (organic and inorganic) is [49, 51, 52]:

$$f(E) = \frac{1}{e^{\frac{E-E_F}{k_B T}} + 1} \tag{3}$$

Where k_B is the Boltzmann constant. It is worth highlighting that, since $f(E)$ is the probability of occupation of a state with energy E in the conduction band by an electron, $1 - f(E)$ is the probability of occupation of a state with energy E in the valence band by a hole. Furthermore, if $(E-E_F)$ is larger than $3k_BT$, the Fermi-Dirac distribution for electrons in the conduction band may be approximated as the Maxwell-Boltzmann distribution:

$$f(E) \approx e^{-\frac{E-E_F}{k_B T}} \tag{4}$$

2.3.4.3 Density of states in organic and inorganic semiconductors

According to inorganic semiconductor physics and in first approximation, the density of states in the conduction and valence band can be calculated by solving Schrödinger's equation. This assumes that the semiconductor can be described as a quantum well in which fermions are confined (that is, the potential is finite within a confined region, and infinite everywhere else). In this well, fermions are delocalized and either don't move (*0-D*) or move in *1-D*, *2-D* or *3-D* with an effective mass of *m**. Wavenumbers *k* that are solution to the equation are used to determine the number of available states *N(k)*, and that number is then expressed as a function of energy, *N(E)*, from which the number of states per unit energy and volume is obtained. In a *3-D* quantum well, the density of states for electrons and holes can be described by equations (5) and (6) [49].

$$g_C(E) = \begin{cases} \frac{8\pi\sqrt{2}m_e^{\frac{3}{2}}}{h^3}\sqrt{E - E_C}, for\ electrons\ with\ energy\ E \geq E_C \\ 0\ for\ electrons\ with\ energy\ E \leq E_C \end{cases} \quad (5)$$

$$g_V(E) = \begin{cases} \frac{8\pi\sqrt{2}m_h^{\frac{3}{2}}}{h^3}\sqrt{E_V - E}, for\ holes\ with\ energy\ E \leq E_V \\ 0, for\ holes\ with\ energy\ E \geq E_V \end{cases} \quad (6)$$

This model may be considered an inaccurate approximation for organic semiconductors. First, to extend the concept of effective mass for electrons and holes from inorganic to organic semiconductors is a rough approximation. But most importantly, these equations were obtained assuming that electrons and holes in an organic semiconductor may be described as fermions confined in a *3-D* quantum well.

An infinite quantum well simplification is an approximation used in crystalline inorganic semiconductors since charge carrier wave-functions are highly delocalized over the entire system. If the semiconductor exhibits few impurities, strong electronic coupling between adjacent sites will promote delocalization. However, most organic semiconductors are at most semi-crystalline, which leads to charge carrier wave-function localization and a dominant hopping regime, as opposed to band transport. Since electron-vibration couplings are dominant (that is, there is a strong connection between electronic and geometric structure), charges hop incoherently between adjacent molecules.

Gaussian rather than free-electron-like densities of states are an alternate approximation to the density of states of organic semiconductors. Assuming a Gaussian-broadened [40] manifold of transport levels, Ueno proposed expressions (7) and (8) [53, 54], where $N_{e\text{-}O}$, $N_{h\text{-}O}$, σ_e, σ_h, $E_{e\text{-}O}$ and $E_{h\text{-}O}$ are the total density of states, standard deviation and peak positions in energy for electron- and hole-transport manifolds.

$$g_{e-O}(E) = \frac{N_{e-O}}{\sigma_e\sqrt{2\pi}} \exp\left(-\frac{(E - E_{e-O})^2}{2\sigma_e^2}\right) \tag{7}$$

$$g_{h-O}(E) = \frac{N_{h-O}}{\sigma_h\sqrt{2\pi}} \exp\left(-\frac{(E - E_{h-O})^2}{2\sigma_h^2}\right) \tag{8}$$

2.3.4.4 Density of carriers in organic and inorganic semiconductors

The density of free electrons in the conduction band of an inorganic semiconductor can be obtained by integrating the product of the distribution function for electrons with their probability of occupation, for energies ranging from the bottom of conduction band to infinity. This procedure is conducted in full analogy at the valence band to obtain the

density of free holes and holds for organic and inorganic semiconductors. If equations (4) through (6) are used, the density of charge carriers becomes (spin degeneracy of 1):

$$n_I = \int_{E_C}^{\infty} g_C\,(E) f(E) dE = N_c e^{\frac{E_F - E_C}{K_B T}}, \qquad N_C = 2\left(\frac{2\pi m_e^* k_B T}{h^2}\right)^{\frac{3}{2}} \tag{9}$$

$$p_I = \int_{-\infty}^{E_V} g_V(E)\big(1 - f(E)\big) dE = N_V e^{\frac{E_V - E_F}{K_B T}}, N_V = 2\left(\frac{2\pi m_h^* k_B T}{h^2}\right)^{\frac{3}{2}} \tag{10}$$

For the case of organic semiconductors, using equations (4), (7) and (8), the density of charge carriers is (spin degeneracy of 1):

$$n_O = \int_{E_{e-O}}^{\infty} g_{e-O}(E) f(E) dE = N_{e-O} e^{\frac{E_F - E'_{e-O}}{K_B T}} \tag{11}$$

$$p_O = \int_{-\infty}^{E_{h-O}} g_{h-O}(E)\big(1 - f(E)\big) dE = N_{h-O} e^{\frac{E'_{h-O} - E_F}{k_B T}} \tag{12}$$

In which,

$$E'_{e-O} = \frac{k_B T}{2\sigma_{\mathrm{e-O}}^2}\left(E_{e-O}^2 - \left(E_{e-O} - \frac{\sigma_{\mathrm{e-O}}^2}{k_B T}\right)^2\right) \tag{13}$$

$$E'_{h-O} = \frac{k_B T}{2\sigma_{h-O}^2}\left(\left(E_{h-O} - \frac{\sigma_{\mathrm{h-O}}^2}{k_B T}\right)^2 - E_{h-O}^2\right) \tag{14}$$

Expressions (9) through (12) indicate that, regardless of the semiconductor being organic or inorganic, charge carrier densities will exhibit an exponential dependence with respect to energy. This is not surprising as indeed, mass-action law for an intrinsic

semiconductor in thermal equilibrium may be derived from purely thermodynamic arguments. In fact, [51]

$$np = n_i^2 = Ae^{-\frac{\Delta F^0}{k_B T}} = Ae^{\frac{\Delta S^0}{k_B}} e^{-\frac{\Delta U^0}{k_B T}} \tag{15}$$

where A is the activity coefficient term, ΔF^0 is the Helmholtz free energy of a constant volume process and $\Delta U^0 = E_g$. Furthermore, in first approximation, expressions (9) through (12) provide a simple tool to evaluate changes in carrier density as a function of variations in the Fermi level energy of an inorganic and organic semiconductor. For example, if p_0 is the intrinsic concentration of holes in an organic semiconductor and p_1 is the increased concentration after *p*-type doping, (12) predicts (analogous for electrons):

$$E_{F_0} - E_{F_1} = \Delta E_F = k_B T \ln\left(\frac{p_1}{p_0}\right) = k_B T \ln(10^{\alpha}) \approx 60\alpha \; meV \; at \; 25\,℃ \tag{16}$$

2.4 Device Physics of Organic Photovoltaics

2.4.1 Operation

An organic solar cell converts input optical power into electrical power, that is, a photovoltage and a photocurrent. The photocurrent may be described as a consequence of the following processes: (1) photon absorption and exciton formation; (2) exciton migration; (3) charge separation; (4) free charge carrier transport and (5) charge collection at an electrode. The photovoltage requires that separated charges of different polarity accumulate in opposing regions of the device, a process which is often favoured through the incorporation of a built-in-potential, as will be discussed later in section 2.4.3. Physical

processes that lead to charge transport and collection are briefly described below and depicted in Figure 2-4 [55, 56].

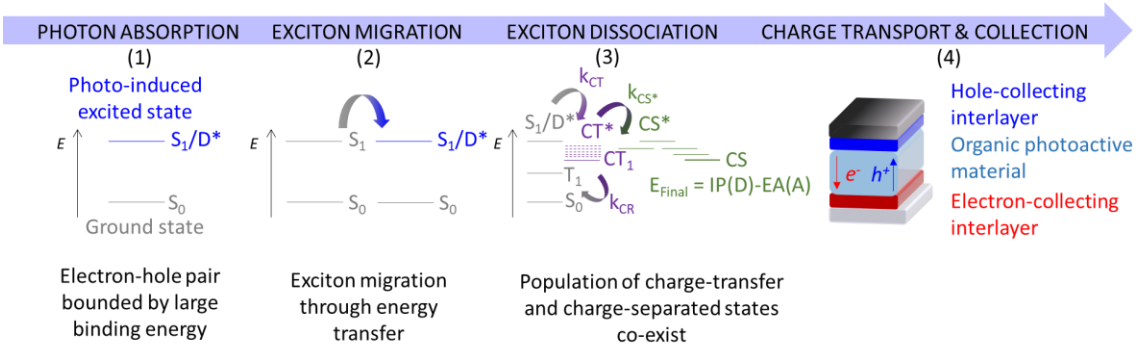

Figure 2-4. Operation of an organic solar cell under illumination.

(1) Photon Absorption: When an incoming photon is absorbed by an organic semiconductor, a molecule or polymer segment is promoted from its ground state to a singlet excited state. Then, it relaxes down to the bottom of the potential energy surface (i.e., it becomes the singlet excited state with lowest energy), and an exciton is formed. This is a neutral species as the electron and hole remain Coulombically bound to each other.

(2) Exciton Migration: Since excitons are neutral species, their movement is not affected by an electric field. Instead, the energy of the excited state is transferred incoherently from one molecule or polymer chain segment to another until the exciton reaches an interface between a donor and an acceptor, or it recombines (whatever happens first, depending upon the exciton diffusion length).

(3) Exciton Dissociation: A widely accepted molecular picture of the exciton dissociation process remains elusive due to its complexity [57]. However, given the scope of this work, it suffices to mention that dissociation involves at least two additional states: the

charge-transfer state (CT) and the charge-separated (CS) state. If an exciton reaches the interface between donor and acceptor molecules, it can relax to the CT state, in which the electron and hole are still Coulombically bound to each other, but now the hole is located on the donor molecule and the electron moved to the acceptor molecule. Furthermore, if an exciton reaches a CS state, the electron and hole will not be bound anymore, and they will relax until their energy is that of the transport gap, that is, the *IE* (Donor) - *EA* (Acceptor). Populations of excitons, CT states and CS states exist simultaneously in a device under illumination.

(4) Charge Transport and Collection: In a solar cell under illumination (either organic or inorganic), gradients of quasi fermi level energies, densities of electrons and holes and their respective charge mobilities directly determine the amount of charge carriers moving towards each electrode. In other words, mobile photo-generated charge carriers can move along the conjugated backbone of organic materials, but to collect them at opposite electrodes, a driving force needs to be added to the system. In inorganic *p-n* junctions, a depletion region provides a built-in potential that drives charge carriers in opposite directions. Similarly, an asymmetry is required in organic solar cells to have mobile holes and electrons flow in opposite directions. This asymmetry is built into the device by means of a hole-collecting and an electron-collecting interlayer next to each electrode, to modify their work functions. Furthermore, interlayers may compensate the impact of interfacial charge-density redistributions at the interface between metals and semiconductors.

2.4.2 Figures of merit

For an organic solar cell to work optimally, it needs to follow certain design criteria. Each operation step described in 2.4.1 imposes certain conditions on the materials and device architecture. For efficient charge collection, the device architecture should sandwich the light absorber between two electrodes such that, under illumination, the LUMO and HOMO manifolds resembles the energy level diagram of Figure 2-5.

If the organic solar cell is put under illumination, its fermi level energy will split into two: the quasi fermi level for electrons and holes. Furthermore, the gradient of such quasi fermi levels directly impacts the total amount of electrons and holes available for collection. Thus, the photovoltage and photocurrent may be written as:

$$eV_{OC} = F_n(d) - F_p(0) \tag{17}$$

$$\overrightarrow{J_T} = n\mu_e\vec{\nabla}F_n + p\mu_h\vec{\nabla}F_p \; where \; \left\|\overrightarrow{J_T}\right\| = J_{SC} \tag{18}$$

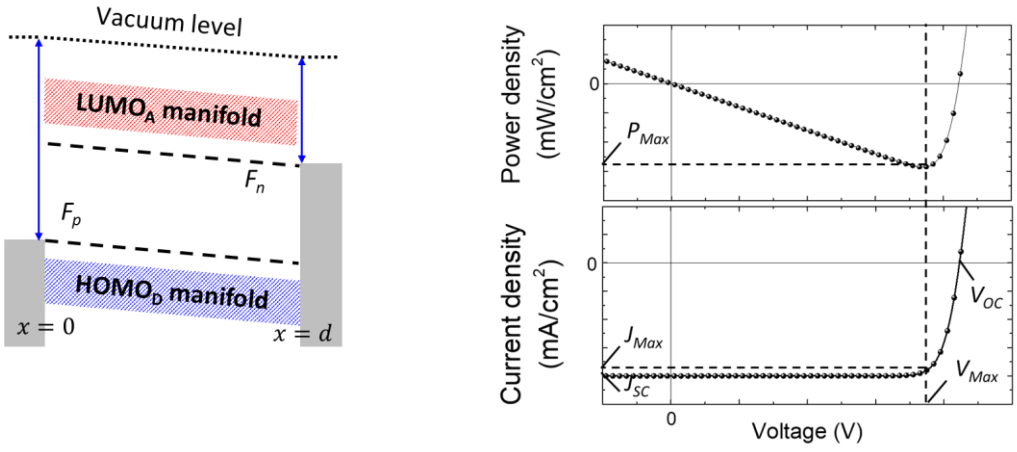

Figure 2-5. An organic solar cell under illumination. Left: energy level diagram where F_N and F_P stand for the quasi fermi level energies for electrons and holes, respectively,

and the hole-collecting electrode is at *x*=0 while the electron collecting electrode is at *x*=*d*. Right: figures of merit in a *J*-*V* and *P*-*V* plot.

Consequently, key metrics to evaluate the performance of an organic solar cell are the open circuit voltage V_{OC} [V], the short-circuit current density J_{SC} [mA cm^{-2}], the fill factor *FF* [%],

$$FF = \frac{J_{Max}V_{Max}}{J_{SC}V_{OC}} \tag{19}$$

and the power conversion efficiency (PCE) η [%]:

$$PCE(\eta) = \frac{V_{OC}J_{SC}FF}{P_{In}} \tag{20}$$

Furthermore, the spectrum of the light source has a direct impact on the maximum achievable short circuit current of the device under illumination. Both the location where the photon is absorbed, and its energy impact the efficiency of its conversion. Therefore, the upper limit for the short circuit current of a solar cells under illumination is:

$$J_{SC} \leq e \int_{AM\ 1.5} \eta_{EQE}(\lambda) N_{ph}(\lambda) d\lambda \tag{21}$$

In expression (21), *e* is the fundamental charge, $N_{ph}(\lambda)$ is the photon flux density of the incident optical power with AM 1.5 G spectrum at wavelength λ and a total intensity of 100 mW cm^{-2} (when integrated over the full spectrum), and η_{EQE} is the external quantum efficiency or *EQE*, which corresponds to the fraction of incident photons converted into current [56].

2.4.3 Organic photovoltaics fabricated using dopants

Electrical doping of organic semiconductors may be used to increase their charge carrier mobility as well as to facilitate injection or collection from metal electrodes. Although not exclusively, doped organic semiconductors have been introduced in organic solar cells as interlayers to favour charge transport and collection.

From a fabrication perspective, such interlayers consist of either a fully doped organic film which is laminated or evaporated onto the organic photoactive material, or a 'thin' (1-5 nm) pure dopant film, also laminated or evaporated onto the organic light absorber. Many molecular dopants had been reported in the literature, both for *n*- and *p*-type doping. Yet, until early 2017, there were no successful and simple demonstrations of dopants which would, in steady-state conditions, diffuse only down to a limited depth into the organic semiconductor [41].

2.4.4 Organic photovoltaics fabricated using phosphomolybdic acid

2.4.4.1 Phosphomolybdic and Phosphotungstic acid as interlayers in OPVs

12-molybdophosphoric acid hydrate (phosphomolybdic acid or PMA) and 12-phosphotungstic acid hydrate (or PTA) belong to a class of polyoxometalates (POMs) known as heteropoly acids with a Keggin structure. These nanoclusters consist of a phosphate ion and twelve molybdenum or tungsten oxyanions, as shown in Figure 2-6 [58].

Regarding the combination of polyoxometalates and conjugated polymers, examples date back to the 2000's [59-61]. Regarding OPVs, Sun and co-workers in late 2013 demonstrated the use of PMA as an efficient hole-collecting interlayer for organic

solar cells with an absorber containing PTB7 and $PC_{71}BM$ [62]. Similar work was conducted by Argitis, Tortech and Ruan, demonstrating the use of PTA and PMA to favour hole collection in single junction and tandem organic solar cells. However, researchers did not mention anything related to *p*-type electrical doping [63-66].

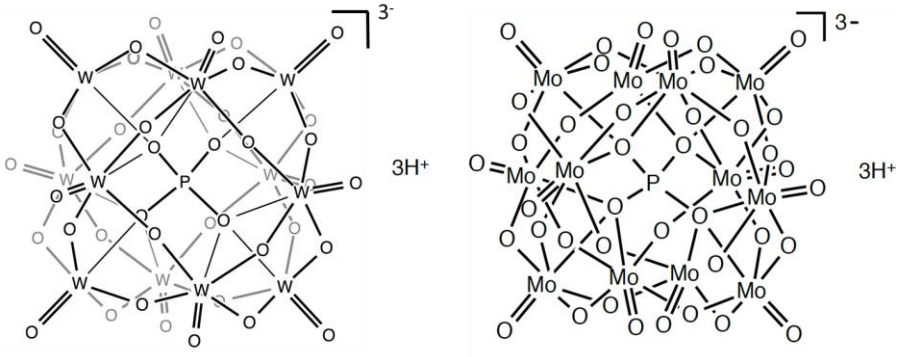

Figure 2-6. Molecular structures of 12-phosphotungstic acid hydrate (left) and 12-molybdophosphoric acid hydrate (right) [58].

2.4.4.2 Phosphomolybdic acid as a *p*-type dopant in OPVs

In 2016, Aizawa and co-workers found that, by immersing neat films of the polymer poly[N-9'-heptadecanyl-2,7-carbazole-alt-5,5-(4',7'-di-2-thienyl-2',1',3'-benzothiadiazole)] (PCDTBT) into a solution of PMA-nitromethane, these films would exhibit an increase in their electrical conductivity of ca. 6 orders of magnitude and corresponding fermi level energy changes, (see equation (10)) supporting *p*-type doping. Doped films worked efficiently as hole-collecting interlayers in conventional-geometry OPVs [67]. Yet, it was not until 2017 when Kolesov and co-workers generalized the technique to a post-process immersion method (see Figure 2-7).

Electrical and optical characterization of doped films, including electrical conductivity, work function, UV-Vis-NIR spectroscopy and X-ray Photoelectron

spectroscopy measurements supported electrical *p*-type doping of organic semiconductors down to a limited depth from the surface.

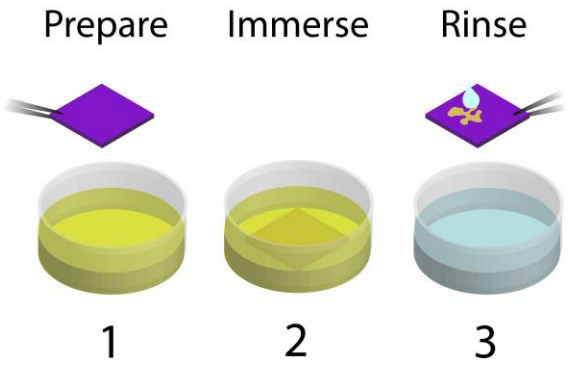

Figure 2-7. Immersion of conjugated polymer films into PMA-nitromethane solution.

Electrical conductivity was shown to increase by over 6 orders of magnitude, and corresponding changes in work function were demonstrated, up to 0.4 eV, upon PMA-immersion. Regarding the optical characterization, UV-Vis-NIR spectroscopy of PMA-immersed P3HT films evidenced photo-bleaching of the main π-π* absorption bands of the organic semiconductor, as well as variations in the IR region which correlate well with P3HT polaron bands. Furthermore, XPS measurements into the depth of PMA-immersed P3HT indicated the oxidation of sulphur S (2s) of P3HT alongside the reduction of Mo (3d) of PMA. In fact, increased photo-oxidation stability of PMA-immersed P3HT as compared to pristine ones point out to molecular hindrance of the photo-oxidation mechanism that leads to sulphur oxidation (S=O) on the backbone of P3HT. In conclusion, immersion of polymer semiconductors and bulk-heterojunction based organic solar cells into a PMA-nitromethane solution produced electrical *p*-type doping down to a limited depth. This key feature made possible to embed the hole-collecting region into OPV

devices with various photoactive materials, a step that simplified their fabrication and led to the demonstration of the first single layer organic solar cell [68].

Still, critical to the method was the use of nitromethane, a highly unstable solvent, to dissolve PMA. According to the National Fire Protection Association (NFPA), nitromethane is readily capable of detonation, explosive decomposition or explosive reaction at room temperature and atmospheric pressure. While many solvents readily dissolve PMA, the ability of a PMA solution to electrically dope an organic semiconducting film efficiently was found strictly dependent on the selected solvent. Thus, as long as the technique relies on the use of nitromethane, its applicability to large-scale fabrication of organic solar cells would be limited.

More importantly, the interplay between organic semiconductors, PMA and solvent molecules that leads to *p*-type electrical doping of organic films remained unclear. In other words, what are the key variables that govern this process? Ultimately, this technique is unique in that it produces vertical doping profiles, but there is no clear rationale behind such profiles or the phenomena causing them. These questions are the starting point of this PhD Thesis.

CHAPTER 3. RESEARCH METHODS

3.1 Materials

A comprehensive list of organic conjugated polymers, organic conjugated molecules, polar and non-polar solvents, substrates, electrically conductive materials and nanocluster required to conduct all experiments reported in this thesis is included hereon.

Organic conjugated polymers were Poly(3-hexylthiophene-2,5-diyl) or P3HT, regioregular Electronic grade (Rieke metals, product# 4002-E), Poly(3-hexylthiophene-2,5-diyl), regiorandom (Rieke metals, product# 4007) and Poly[(2,6-(4,8-bis(5-(2-ethylhexyl)thiophen-2-yl)-benzo[1,2-b:4,5-b']dithiophene))-alt-(5,5-(1',3'-di-2-thienyl-5',7'-bis(2-ethylhexyl)benzo[1',2'-c:4',5'-c']dithiophene-4,8-dione)] or PBDB-T, (1-Material). Also, the non-conjugated polymer polyethylenimine, 80% ethoxylated, was used (Sigma Aldrich, product# 306185). Some experiments also include the use of the fullerene derivative indene C_{60} bisadduct or ICBA (Nano-C). Materials were used as received.

Solvents used to dissolve aforementioned materials and make inks were acetonitrile (anhydrous, 99.8% purity, Sigma Aldrich, product# 271004), nitromethane (ACS reagent, > 95% purity, Sigma Aldrich, product# 360554), 2-propanol (anhydrous, 99.5% purity, Sigma Aldrich, product# 278475), chlorobenzene (anhydrous, 99.8% purity, Sigma Aldrich, product# 284513), 1,2-dichlorobenzene (anhydrous, 99% purity, Sigma Aldrich, product# 240664), Dimethyl sulfoxide (anhydrous, 99.9% purity, Sigma Aldrich, product# 276855), N,N-Dimethylformamide (anhydrous, 99.8% purity, Sigma Aldrich, product# 227056), 2-methoxyethanol (anhydrous, 99.8% purity, Sigma Aldrich, product# 284467)

and ethyl alcohol (anhydrous, 99.5% purity, Sigma Aldrich, product# 459836). All solvents were used as received.

Metals, metal oxides and a nanocluster were used to complete the fabrication of organic photovoltaic devices reported in this thesis. In particular, Ag (Kurt J. Lesker, product# EVMAG40QXQ-B) and MoO_3 (Fisher Scientific, Molybdenum (VI) Oxide, Puratronic ®, 99.9995% purity, product# 12930) were used. The nanocluster used as *p*-type electrical dopant is 12-molybdophosphoric acid or PMA (Fisher Scientific, product# AA5616622). These materials were used as received.

Finally, ITO-coated soda lime float glass sheets with a sheet resistance of 9 Ω/□ to 15 Ω/□ (Colorado Concept Coatings LLC and MSE supplies), plain glass slides (VWR Micro Slides product #48300-026) and Silicon wafers (University Wafers, part# S4N01SP) were used as substrates.

3.2 Fabrication

3.2.1 Substrate preparation

Either plain glass slides, ITO-coated soda lime float glass sheets or silicon wafers indicated in section 3.1 were cleaved into 1'' by 1'' pieces and used as substrates for organic semiconducting films. These substrates were then solvent cleaned in sequential ultrasonic baths (Branson 5510) using Liquinox detergent dissolved in distilled water, distilled water, acetone and 2-propanol, each lasting 40 min and at a temperature of 40 °C. Then, substrates were blown dry with N_2 and transferred into a N_2-filled glovebox for further processing.

3.2.2 Films of P3HT immersed in PMA solutions at room temperature

P3HT was weighed on an electronic scale in air and added to two amber glass vials, each with a magnetic stirrer. The vials were transferred to a N_2-filled glove box for further processing. On the first vial, the P3HT was dissolved to a concentration of 10 mg ml^{-1} using chlorobenzene. On the second vial, the P3HT was dissolved to a concentration of 30 mg ml^{-1} using 1,2-dichlorobenzene. Both solutions were magnetically stirred overnight at 500 RPM at room temperature.

The 10 mg ml^{-1} solution of P3HT in chlorobenzene was filtered using a 0.2 µm pore-size PTFE filter and spun coated (Spin Coater by Headway research, Inc.) onto plain glass slides and silicon wafers at 800 RPM, 10,000 RPM s^{-1} for 30 s, dispensing 200 µl of solution per sample. Then, samples were left in glass petri dishes to solvent anneal for 1 h and thermally annealed on a hot plate at 150 °C for 10 min.

The 30 mg ml^{-1} solution of P3HT in 1,2-dichlorobenzene was filtered using a 0.2-µm-pore PTFE filter and spun coated (Spin Coater by Headway research, Inc.) onto the ITO-coated glass slides at 800 RPM, 10000 RPM s^{-1} for 30 s, dispensing 200 µl of solution per sample. Then, samples were left inside glass petri dishes to solvent anneal for 3 h and thermally annealed by placing them on a hot plate at 150 °C for 10 min.

As-made P3HT films processed from chlorobenzene were dipped into a 0.5 M solution of PMA in nitromethane or acetonitrile for 30 min and then thoroughly rinsed with pure solvent, to remove PMA residues from their surface. The as-made P3HT films processed from 1,2-dichlorobenzene were similarly dipped into a 0.5 M PMA solution in nitromethane or acetonitrile for 1 min, 10 min or 30 min, and rinsed using pure solvent.

3.2.3 Films of PBDB-T immersed in hot PMA solution

Plain glass slides and silicon wafers were cleaved into 1'' by 1'' pieces and used as substrates for PBDB-T semiconducting films. ITO-coated glass sheets with tailored patterns were also used as substrates for PBDB-T semiconducting films. All substrates were prepared as indicated in section 3.2.1.

PBDB-T was weighed on an electronic scale in air and added to three amber glass vials each with a magnetic stirrer. Vials were transferred to a N_2-filled glove box for further processing. PBDB-T was dissolved to concentrations of 5 mg ml^{-1}, 10 mg ml^{-1} and 20 mg ml^{-1} using chlorobenzene. Solutions were magnetically stirred overnight at 500 RPM and 50 ºC overnight.

The 5 mg ml^{-1} PBDB-T solution in chlorobenzene was dynamically spun (Spin Coater by Headway research, Inc.) onto VWR glass slides at 1,000 RPM, 1,000 RPM/s for 30 s, dispensing 100 µl of solution per sample. Then, samples were left in glass petri dishes to solvent anneal for 1 h. As-made PBDB-T films were heated on a hot plate at 100 ℃, alongside a 0.5 M solution of PMA in acetonitrile, for 15 min. Then, hot PBDB-T samples were immersed into the hot PMA solution for 1 min and left to cool at room temperature for 5 min immediately after. Then, samples were rinsed thoroughly with pure solvent at room temperature, to remove all PMA residues from their surface.

The 10 mg ml^{-1} PBDB-T solution in chlorobenzene was dynamically spun (Spin Coater by Headway research, Inc.) onto ITO-coated glass slides at 1000 RPM, 1,000 RPM s^{-1} for 60 s, dispensing 100 µl of solution per sample. Then, samples were left in glass petri dishes to solvent anneal for 1 h. As-made PBDB-T films were heated on a hot plate at 40

°C, 60 °C, 80 °C and 100 °C for 15 min. In each case, a 0.5 M solution of 12-molybdophosphoric acid hydrate (PMA) in acetonitrile was also heated at the same temperature, for 15 min. Then, hot PBDB-T samples were immersed into the hot PMA solution for 1 min, left to cool at room temperature for 5 min and rinsed thoroughly with pure solvent at room temperature, to remove all PMA residues from their surface.

The 20 mg ml^{-1} PBDB-T solution in chlorobenzene was dynamically spun (Spin Coater by Headway research, Inc.) onto Si substrates at 2,500 RPM, 1,000 RPM s^{-1} for 60 s, dispensing 100 µl of solution per sample. Then, samples were left in glass petri dishes to solvent anneal for 1 h.

3.2.4 Films of PBDB-T coated with PMA solution and a swelling solvent

Plain glass slides were cleaved into 1'' by 1'' pieces and used as substrates for PBDB-T semiconducting films. ITO-coated glass sheets with tailored patterns and a sheet resistance between 9-15 Ω/□ were also used as substrates for PBDB-T semiconducting films. All substrates were prepared as indicated in section 3.2.1.

PBDB-T was weighed on an electronic scale in air and added to an amber glass vial with a magnetic stirrer. The vial was transferred to a N_2-filled glove box for further processing. PBDB-T was dissolved to a concentration of 10 mg ml^{-1} using chlorobenzene and magnetically stirred overnight at 500 RPM and 50 ºC overnight. The fully dissolved 10 mg ml^{-1} PBDB-T solution in chlorobenzene was dynamically spun (Spin Coater by Headway research, Inc.) onto VWR glass slides at 2,500 RPM, 1,000 RPM s^{-1} for 45 s, dispensing 100 µl of solution per sample. Then, samples were left in glass petri dishes to solvent anneal for 1 h.

PMA was dissolved in 2-propanol at a 0.5 M concentration and left stirring for 1 h at room temperature in air, after which the solution appeared homogeneous to the naked eye. The solution was transferred to a N_2-filled glove box, combined in 4:1 or 9:1 ratio by volume with chlorobenzene or 1,2-dichlorobenzene and these 4 additional solutions were stored in amber vials inside the glovebox. These solutions were dynamically spun (Spin Coater by Headway research, Inc.) onto PBDB-T films, coating 160 µl of solution per sample at 1,000 RPM, 1,000 RPM/s for 30 s. Samples were left to solvent anneal for 1 h inside the glovebox at room temperature to ensure full solvent evaporation. Then, treated PBDB-T samples were rinsed thoroughly with 2-propanol at room temperature to remove PMA residues from their surface.

3.2.5 OPV devices electrically p-type doped with PMA in acetonitrile

ITO-coated soda lime float glass sheets (4 mm thick, 1'' by 1'' length and width), with a sheet resistance of 9-15 $\Omega\ \square^{-1}$ were used as substrates and prepared as described in section 3.2.1. PEIE dissolved in H_2O at a concentration of 37 wt.% had previously been purchased from Sigma-Aldrich, further diluted with 2-methoxyethanol to a concentration of 0.1 weight % and left stirring overnight at 500 RPM inside a transparent vial in air. The 0.1 weight % PEIE solution was then spun coated (Spin Coater by Headway research, Inc.) on the cleaned ITO substrates at 5000 RPM, 928 RPM s^{-1} for 1 min and the wet layer was annealed immediately after on a hot plate at 100 ºC for 10 min, in air. Coated substrates were then transferred into a N_2-filled glove box for further processing.

Regioregular P3HT had previously been mixed with ICBA in a 1:1 weight ratio and dissolved into a 40 mg ml^{-1} solution using 1,2-dichlorobenzene. The solution was magnetically stirred overnight at 500 RPM at 70 °C, inside a nitrogen-filled glovebox.

The P3HT:ICBA solution was filtered through a 0.2-µm-pore PTFE filter and spun coated (Spin Coater by Headway research, Inc.) onto each Glass/ITO/PEIE sample at 800 RPM, 10,000 RPM s^{-1} for 30 s, dispensing 200 µl per sample. The resulting wet films were then slowly dried in covered glass Petri dishes for 3 h. Next, a portion of the P3HT:ICBA layer was wiped off using chlorobenzene to expose the underlying ITO electrode to allow electrical contact.

Slides with a stack of ITO, PEIE and P3HT:ICBA layers, one on top of the other, were thermally annealed on a hot plate set to 150 °C for 10 min inside the glovebox, and let to cool down in covered glass Petri dishes for 30 min. Next, samples were dipped into a 0.5 M solution of PMA dissolved in acetonitrile for various times (1 min, 10 min, 30 min). Immediately after soaking, each doped sample was thoroughly rinsed with pure solvent to remove PMA residues from their surface.

Samples were then transferred through an antechamber to an adjacent nitrogen-containing glovebox which is integrated with a Kurt J. Lesker thermal evaporator. Slides were mounted onto a sample holder and affixed to a shadow mask with openings defining 5 rectangular-with-rounded-corners-shaped electrodes for individual devices. The vacuum chamber was pumped down to a base pressure of 1×10^{-7} Torr. The thermal evaporator system was then used to deposit 150 nm of Ag (at a rate of 0.1-3.0 Å s^{-1}). Resulting OPV devices were unloaded from the system to conduct the electrical characterization.

3.3 Characterization

Equipment and facilities needed to characterize prepared materials, films and OPV devices were available either at the Kippelen Group Laboratory in the Molecular Science and Engineering Building of the Georgia Institute of Technology, or at the Material Characterization Facility at Georgia Tech's Institute of Electronics and Nanotechnology (IEN). In what follows, all procedures used to characterize materials, films and OPV devices are described.

3.3.1 ^{31}P NMR measurements of PMA dissolved in acetonitrile

10 µl of PMA acetonitrile solution at 0.5 M were added to 500 µl deuterated water contained in an 8 inches-long and 5 mm-thick glass tube compatible with NMR spectroscopy in the range between 300 MHz and 500 MHz. Then, the tube was loaded inside the NMR machine and ^{31}P NMR characterization was conducted. Chemical shift data was calibrated using a previous run with phosphoric acid dissolved in deuterated water.

3.3.2 FTIR spectroscopy of PMA dissolved in solvents and dried

A Nicolet 6700 FTIR spectroscopy instrument with a DTGS TEC detector, a KBr beam splitter and an IR source were calibrated in air. The wavenumber range was set to a maximum of 4,000 cm^{-1} and a minimum of 500 cm^{-1}. All measurements were set to transmittance mode. Each measurement corresponded to the average of 64 scans.

0.5 M PMA-acetonitrile and 0.5 M PMA-ethanol solutions were prepared in air at room temperature and left stirring for 1 h inside capped transparent vials. Then, vials were

uncapped and put on a hot plate at 70 ºC inside a fume-hood in air to fully evaporate solvents. After 12 h, vials were capped again and left at room temperature to cool down for additional 12 h.

The material inside each vial and pristine PMA were sequentially loaded on the stage of the Nicolet 6700 tool and their transmittance spectra were measured.

3.3.3 FTIR spectroscopy of neat and PMA-immersed P3HT strands

A Nicolet 6700 FTIR spectroscopy instrument with a DTGS TEC detector, a KBr beam splitter and an IR source were calibrated to be used in air. The wavenumber range was set to a maximum wavenumber of 4,000 cm^{-1} and a minimum of and 500 cm^{-1}. All measurements were set to be conducted in transmittance mode. Each measurement corresponded to the average of 64 scans.

A strand of neat P3HT (as received from the vendor) was dipped into a 0.5 M PMA-acetonitrile solution for 1 min, rinsed with pure acetonitrile and blown dry with N_2 in air. Next, both the PMA-immersed P3HT strand and a new P3HT strand were sequentially loaded on the stage of the Nicolet 6700 tool and their transmittance spectra were measured.

3.3.4 Optical characterization of conjugated polymer films at room temperature

The UV-vis-NIR transmittance spectra of conjugated polymer films or bulk heterojunctions prepared on glass according to sections 3.2.2, 3.2.3 or 3.2.4 were measured using a Variable Angle Spectroscopic Ellipsometry system (J. A. Woollam Co.) calibrated in air and set to operate in transmittance mode. The wavelength range was set to a minimum

of 245 nm and a maximum of 1690 nm, and the stage in which the sample was mounted was at room temperature.

Angles ψ^{o} and Δ^{o} corresponding to the change in polarization state of the measurement beam, induced by reflection from conjugated polymer films prepared on silicon according to sections 3.2.2, 3.2.3 or 3.2.4, were measured using a Variable Angle Spectroscopic Ellipsometry system (J. A. Woollam Co.). The system was calibrated in air and set to operate in ellipsometry mode. The wavelength range was set to a minimum of 245 nm and a maximum of 1690 nm. Measurements were conducted with both source and detector arms at angles of 65º, 70º and 75º. Both the sample and the stage in which it was mounted were at room temperature.

3.3.5 Temperature dependent optical characterization of a PBDB-T film

Liquid nitrogen was connected to a Variable Angle Spectroscopic Ellipsometry system (J. A. Woollam Co.) and a stage with thermally conducting paste was used to load conjugated polymer films prepared on silicon according to sections 3.2.2, 3.2.3 or 3.2.4. The system was configured to operate in ellipsometry mode with both source and detector arms fixed at an angle of 70º. Temperature was varied from 10 °C to 140 °C at a rate of 2.5 °C / min. The thickness of the conjugated polymer film was estimated automatically at each temperature using an optical model loaded on the software CompleteEASE™ (J.A. Woollam). The model was built using an isotropic Bruggeman effective medium approximation comprised of two phases: (1) pristine PBDB-T at room temperature, and (2) air. The total thickness was estimated by varying the film free volume and finding the best fit to spectroscopic ellipsometry data.

3.3.6 Electrical conductivity of pristine and PMA-im. conjugated polymer films

Electrical conductivity of conjugated polymer films prepared on glass according to sections 3.2.2, 3.2.3 or 3.2.4 was measured using a 4-point-probe system in air connected to a Keithley 2400 electrometer. The distance in between probes was fixed at 0.1 inches. The electrical resistance of the film was measured at room temperature by connecting the 4 probes to the electrometer. The thickness of the film was measured using a profiler in air (Dektak 6M Stylus Profiler, Veeco, Plainview, NY). Both electrical resistance and film thickness were inputs to estimate sheet resistance and electrical conductivity [69].

3.3.7 Fermi level energy of conjugated polymer films

The Fermi level energy or work function of conjugated polymer films fabricated on ITO according to sections 3.2.2, 3.2.3 or 3.2.4 was measured using a Kelvin Probe in air and at room temperature. The work function of each film was measured at 3 different spots and adjusted by measuring the work function of freshly peeled highly ordered pyrolytic graphite (HOPG, SPI supplies, grade ZYH, 12 mm × 12 mm × 2 mm), with a known work function of 4.6 eV.

3.3.8 Mass depth profile of pristine and PMA-immersed P3HT films

The mass depth profile of PMA-immersed P3HT films was characterized using a Time-of-Flight Secondary Ion Mass Spectrometry instrument (IONTOF ToF SIMS). The tool was operated using a surface charge stabilizing beam (flood gun), a bismuth ion beam to detect ions at the surface of the film, and an oxygen ion beam to drill into the film (sputter gun). After focusing and centring all beams, the spectra was measured on at least 3 different

regions of the sample. The data was processed using IONTOF software. Mo+, In+ and C+ ions were selected to represent the dopant, the ITO region and the conjugated polymer, correspondingly. The depth of the crater in the conjugated polymer film was measured using a profilometer in air (Dektak 6M Stylus Profiler, Veeco, Plainview, NY), and the obtained value was used to scale the depth profile data.

3.3.9 Morphology of pristine and PMA-immersed P3HT films

Grazing Incidence Wide Angle X-ray Scattering or GIWAXS was measured on conjugated polymer films or bulk heterojunctions prepared on silicon according to section 3.2.2 at the Stanford Synchrotron Radiation Lightsource.

Measurements were conducted at beamline 11-3 in a Helium-filled chamber with an X-ray wavelength of 0.9752 Å, and a sample-to-detector distance of 250 mm. The default incident angle was 0.12°. The spectra were recorded on a 2D X-ray detector (MX225, Rayonix LLC) with a pixel size of 73 μm (3,072 × 3,072 pixels) and analyzed using the Nika and WAXStools package for Igor software (WaveMetrics, Inc.) [70, 71]. The polar angle (χ) is defined as the angle of the observed diffraction from the normal to the substrate. Thus, $\chi = 0°$ is perpendicular to the substrate and $\chi = 90°$ is parallel to the substrate. The out-of-plane sector is considered at 0° to 20° and the in-plane sector is 70° to 90°.

3.3.10 J-V characterization of OPV devices

Current density-voltage (*J-V*) characteristics were measured inside a N_2-filled glove box using a source meter (2400, Keithley Instruments, Cleveland, OH) controlled by

a LabVIEW program. To test the solar cell properties under illumination, an Oriel lamp with an air mass 1.5 filter and an intensity of 100 mW cm^{-2} was used as the light source. Each device was covered with an aperture that had a defined area of 0.04 cm^2 and tested in the dark and under illumination conditions.

CHAPTER 4. ELECTRICAL P-TYPE DOPING USING PMA DISSOLVED IN ACETONITRILE

4.1 Introduction

Controlled and stable electrical doping of organic semiconductors is desirable for the realization of efficient organic optoelectronic devices. Thus, progress has been made to understand the fundamental doping mechanisms [41, 48, 72-75], characterize dopant diffusion and doping efficiencies [76-78], optimize device performance [75, 76, 79-81] develop efficient molecular *n*- and *p*- dopants [82-87] and even explore quantitative dedoping and patterning techniques [88-90]. As a result, from a fabrication perspective, organic semiconductors can be doped today using evaporation methods in a high-vacuum chamber or from solution.

Within the solution-based approaches, dopants may be deposited through co-deposition or via sequential deposition. In the first approach, dopants are mixed with the semiconductor in a single solution, whereas in the second method, dopants are coated once the organic film is dry, from solvents that do not dissolve the semiconductor. Co-deposition has the advantage that the mixing ratio of dopant to semiconductor is known and can be precisely controlled. However, poor solubility of the dopants in the solvents of the semiconductors and strong interactions between such compounds and the dopants in solution make it challenging to produce doped films with the required morphology for high performing organic optoelectronics. Consequently, sequential deposition of dopant

molecules appears to be the most suitable alternative to develop large-area devices using high throughput manufacturing [41, 67, 91, 92].

In 2016, the use of 12-molybdophosphoric acid hydrate (PMA) to induce *p*-type doping and crosslinking of neat films of poly[N-9'-heptadecanyl-2,7-carbazole-alt-5,5-(4',7'-di-2-thienyl-2',1',3'-benzothiadiazole)] (PCDTBT) was reported [67]. Later on, a more general approach of sequential solution-based doping was presented, by post-process immersion of donor-like polymer films in PMA-nitromethane solutions. This method renders polymers electrically *p*-type doped over a limited depth of 60 nm and was shown to produce high performing OPV devices, with a power conversion efficiency up to 7.8%, which was comparable to their corresponding reference with an evaporated MoO_3 hole collecting layer [68]. The approach greatly simplified the solar cell geometry and the fabrication complexity as it is vacuum-free and takes place at room temperature. However, critical to the method is the use of nitromethane, a highly unstable solvent, to dissolve PMA. According to the National Fire Protection Association (NFPA), nitromethane is readily capable of detonation, explosive decomposition or explosive reaction at normal temperatures and pressures. While it is known that many solvents readily dissolve PMA, the ability of a PMA solution to electrically dope an organic semiconductor film is highly dependent on the selected solvent. Thus, as long as the post-process immersion technique relies on the use of nitromethane, its applicability to large-scale fabrication of organic solar cells would be limited.

This chapter reports on the use of acetonitrile, an air-stable solvent, as an alternative to nitromethane to enable PMA-based electrical doping of organic semiconductors within a limited depth from the surface. The morphology of doped organic films (using PMA

dissolved in nitromethane or acetonitrile) was studied using Grazing-Incidence Wide-Angle X-ray Scattering (GIWAXS) and the data revealed that the dopant molecules intercalate between the P3HT lamella but cause no change in the π-π stacking. Finally, the use of acetonitrile is validated to fabricate OPVs and it is shown that these devices exhibit increased stability when exposed to normal atmospheric conditions, compared to reference devices fabricated using nitromethane.

4.2 Results and Discussion

4.2.1 Survey of industrial solvents using Hansen solubility theory

The solvent-screening process begun by looking into chemicals that would dissolve the polyoxometalate at room temperature, would not distort the morphology of the organic film when used in sequential solution-based doping, and would be stable in air at room temperature and 1 atmosphere according to the NFPA 704 standard. The search was limited to chemicals with a stability rating of 2 or less, that is, solvents that may undergo violent chemical change at elevated temperatures and pressures but are not readily capable of detonation at normal temperatures and pressures. The search was further constrained by selecting only polar solvents, in hindsight of our previous findings using nitromethane and ethanol, both polar solvents. Finally, chemicals were ranked according to their distance to nitromethane in the Hansen space, and chosen with a distance to nitromethane that is equal or below 16.64 (which is the distance between ethanol and nitromethane according to their Hansen solubility parameters, see Table A-1).

Hence, the following solvents were chosen: 2-propanol, 2-methoxyethanol, dimethyl sulfoxide, dimethylformamide and acetonitrile. PMA was dissolved using each solvent,

and P3HT films were immersed at room temperature in these different solutions. Then, the transmittance spectrum of these films was compared against that of a pristine film with the same thickness. Although all selected solvents readily dissolved PMA, only one produced a solution that significantly altered the transmittance spectra of P3HT films after immersion, providing an indication of efficient electrical doping (see Figure A-1). That solvent is acetonitrile, anhydrous, 99.8% purity, purchased from Sigma Aldrich and used as received in inert atmosphere.

4.2.2 P3HT films doped with PMA-acetonitrile v/s PMA-nitromethane

The optical properties of P3HT films immersed for 30 min in a 0.5 M solution of PMA in acetonitrile (PMA-im-P3HT) were studied by comparing their transmittance spectra against pristine P3HT and P3HT immersed similarly in a 0.5 M solution of PMA in nitromethane (Figure 4-1). The normalized change of transmittance $\Delta T\,T^{-1}$ as a function of wavelength reveals the same spectral signatures reported for PMA-im-P3HT films when PMA was dissolved in nitromethane. That is, changes in the region where $\Delta T\,T^{-1} < 0$ correlate with the P3HT polaron bands, and deviations in the region where $\Delta T\,T^{-1} > 0$ correlate to the bleaching of the main π-π^* absorption bands [93, 94]. The data suggest electrical *p*-type doping into the depth of the organic film. But, additional electrical and physical characterization of the surface and bulk of the doped semiconductor is required to determine if the doping is as effective as when using PMA in nitromethane or less, as we found and reported in the past using PMA dissolved in ethanol [68].

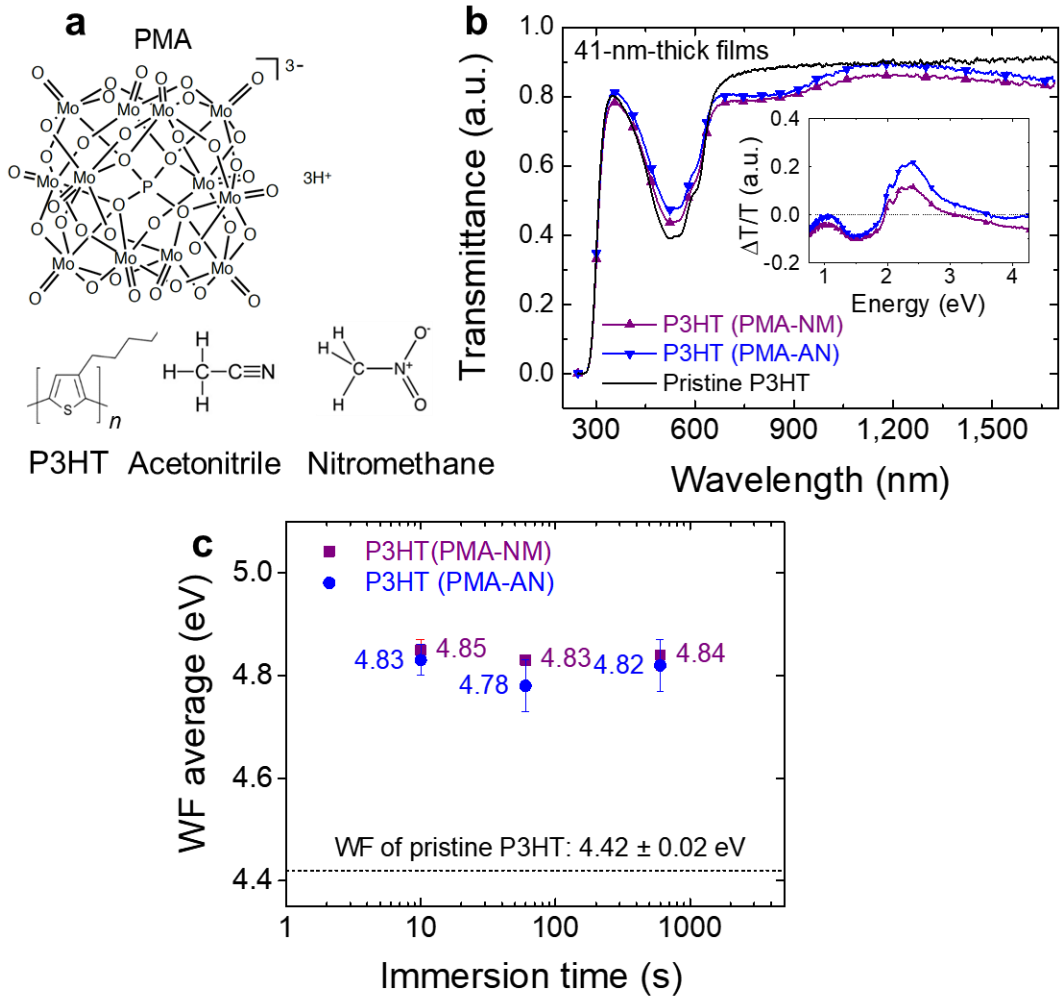

Figure 4-1. Optoelectronic properties of P3HT films immersed in PMA solutions. (a) Chemical structures of phosphomolybdic acid (PMA), nitromethane, acetonitrile and poly(3-hexylthiophene-2,5-diyl) (P3HT). (b) Transmittance of 41 nm-thick pristine P3HT and PMA-im-P3HT. (c) WF values of 188-nm thick PMA-im-P3HT films immersed in PMA in nitromethane or acetonitrile for varying immersion times. Error bars represent statistical variations over a minimum of four spots on each film.

Thus, the surface properties of PMA-im-P3HT films were studied using a Kelvin Probe inside a nitrogen-filled glovebox. The results show a work function (WF) change from 4.4 eV in pristine P3HT, to 4.8 eV in PMA-im-P3HT, whether nitromethane or acetonitrile is used to dissolve the polyoxometalate. This is consistent with Fermi level pinning at the *IE* of P3HT. The change was observed after only 10 s of immersion, and it

remains constant for longer immersion times (1 min or 10 min as illustrated in Figure 4-1). This confirms that the *p*-type electrical doping effect saturates, just as reported earlier [68]. Such a variation in Fermi level energy, when neglecting the presence of surface dipoles, also indicates a change in carrier density of about 10^6 cm^{-3}, if measured at room temperature. This is important because, if electrical *p*-type doping is indeed the cause, then the carrier density variation should correlate with an electrical conductivity increase of up to 6 orders of magnitude, starting in the μS cm^{-1} for pristine P3HT and reaching values in the S cm^{-1} for doped P3HT.

To confirm this claim, the doping profile, overall penetration depth of dopants and electrical conductivity of PMA-im-P3HT films was investigated, for PMA in acetonitrile. In our previous work, the reduction of molybdenum in PMA/PTA-im-P3HT films alongside with the oxidation of sulfur from P3HT demonstrated oxidative doping to a limited depth. As a consequence, the focus now was on the characterization of the molybdenum profile into the bulk of the organic layer, obtained by conducting depth profile measurements of PMA-im-P3HT films using a Time-of-Flight Secondary Ion Mass Spectrometry system (IONTOF ToF SIMS). All P3HT layers were coated onto ITO/glass substrates for ease of data processing. Accordingly, depth profiles of molybdenum (attributed to PMA), carbon (attributed to P3HT) and indium (attributed to ITO) cations were measured in PMA-im-P3HT films when PMA was dissolved in nitromethane or acetonitrile (Figure 4-2). The comparison of such profiles shows that the distribution of molybdenum cations has an exponential shape in both cases and has a decay constant of 15-20 nm when using PMA in nitromethane, and 20-25 nm when dissolving PMA in acetonitrile.

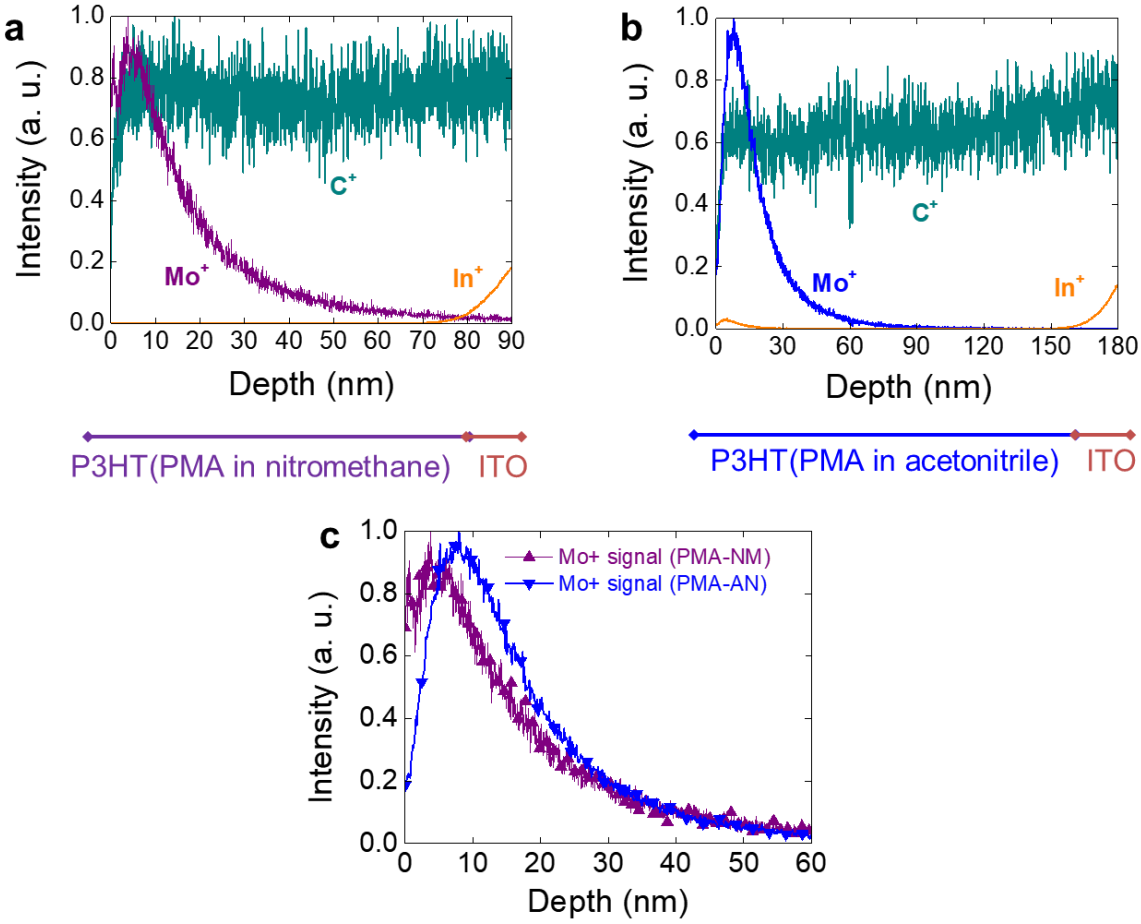

Figure 4-2. Vertical profile of P3HT films measured using mass spectrometry. Normalized signals for Mo+, C+ and In+ cations into the depth of a P3HT film immersed for 1 min in (a) PMA in nitromethane, (b) PMA in acetonitrile, and (c) comparison.

Indeed, the density of dopants is below 4% of its peak at ca. 60 nm from the surface the film, using either nitromethane or acetonitrile. With these data, the electrical conductivity of a 188-nm-thick PMA-im-P3HT film was estimated, after immersion in a PMA solution in acetonitrile for 1 min. A sheet resistance of 40.9 ± 1.0 kΩ $\square^{-1}$ was found using the four-point probe method, which translates into an electrical conductivity of 4.1 S cm^{-1} assuming 60 nm of the bulk electrically *p*-type doped. This value is in good agreement

with previously reported electrical conductivity data and is consistent with WF changes measured using the Kelvin Probe.

4.2.3 Morphology characterization of P3HT films using various PMA solutions

To elucidate why the doping capability of the PMA solution is solvent dependent, the morphology of PMA doped films was investigated when the polyoxometalate is dissolved in various solvents. In addition to acetonitrile, nitromethane and ethanol were chosen, as the latter two produce a PMA solution capable of doping, but PMA-nitromethane is significantly more effective than PMA-ethanol to dope organic films. As a consequence, the direct comparison is correlated back to the dissimilar effectiveness of these doping solutions, as reported in the past [68].

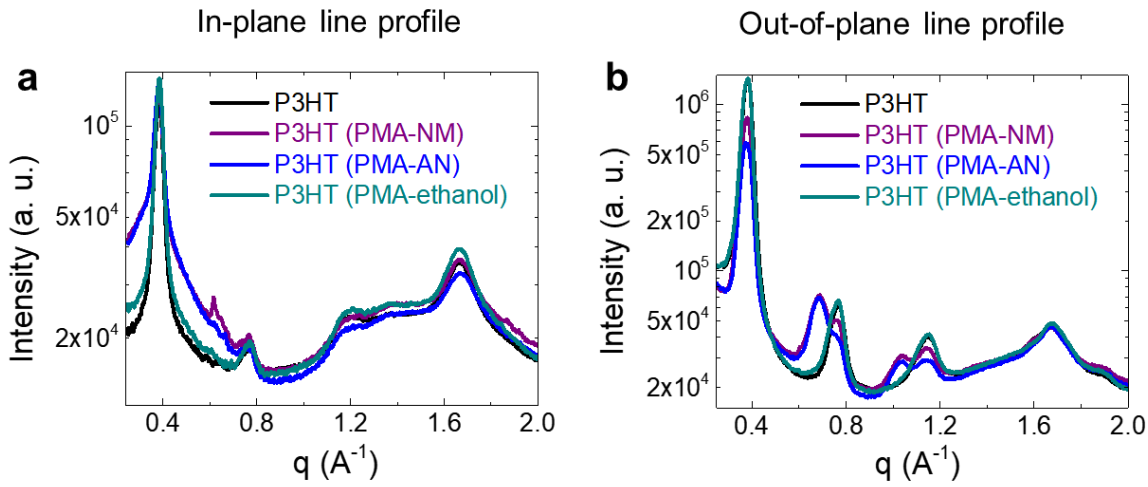

Figure 4-3. In-plane and out-of-plane line profiles obtained from two-dimensional GIWAXS data as measured on pristine and PMA-doped P3HT, when using various solvents to dissolve the PMA.

Therefore, acetonitrile, nitromethane and ethanol were used to dissolve the polyoxometalate and the morphology of PMA-im-P3HT films fabricated on Si substrates

was analyzed using GIWAXS (Figure 4-3). As expected, the images show that the preferred orientation of P3HT on the SiO_2 surface is edge-on, with distinctive (100), (200) and (300) lamellar peaks observed in the out of plane direction with q values of 0.37 $Å^{-1}$, 0.77 $Å^{-1}$ and 1.14 $Å^{-1}$. Also as expected, there is a clear peak on the (010) direction with a q value of 1.68 $Å^{-1}$ in the in-plane line profile (*d*-spacing ca. 0.37 nm), which is due to the π-π stacking of P3HT.

Interestingly, PMA doping does not appear to alter the location of the peaks in the in-plane line profile, which implies no change of the π-π stacking distance of P3HT. Instead, additional peaks appear in the out-of-plane line profile of P3HT samples doped with PMA, when the polyoxometalate is dissolved in either nitromethane or acetonitrile, pointing out to the intercalation of doping molecules between P3HT lamellae. Specifically, in doped samples using PMA in nitromethane or acetonitrile, near the (200) diffraction, the original neat P3HT peak at 0.77 $Å^{-1}$ of the out-of-plane line profile appears next to a new peak at 0.69 $Å^{-1}$. Moreover, near the (300) diffraction, there is a new peak at 1.03 $Å^{-1}$, in addition to the original peak at 1.14 $Å^{-1}$. Thus, the GIWAXS data shows that the dopant molecules, when using PMA dissolved in nitromethane or acetonitrile, become intercalated between the lamellar while producing no distortion in the π-π stacking of P3HT. The lamella *d*-spacing expands from 16.53 Å in pristine P3HT (consistent with the literature [95]) to 18.21 Å in the doped P3HT or by nearly 1.68 Å, for a total PMA nanocluster diameter around 1 nm. However, such an effect is not present when immersing P3HT films into PMA in ethanol. This is consistent with the less effective doping of the PMA-ethanol solution as observed in the past.

4.2.4 OPV devices doped with PMA dissolved in acetonitrile

As reported in 2017, electrical *p*-type doping using a solution of PMA in nitromethane may be used to fine tune the electrical properties of the photoactive layer of an OPV, producing embedded hole-collecting interlayers through a simple film immersion process [68]. Consequently, the performance of OPVs immersed in a 0.5 M solution of PMA in nitromethane or acetonitrile for 1 min was investigated. All OPV devices were fabricated with a 200-nm-thick PMA-im-P3HT:ICBA photoactive layer, on top of an ITO / polyethyleneimine ethoxylated (PEIE) electron-collecting bottom electrode, and with a Ag top electrode.

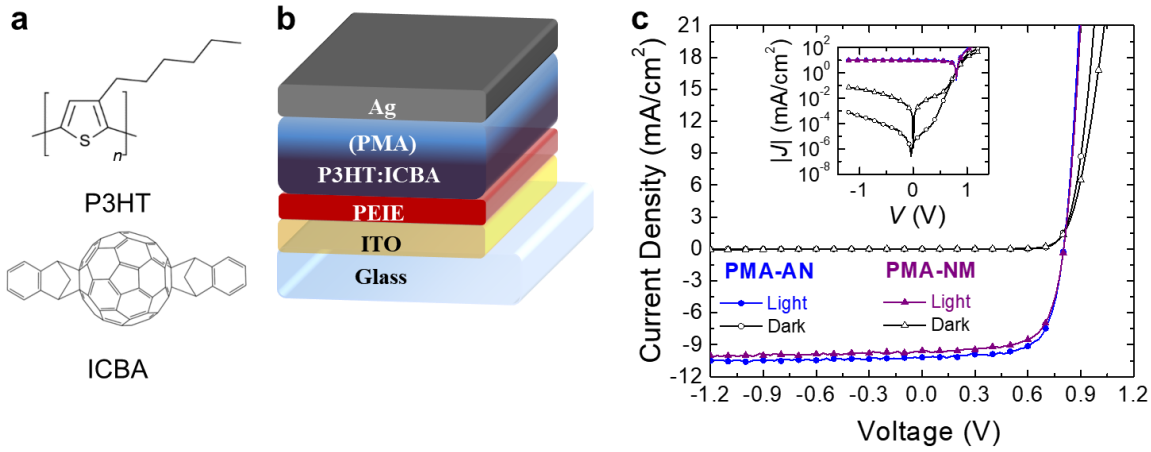

Figure 4-4. OPV devices doped with PMA in acetonitrile or nitromethane, measured in the dark and under 1-sun illumination. (a) Chemical structures of poly(3-hexylthiophene-2,5-diyl) (P3HT) and indene C_{60} bisadduct (ICBA). (b) OPV structure. (c) Direct comparison of *J–V* characteristics measured in the dark and under 1-sun illumination.

The data shows that the performance of PMA-doped OPV devices using PMA in acetonitrile is comparable to that of OPVs made using PMA in nitromethane or MoO_3, under simulated AM 1.5G solar illumination (Figure 4-4, Table 4-1 and Figure A-2).

Moreover, OPV devices that were immersed for longer times show comparable photovoltaic performance to those immersed for one min only, confirming that the effect saturates. Overall, these data validate the use of acetonitrile to fabricate OPVs with photovoltaic performance comparable to that of solar cells doped using PMA in nitromethane.

Table 4-1. Photovoltaic performance parameters measured under simulated 100 mW cm^{-2} AM 1.5G illumination. The data represents average values and standard deviations measured over a total of 24 samples.

Structure (comments)	J_{sc} (mA cm^{-2})	V_{oc} (mV)	FF	PCE (%)	Number of devices
ITO/PEIE/P3HT:ICBA (200 nm)/MoO_3/Ag (Reference)	9.3 ± 0.2	788 ± 6	71 ± 0	5.2 ± 0.1	5
ITO/PEIE/PMA-im-P3HT:ICBA (200 nm)/Ag *(PMA - NM, 1 min imm.)*	9.3 ± 0.4	804 ± 1	66 ± 1	4.9 ± 0.2	5
ITO/PEIE/PMA-im-P3HT:ICBA (200 nm)/Ag *(PMA - AN, 1 min imm.)*	9.9 ± 0.3	802 ± 5	68 ± 1	5.4 ± 0.2	5
ITO/PEIE/PMA-im-P3HT:ICBA (200 nm)/Ag *(PMA - AN, 10 min imm.)*	9.5 ± 0.4	810 ± 3	71 ± 1	5.4 ± 0.2	5
ITO/PEIE/PMA-im-P3HT:ICBA (200 nm)/Ag *(PMA - AN, 30 min imm.)*	9.0 ± 0.5	808 ± 4	70 ± 1	5.1 ± 0.3	4

However, longer OPV immersion time may be undesirable, as *J-V* characteristics of OPV devices immersed for 10 min and 30 min show an increase in their leakage current under reverse bias, when measured in the dark (see Figure A-3). These effects have been correlated in the past with a decreased parasitic shunt resistance, which is detrimental to the device performance under light intensities below 1-sun illumination [56, 96].

4.2.5 Stability of PMA doped OPVs in air

All unencapsulated OPV devices were further studied by measuring their photovoltaic performance after exposing them to air, in dark conditions. The results show that OPV devices doped using PMA, whether dissolved in nitromethane or acetonitrile, exhibit an s-shape in the four quadrant of their *J-V* characteristic. Interestingly, all s-shapes are eliminated after 10 min of light soaking under simulated AM 1.5G solar illumination.

In other words, the exposure to simulated sunlight corrects the observed s-shape. As reported previously [97], s-shapes observed in *J-V* characteristics of OPVs may be attributed to reversible changes of the work function value of indium-tin-oxide (ITO) under prolonged exposure to ultraviolet light in inert atmosphere, or air. Thus, we speculate that these s-shapes are caused by the adsorption of oxygen on the PEIE-treated ITO bottom contact, when OPV devices are exposed to air.

This is consistent with the removal of such s-shapes following light soaking, as UV irradiation produces desorption of oxygen from the ITO in inert atmosphere. Furthermore, if the light soaking mechanism is used before each measurement, OPVs made using PMA in nitromethane or acetonitrile remain stable for up to 524 h in air (Figure 4-5), retaining 80% of their initial PCE. Moreover, the appearance of an s-shape in the *J-V* characteristic of OPVs doped with PMA in acetonitrile is delayed, compared to OPVs doped with PMA in nitromethane. The difference is noticeable up to 10 h of air exposure, and seems negligible after 97 h of air exposure in all devices (see Figure A-4). Hence, OPV devices made using PMA in acetonitrile show increased air stability compared to similar devices fabricated using PMA in nitromethane. Finally, OPV devices made using an evaporated 10-nm-thick MoO_3 exhibit s-shapes in the fourth quadrant of their *J-V* characteristic. But, s-shapes comparable to those found in PMA-doped OPV devices degraded in air for 97 h appear after 524 h of similar exposure when using MoO_3 (see Figure A-5).

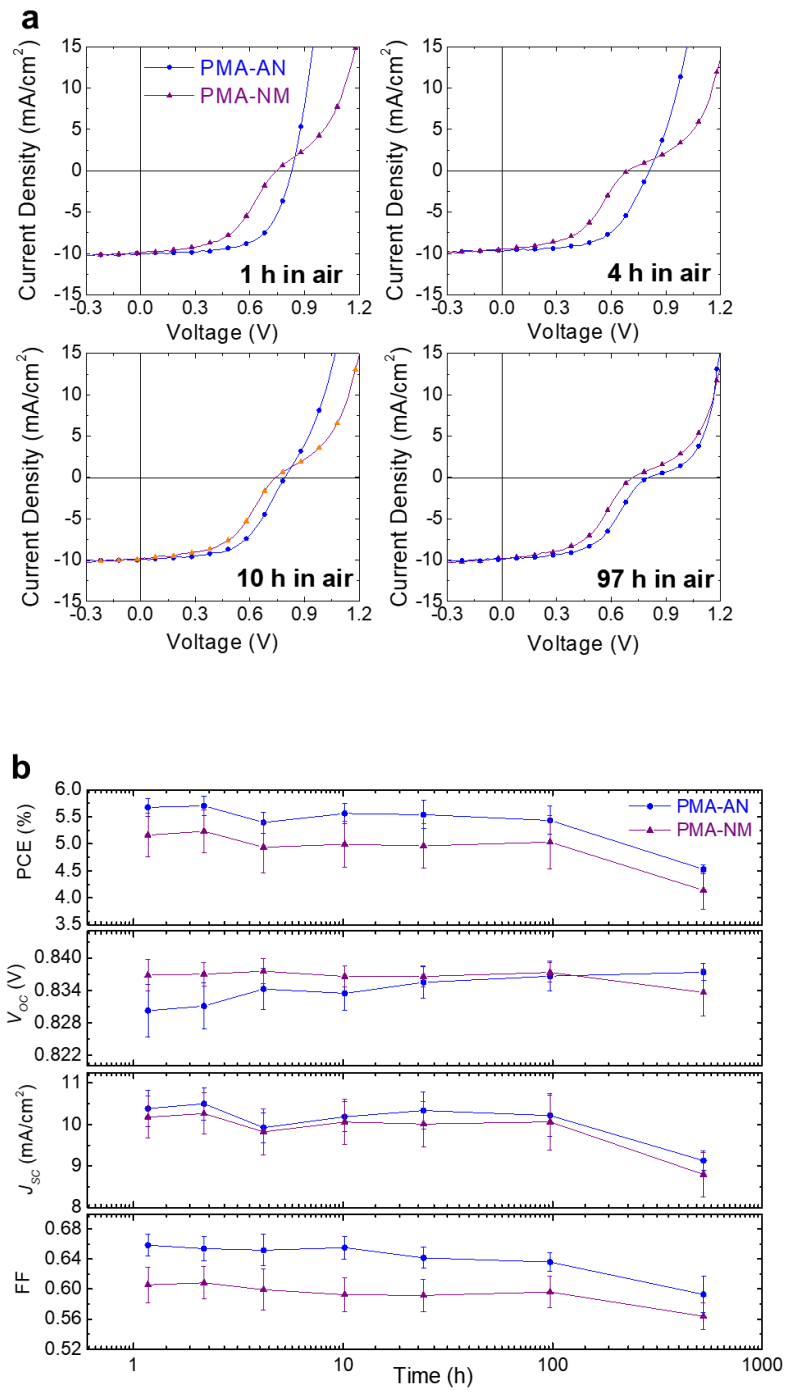

Figure 4-5. Air stability of OPV devices doped with PMA in acetonitrile or nitromethane. (a) *J–V* comparison of 200 nm-thick PMA-im-P3HT:ICBA OPVs doped using PMA–AN or PMA–NM. (b) Temporal evolution of photovoltaic parameters of 200 nm-thick PMA-im-P3HT:ICBA OPVs in air and in the dark.

4.3 Summary

The immersion of polymeric semiconducting films into a polyoxometalate (PMA) solution was found to lead to electrical doping over a limited depth, enabling the fabrication of organic photovoltaic devices with simplified geometry; yet, the technique was highly solvent selective and the use of nitromethane was found limiting. This chapter presents the use of acetonitrile as an alternative solvent for PMA. It is shown that acetonitrile enables *p*-type electrical doping of polymeric films following immersion into a PMA solution. Morphology studies on pristine and PMA doped P3HT films suggest that dopants reside in between polymer lamellae but cause no distortion to P3HT π-π stacking. Degradation studies reveal a superior stability of films doped with PMA in acetonitrile.

CHAPTER 5. MORPHOLOGY OF PMA-DOPED P3HT FILMS

5.1 Introduction

The application of solution-based electrical *p*-type doping of organic semiconductors to organic optoelectronic devices, as opposed to mere organic films, is not straightforward. Since most devices, including OPVs, are comprised of several layers, the ability to fabricate doping profiles vertically or laterally (i.e., to a limited depth or area extension), is critical to enable their operation. However, the fabrication of stable doping profiles in polymer films has proven challenging, as neither solution processing nor evaporation of dopants leads to vertical doping profiles due to fast diffusion on the length scale of the typical film thickness (~100 nm) [41].

While there have been attempts to fabricate doping profiles through lamination of several layers [76], there were no successful solution-based electrical doping profiles until December 2016. Then, Kolesov et al. reported a method to produce vertical doping profiles in organic semiconducting films following immersion into a PMA solution [68].

As discussed in detail in Chapter 4, this technique was optimized by replacing the processing solvent with acetonitrile. It was shown that the new PMA-solvent solution becomes more stable in air (compared to the use of nitromethane), without losing its doping ability. Additionally, organic solar cells fabricated using the updated approach showed improved operational stability when exposed to air.

Still, from a molecular perspective, the interplay between P3HT and PMA that leads to *p*-type electrical doping of the organic layer remains unclear. In other words, what are

the key variables that govern this process, and ultimately why this technique produces vertical doping profiles? Since the self-limiting nature of PMA doping distinguishes the technique from most solution-based electrical doping methods, to unravel the doping mechanism is key to further tailor the profile and penetration depth of dopants into organic semiconducting films.

To explore possible answers to these questions, this chapter focuses on analyzing the morphology of pristine and PMA doped P3HT films. By varying the immersion time and controlling the crystallinity of these films, the influence of these variables, if any, in the morphology of electrically *p*-type doped P3HT films, is studied.

5.2 Results and Discussion

5.2.1 Morphology of PMA doped P3HT films as a function of immersion time

The study began by evaluating how morphological changes in PMA doped semiconducting polymer films progress as a function of immersion time. This was determined by characterizing with GIWAXS the morphology of P3HT films after immersion into PMA dissolved in acetonitrile for either 10 s, 60 s or 600 s.

Figure 5-1 (a) shows the 2-D GIWAXS pattern of pristine and PMA doped P3HT films for 10 s, 60 s, and 600 s, while (b) highlights the out-of-plane and in-plane line profiles for each condition. Per the out-of-plane line profile, the pristine P3HT film features the expected (100), (200), and (300) diffraction peaks at q = 0.38 $Å^{-1}$, 0.76 $Å^{-1}$, and 1.14 $Å^{-1}$; and a broad π-π stacking peak at q = 1.66 $Å^{-1}$ with broad polar angle distribution, comprising both edge-on and face-on orientation with respect to the Si substrate. The broad

(in polar angle) π-π stacking peak is attributed to the coexistence of both face-on and edge-on molecular packing orientation in the film, consistent with the literature [98].

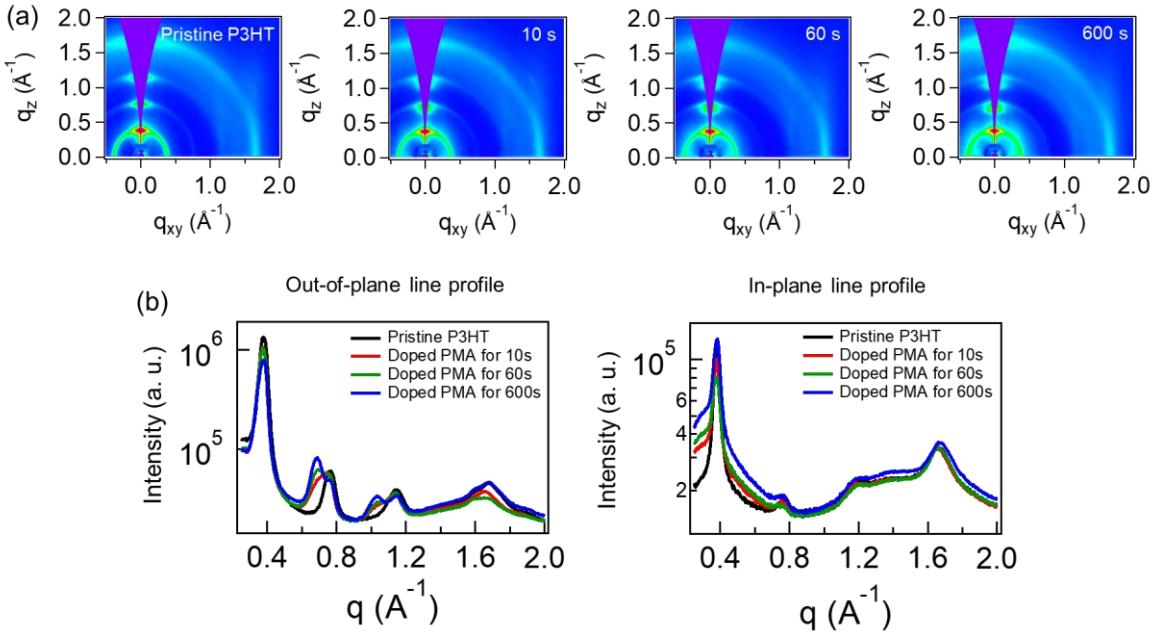

Figure 5-1. (a) 2-D GIWAXS patterns of pristine P3HT and PMA doped P3HT, were immersion time varies between 10 s, 60 s and 600 s. (b) Out-of-plane and in-plane line profiles for pristine and PMA doped P3HT.

As the P3HT film is doped by immersion in a 0.5 M solution of PMA in acetonitrile for 10 s (Figure 5-1 (b)), the (200) diffraction peak splits into two peaks at q = 0.69 Å^{-1} and 0.76 Å^{-1}. The peak at 0.76 Å^{-1} corresponds to pristine P3HT, whereas the new peak at 0.69 Å^{-1} is associated to PMA modifying the P3HT packing. The (300) diffraction signal also splits into two peaks, one at q = 1.03 Å^{-1} and another at 1.14 Å^{-1}. Similarly, the peak at 1.14 Å^{-1} corresponds to neat P3HT while the new peak at 1.03 Å^{-1} relates to PMA-modified P3HT packing. From these data it is clear that PMA becomes intercalated with P3HT lamellae, as reported in Chapter 4 for 1 minute immersion. While the lamellae *d*-spacing increases due to the intercalation, the π-π stacking peak does not shift in position.

Presumably, this implies that there are separated doped and undoped portions of the material.

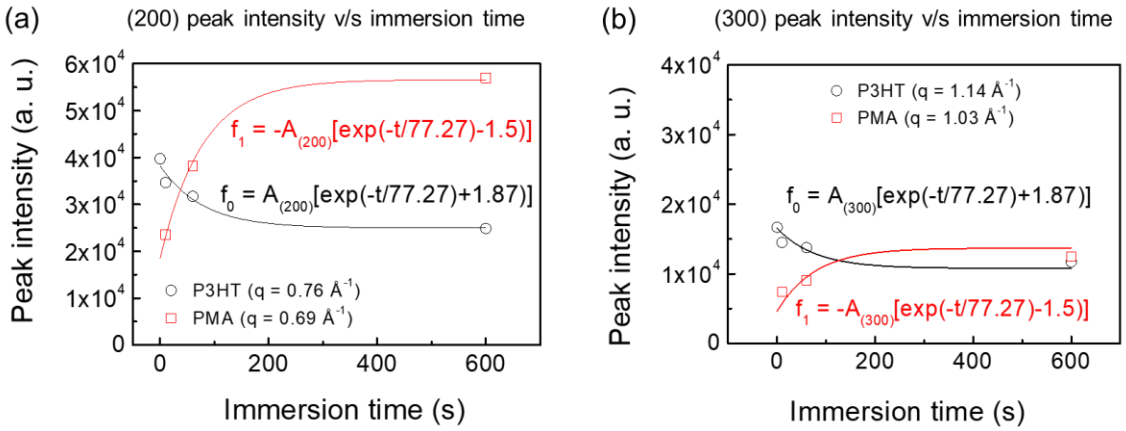

Figure 5-2. Intensity of the (200) diffraction peaks corresponding to pristine P3HT and PMA in (a), and the (300) diffraction peaks in (b). Profiles are fitted to an exponential decay function.

Further increasing the doping time to 60 s and 600 s correlates with peak intensity increases for the (100), (200), and (300) diffraction peaks, but their *q* position remains unchanged. A decreased intensity for neat P3HT peaks along with higher scattering intensity from PMA peaks suggests that more PMA intercalates into P3HT lamellae with longer immersion times. Figure 5-2 highlights these changes by comparing the intensity of the (200) and (300) diffraction peaks corresponding to neat P3HT and PMA-modified packing (calculation procedure reported elsewhere [71]). The results are in agreement with an exponential function fit which suggests that changes in peak intensity would be negligible after 200 s, in line with the self-limiting nature of the phenomena.

While out-of-plane line profiles of PMA doped P3HT exhibit distinctive peaks corresponding to neat P3HT and PMA nanoclusters for the (200) and (300) diffraction, the

(100) diffraction does not clearly split for any immersion time. At most, a tail develops towards smaller *q*-values. This suggests that the neat P3HT peak from the (100) diffraction is overlapping with the signal corresponding to PMA-modified P3HT packing, but additional 2-D GIWAXS patterns with various X-ray incident angles are required to confirm this claim (current incident angle is 0.12°). Varying the incidence angle would also provide a broad picture of the distribution of PMA nanoclusters into the doped film, as it would help characterizing regions closer to the surface and deeper into the sample.

Thus, the X-ray incidence angle was varied to 0.04°, 0.08°, 0.16° and 0.20° on the P3HT film immersed into PMA solution for 600 s. This sample was selected as its previous GIWAXS characterization (per Figure 5-1 (b)) suggests it contains the largest amount of PMA nanoclusters compared to all other samples immersed for shorter times. The out-of-plane line profiles are depicted in Figure 5-3 (a).

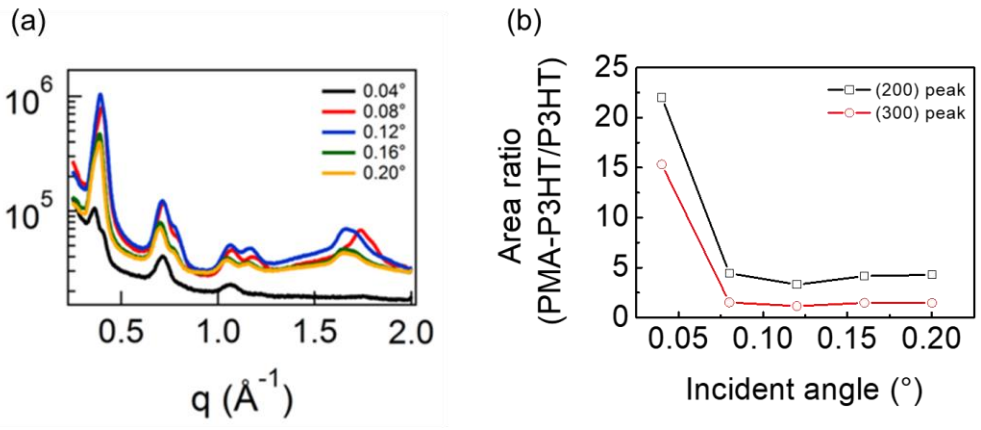

Figure 5-3. (a) Out-of-plane line profile from GIWAXS patterns taken at various incident angles in a P3HT sample immersed into PMA solution for 600 s. (b) Ratio of PMA to neat P3HT signals for diffractions (200) and (300) v/s angle of incidence.

With an X-ray incident angle of 0.04°, the (100) diffraction does split into two peaks as shown in Figure 5-3 (a), which indicates that neat P3HT and PMA overlap in the out-

of-plane profile taken at X-ray incidence of 0.12°. Moreover, the intensity of peaks correlated with pristine and PMA-immersed P3HT changes with angle of incidence. Figure 5-3 (b) plots the ratio between the area of the PMA peak and the pristine P3HT peak (calculation procedure reported elsewhere [71]). These data show that PMA nanoclusters penetrate only down to a limited depth of the P3HT film and concentrate close to the surface of the sample, which is consistent with previous characterizations of the dopant distribution into the depth of the film (ToF SIMS, XPS). In essence, the data confirms that the P3HT crystal is altered by PMA.

5.2.2 Comparison of regioregular v/s regiorandom P3HT films after doping

It remains unclear whether PMA nanoclusters are located in amorphous regions in addition to those in the crystalline phase, and if they do, whether they dope amorphous P3HT. Thus, additional UV-Vis-NIR spectroscopy and sheet resistance measurements were conducted on amorphous (regiorandom or rra) and semi-crystalline (regioregular or rre) P3HT. Regiorandom P3HT was chosen because it maintains a disordered morphology in the solid state due to steric repulsion between its randomly oriented side chains. Also, its *IE*, while larger than that of P3HT, is still higher than the *EA* of the PMA nanocluster.

UV-Vis-NIR spectroscopy in Figure 5-4 shows changes in the near infrared that can be correlated to a polaron absorption band in both regiorandom and regioregular P3HT, which suggests electrical *p*-type doping of both phases. Furthermore, when crystallinity is controlled in regioregular P3HT (Figure 5-4 (b)), the normalized spectroscopic transmittance change of the main absorption band increases from around 5% to almost 20%. Thus, it appears that as more crystals become available, the absorption band of the

film is decreased, as each of these crystals become *p*-type doped. Finally, a change of five orders of magnitude in the sheet resistance of regiorandom and regioregular P3HT following 1 min immersion in PMA – acetonitrile (Figure 5-4 (d)), also suggests electrical *p*-type doping.

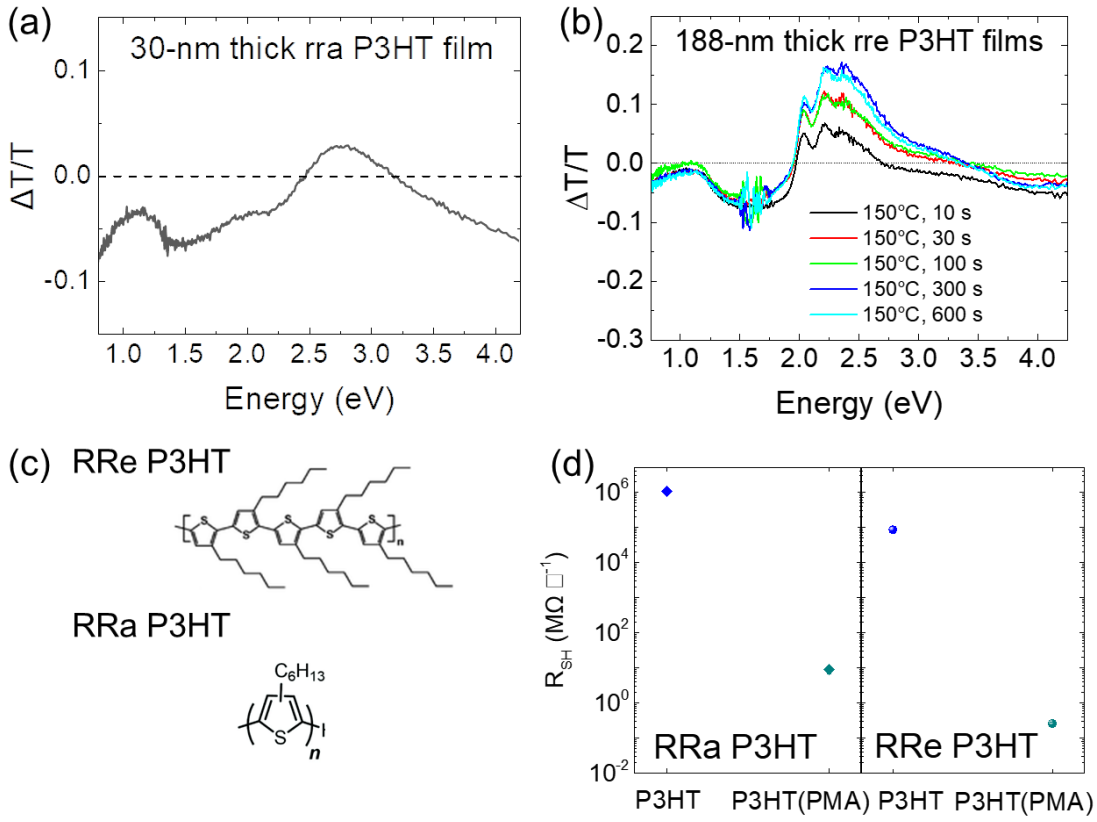

Figure 5-4. Normalized change in transmittance in rra P3HT (a) after 1 min PMA immersion and rre P3HT (b), having thermally annealed samples for various times at 150 ºC. (c) Molecular structures of rre and rra P3HT. (d) Sheet resistance in pristine P3HT, both rra and rre, and after 1 min immersion into PMA solution.

While it is clear that both amorphous and crystalline phases in P3HT become doped, the morphology study does not provide evidence to rationalize why PMA nanoclusters allocate near the surface of P3HT films while most other *p*-type molecular dopants (e.g.,

F4TCNQ) penetrate the full volume when applied to the semiconductor. It is speculated that these dopants might fit more easily into amorphous domains of acetonitrile swollen P3HT, compared to the bulkier PMA nanocluster. Indeed, the PMA anion, containing a phosphate moiety attached to twelve molybdenum trioxide subunits has a total diameter of 10.2 ± 0.5 Å. This is large compared to the expansion quantified using GIWAXS, which also suggests that the PMA content in the crystalline phase should be small. Furthermore, while acetonitrile is not a good solvent for P3HT, it has been shown that it swells it to a limited extent [99].

5.3 Summary

This chapter reports on the morphology of pristine and PMA doped P3HT films. GIWAXS data suggests that P3HT crystals become altered following immersion into a PMA-acetonitrile solution. The data suggests that dopant molecules allocate in between polymer lamellae within crystalline phases down to a limited depth from the surface, regardless of immersion time. Last, UV-Vis-NIR spectroscopy and sheet resistance measurements support electrical *p*-type doping of both crystalline and amorphous phases in P3HT films.

CHAPTER 6. INCREASING FREE VOLUME IN CONJUGATED POLYMER FILMS TO FACILITATE ELECTRICAL DOPING WITH PMA

6.1 Introduction

P-type (or *n*-type) dopants are generally neutral organic molecules that can accept (or donate) a charge carrier from (or to) an organic semiconducting host. The increase in electrical conductivity of the doped host arises from the addition of charge carriers and their ability to move under the influence of an electric field [41]. As such, molecular dopants have been applied extensively to various organic electronic device platforms, including OPVs [100-106].

In the case of OPVs, molecular *p*- and *n*-type dopants have been used to create *p*-*i*-*n* structures with a built-in potential that favors charge collection without the use of expensive, brittle or unstable materials at opposite electrodes [107-109]. Furthermore, the use of molecular *p*-type dopants in the photoactive layer of OPVs has been linked to improvements in the OPV's power conversion efficiency, presumably due to dopant-induced filling of traps [110, 111].

Yet, the application of molecular *p*-type dopants to OPV devices has proven challenging because most of them diffuse within the electronic device in days [112, 113]. Since OPVs are comprised of several organic layers, selective doping of a limited region is required to ensure operational stability. For optimal performance at an extended lifetime, dopants need to remain in the domain where they were inserted or printed.

The processing of molecular dopants is another challenge. While vacuum techniques allow the co-deposition of dopants and the molecules being electrically doped, the mixing of dopants with polymers processed from solution can be challenging as the interaction of the dopant and polymer in solution can affect rheological properties of the solution. In some cases, this interaction can lead to the precipitation of the polymer after addition of the dopant in solution.

PMA is a solution-processible *p*-type dopant that was shown to diffuse down to a limited depth of 60 nm from the surface of the film and remain stable for at least 280 h at 60 °C. This diffusion was shown to occur when the polymer film is immersed in a solution of either nitromethane or acetonitrile containing PMA. This particular feature of solution-based PMA doping enabled the first demonstration of a single-layer OPV device [68].

However, a few challenges remain to be addressed before extending the scope and scale of applications of PMA doping to emerging conjugated polymers, small molecules and other organic electronic device platforms. First, while *p*-type doping has been demonstrated using PMA dissolved in nitromethane and acetonitrile (Chapter 4), only these two solvents enable the process to take place efficiently. In other words, the application of this method to organic semiconducting films remains solvent-dependent and the reason behind this phenomenon is poorly understood.

Secondly, there is evidence from Secondary Ion Mass Spectrometry (SIMS) and X-ray Photoelectron Spectroscopy (XPS) measurements on PMA doped conjugated polymer films that PMA penetrate such films down to a limited depth from the surface and remain

stable in their confinement up to 280 h at 60 °C [68]. Yet, the mechanism behind the formation of such doping profile remains elusive.

Grazing-Incidence Wide-Angle X-ray Scattering (GIWAXS) measurements provided evidence of a change of polymer morphology which was attributed to the intercalation of dopants between lamellae (Chapter 5). Still, it remains unclear whether electrical doping occurs preferentially on the amorphous or crystalline phases, and what is the role of these phases in the formation of the dopant profile.

Furthermore, in view of the large size of the Keggin structure of PMA, it remains unclear if the nanocluster structure is preserved during the doping process or if it breaks up into smaller constituents. Still, electrochemistry studies using PMA suggest that the PMA Keggin structure remains intact after dissolving it in various solvents [59-61].

These questions are examined by controlling the free volume in conjugated polymer films and evaluating its role in solution-based electrical *p*-type doping with PMA. By expanding conjugated polymer films following two approaches and doping them with PMA nanoclusters, the effect of free volume in the achievable doping level is evaluated. ^{31}P nuclear magnetic resonance spectroscopy (NMR) and Fourier transform infrared (FTIR) spectroscopy experiments are carried out to assess the stability of the Keggin structure.

6.2 Results and Discussion

6.2.1 Integrity of the PMA Keggin structure throughout the doping process

Previous studies in Chapters 4 and 5 showed that the PMA doping technique is strongly dependent on the choice of the solvent. It was hypothesized that such dependency might come from (1) a dominant chemical interaction between solvent and PMA nanoclusters, which modifies the Keggin structure of PMA; or (2) a combination of a charge transfer reaction and a mass transport process. The latter would include solvent infiltration in addition to the charge transfer reaction that enables electrical *p*-type doping.

To test hypothesis (1), a first set of experiments aims at evaluating whether the Keggin structure of PMA is preserved when dissolved in acetonitrile. To this end, its chemical structure is characterized in solution using ^{31}P NMR. It is worth noting that the Keggin structure of PMA breaks up if the material is heated to 400 ºC for 30 min, releasing a phosphate ion and twelve molybdenum trioxide units [114]. Thus, rupture of the Keggin structure at room temperature upon dissolving in acetonitrile or nitromethane is unlikely.

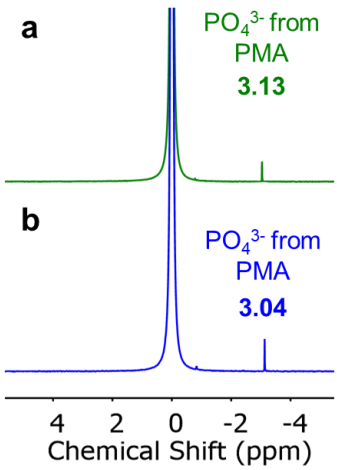

Figure 6-1. ^{31}P NMR study. (a) ^{31}P NMR of PMA in deuterated water. (b) ^{31}P NMR of PMA in acetonitrile at 0.5 M concentration, into deuterated water.

^{31}P NMR studies indicate a chemical shift of 0.09 ppm relative to the reference PO_4^{3-} phosphate standard, when dissolving PMA into acetonitrile at 0.5 M concentration

(Figure 6-1). While this may correlate with changes in the outer region of a given population of nanoclusters, it is not significant given that there is a change in the solvation environment and perhaps an average protonation state. Overall, this change does not support disruption of the Keggin structure, consistent with the literature [115].

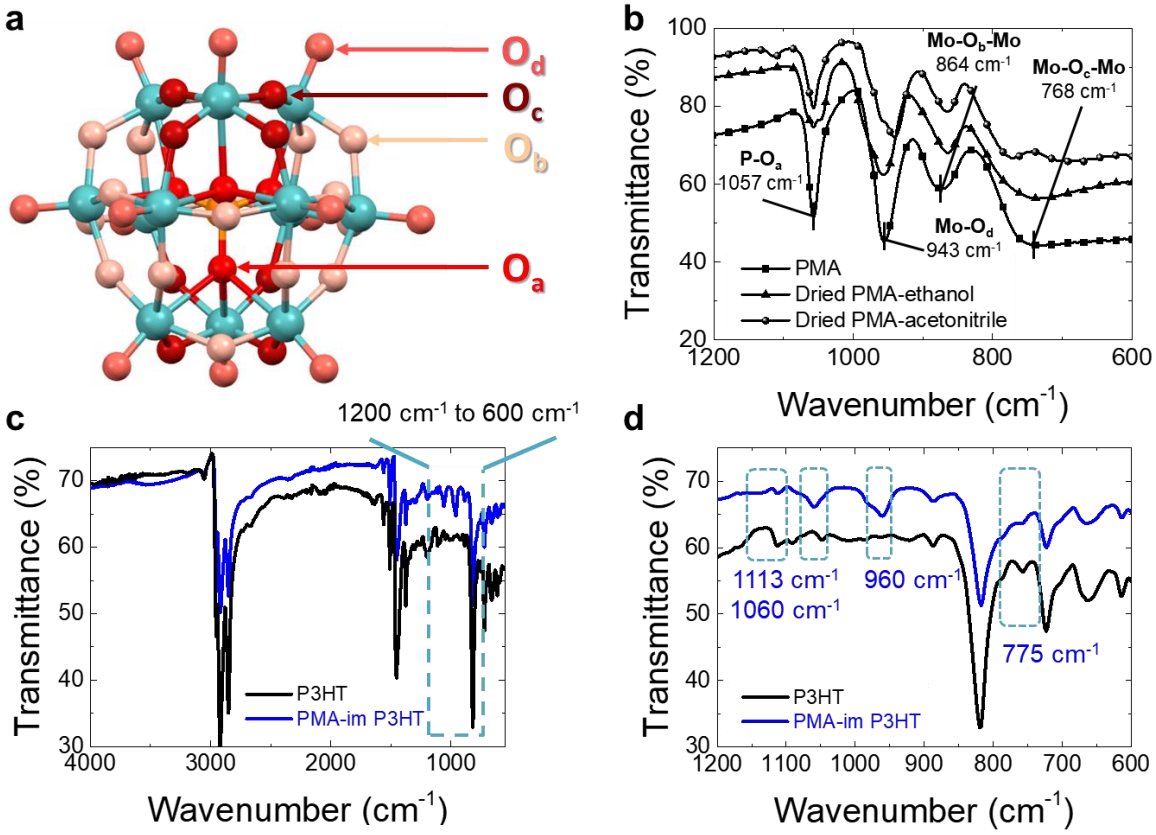

Figure 6-2. FTIR studies. (a) Chemical structure of PMA and nomenclature for oxygen atoms. (b) FTIR spectrum of pristine PMA, PMA dissolved in ethanol and dried, and PMA dissolved in acetonitrile and dried. (c) FTIR spectrum of pristine and PMA-immersed P3HT. (d) FTIR spectrum of pristine and PMA-immersed P3HT between 600 cm^{-1} and 1200 cm^{-1} wavenumber.

Since ^{31}P NMR data for PMA dissolved in acetonitrile exhibits a non-negligible chemical shift for the phosphate ion, potential changes to the chemical structure of PMA before doping are further investigated using FTIR spectroscopy. The spectra of PMA were

characterized before dissolving PMA in acetonitrile and after dissolving with full removal of the solvent. Specifically, the infrared (IR) spectra of pristine PMA nanoclusters were compared to that of PMA nanoclusters dissolved in ethanol or acetonitrile and dried in air. The results show negligible changes for the P-O_a bond, but variations between 10 to 20 cm^{-1} in all other structural bonds. In particular, after dissolving in acetonitrile and drying, the Mo-O_d bond stretching frequency decreases from 956 cm^{-1} to 943 cm^{-1}. The Mo-O_b-Mo stretch changes from 873 cm^{-1} to 864 cm^{-1}. Finally, the Mo-O_c-Mo stretch decreases from 727 cm^{-1} to 705 cm^{-1}, and an additional peak appears at 768 cm^{-1} (Figure 6-2, (a) and (b)).

While weak interactions between PMA and solvent molecules may explain these variations, the data confirms the presence of all four peaks of pristine PMA nanoclusters [114, 116, 117]. Some changes may be expected if the average oxidation state of Mo atoms changes. This would lead to a structure with the same symmetry but slightly weaker bonds, which is reasonable if there are a few extra electrons spread over 12 Mo atoms. The data implies that, within the resolution of the FTIR tool, the Keggin structure of PMA appears to be preserved after solvation in acetonitrile or ethanol. That is, MoO_3 subunits do not detach from the phosphate ion.

Still, it remains unclear what happens with the chemical structure of PMA after electrical *p*-type doping has taken place. In other words, are there any changes to the Keggin structure after it becomes in close contact to the organic semiconductor? To address this question, IR spectroscopy studies of P3HT and PMA immersed P3HT were conducted. Specifically, the IR spectra of neat P3HT was compared to the spectra of P3HT immersed into a PMA-acetonitrile solution for 1 min. The results indicate changes on the spectra of PMA-immersed P3HT compared to pristine P3HT only between 1200 cm^{-1} to 600 cm^{-1},

which correlate with the main IR peaks of PMA. While a detailed analysis of the IR spectra of pristine P3HT over 1,200 cm^{-1} is beyond the scope of this work, the data for pure P3HT between 1,200 cm^{-1} and 4,000 cm^{-1} appear to match several references [118-120]. In the region between 1,200 cm^{-1} and 600 cm^{-1}, a variation in transmittance of PMA-immersed P3HT at 1,113 cm^{-1} matches a peak of PMA dissolved in acetonitrile and dried. Furthermore, a new peak at 1,060 cm^{-1} in PMA-immersed P3HT correlates well with the P-O_a bond of PMA nanoclusters: the link between the phosphate ion and all twelve MoO_3 subunits. Finally, an asymmetry in the IR spectra of PMA-immersed P3HT at 775 cm^{-1} matches the Mo-O_c-Mo stretch (Figure 6-2, (c) and (d)). In summary, all changes to the IR spectra between pristine P3HT and PMA immersed P3HT correlate well with structural PMA bonds or stretches. This suggest that the Keggin structure of PMA interacting with P3HT remain largely unchanged, at least regarding its symmetry.

6.2.2 PMA doping of PBDB-T films at room temperature without expansion

Next, the second hypothesis to explain the solvent dependency of PMA doping is addressed. This hypothesis suggests that the method involves both a charge transfer reaction [68] and a mass transport process. In other words, solvent infiltration would play a key role in enabling the penetration of dopants into the free volume of organic films, facilitating electrical *p*-type doping. Furthermore, if more free volume becomes available, PMA dopants would have more space to infiltrate the film.

Interestingly, while acetonitrile is not a good solvent for most conjugated polymers, it has been shown that it swells them by creating increased free volume [99]. Also, phenomenological models for the infiltration of molecules into polymer films, mostly

through atomic layer deposition, result in self-limited profiles similar to those observed following PMA doping: nearly exponential profiles whose extension depends on the available free volume of the polymer film, among other variables [121].

To test the hypothesized role of free volume in the PMA doping process, it is key to find conjugated polymers that do not become heavily doped after immersion into PMA-acetonitrile at room temperature. To fabricate films with such materials and vary their available free volume would provide a path to confirm or disprove this claim.

The conjugated polymer Poly[(2,6-(4,8-bis(5-(2-ethylhexyl)thiophen-2-yl)-benzo[1,2-b:4,5-b']dithiophene))-alt-(5,5-(1',3'-di-2-thienyl-5',7'-bis(2-ethylhexyl)benzo[1',2'-c:4',5'-c']dithiophene-4,8-dione)] or PBDB-T fulfills aforementioned criteria: films of it do not become heavily doped when immersed into PMA-acetonitrile at room temperature. This was tested experimentally by fabricating 40 nm-thick PBDB-T films from solution on ITO substrates and immersing them into a 0.5 M PMA-acetonitrile solution for 1 min at room temperature. Following immersion, such films exhibit a work function change of 0.14 ± 0.03 eV measured using a Kelvin probe, and show a bleaching of their main absorption bands up to 1% with respect to pristine films (Figure B-1). This can be compared to a work function change of 0.3 to 0.4 eV and 5-10% bleaching of the main absorption bands of films of P3HT, PffBT4T-2OD (PCE11), PCDTBT and many others [68]. While the *IE* of PBDB-T is larger than that of P3HT, it is still not as large as that of PCDTBT for example, so the *IE* of the material by itself does not explain the issue.

6.2.3 PMA doping of expanded PBDB-T films

Since the free volume of conjugated polymer films varies with temperature [121], the doping treatment was modified by heating both the PMA-acetonitrile solution and the organic semiconducting film for 15 min before immersion (Figure 6-3, (a) and (b)). The expansion of a PBDB-T film, was measured using variable angle spectroscopic ellipsometry (Figure 6-3 (c)), with temperatures in the range between 10 ºC and 140 ºC (model parameters in Figure B-2). Transmittance and work function changes were measured as a function of temperature.

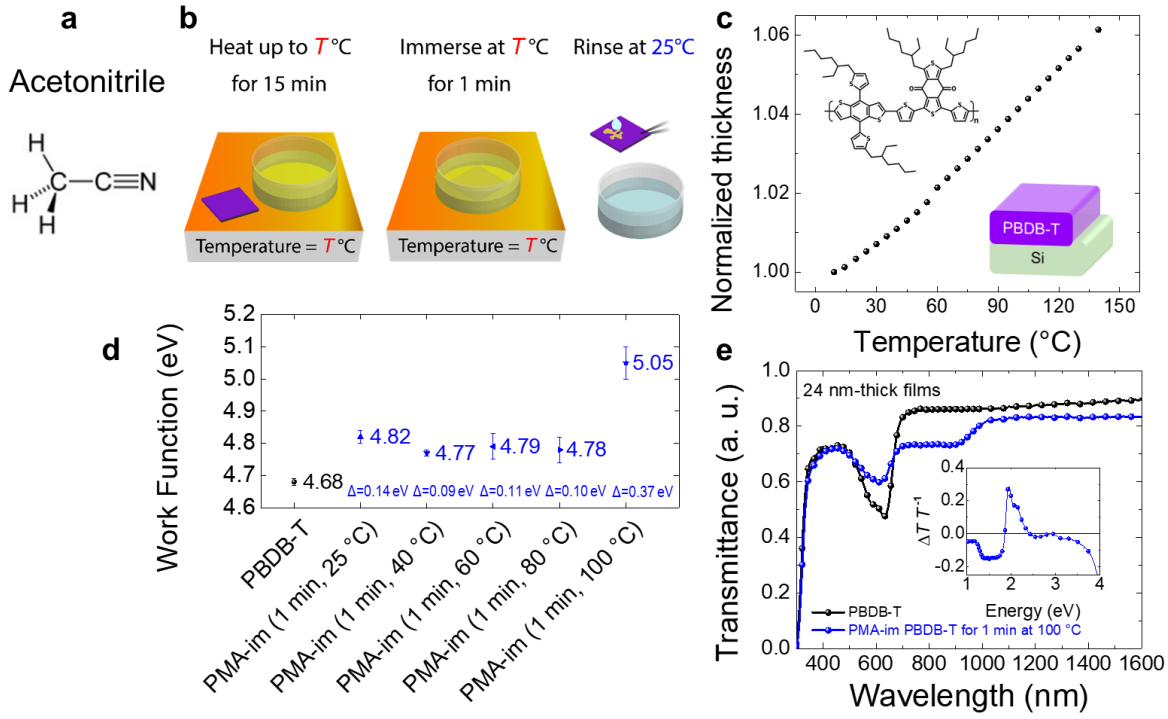

Figure 6-3. Doping of PBDB-T through immersion into hot PMA-acetonitrile solution. (a) Molecular structure of acetonitrile. (b) Sketch of PMA-treatment: (1) heat up pristine PBDB-T and PMA solution, (2) immerse PBDB-T into hot PMA solution and (3) rinse PBDB-T film with pure acetonitrile. (c) Normalized thickness v/s temperature of a PBDB-T film per spectroscopic ellipsometry. (d) Work functions of PBDB-T films treated with PMA solution (average over three measurements in no less than 2 samples per condition). (e) Transmittance of PBDB-T film immersed into

PMA-acetonitrile at 100 °C. Inset: normalized change of transmittance as a function of energy.

Work function and transmittance of PMA-immersed PBDB-T films are consistent with an increased doping level, comparable to what was previously observed in PMA doped P3HT. Regarding the work function, at 100 ºC, an increase of 0.37 ± 0.05 eV is measured in PBDB-T films after 1 min immersion (Figure 6-3 (d)). The normalized change of transmittance reveals spectral signatures comparable to those reported for PMA-immersed P3HT [68] (Figure 6-3 (e)).

Furthermore, PBDB-T films following immersion into hot PMA solution become less soluble in their processing solvent (in this case, chlorobenzene). This phenomenon is observed even if the doping level is lower than the one achieved through immersion into PMA-acetonitrile solutions at 100 ºC for 1 min. For example, by heating a sample and PMA-acetonitrile solution at 80 ºC prior to 1 min immersion, a work function change of only 0.10 ± 0.04 eV is measured. Yet, the film can be rinsed with chlorobenzene without washing it away (see Figure B-3). Moreover, after this rinsing step, the work function increases to 0.16 ± 0.01 eV, which suggests removal of undoped semiconductor.

Heating up both the PMA-acetonitrile solution and the PBDB-T film before immersion supports the proposed hypothesis about the role of the film free volume in the doping process. Yet, these results should be taken with caution. First, it remains unclear whether the reactivity between PMA and the conjugated polymer changes with temperature. Furthermore, as the solvent evaporates from the hot solution prior to film immersion, the concentration of PMA gradually increases. Last, a heating step increases

the energy budget of the doping technique and becomes harder to control compared to room temperature processing.

In what follows, another method to vary the free volume of conjugated polymers is reported. This alternative approach is based on solvent swelling [122]. Specifically, if swelling solvents are homogeneously combined with PMA solutions and coated onto the film surface, higher and potentially controllable levels of *p*-type electrical doping may be achievable at room temperature. Furthermore, acetonitrile might be replaced as the solvent for PMA.

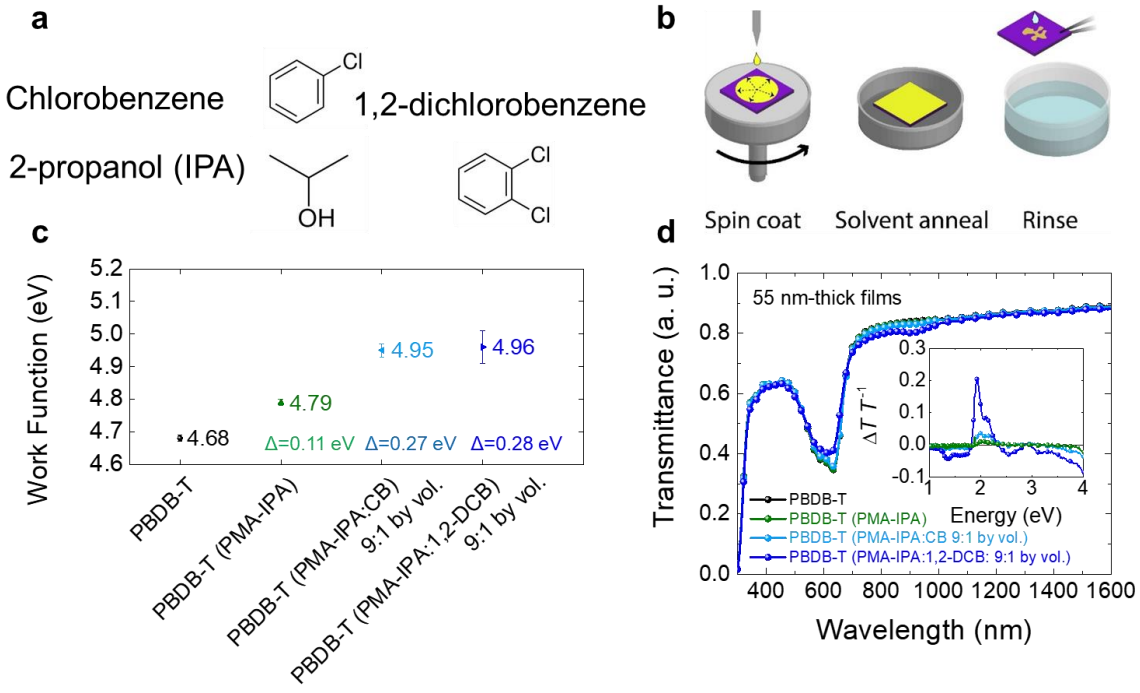

Figure 6-4. PMA-doping of PBDB-T through solvent swelling. (a) Molecular structures of chlorobenzene, 1,2-dichlorobenzene and 2-propanol. (b) Sketch of PMA treatment: (1) spin coat PMA dissolved in 2-propanol with a swelling solvent that is miscible in 2-propanol, (2) solvent anneal until all solvents evaporate and (3) rinse with pure 2-propanol. (c) Work function of PBDB-T films after spin coating PMA dissolved in 2-propanol with swelling solvents (averages over three measurements per sample in no less than 2 samples per condition). (d) Transmittance of PBDB-T films

after spin coating PMA dissolved in 2-propanol with swelling solvents. Inset: normalized change of transmittance as a function of energy.

Yet, several conditions need to be controlled for successful implementation of this method. First, the solvent for PMA needs to be miscible with swelling solvents at room temperature. Otherwise, solvents will phase separate and PMA will not penetrate further into the film. Additionally, the combined solution needs to swell the organic film but not fully wash it away. Typical strategies to achieve this are based on combining 'orthogonal' solvents, e.g., chlorobenzene and dichloromethane [123]. After careful consideration of previously described conditions, 2-propanol was chosen to dissolve PMA, and chlorobenzene and 1,2-dichlorobenzene were used to swell PBDB-T films. As required, 2-propanol solubilizes PMA and is miscible with chlorobenzene and 1,2-dichlorobenzene at room temperature.

Work function and transmittance changes of PBDB-T films treated with a liquid blend of PMA dissolved in 2-propanol and a swelling solvent are consistent with an increased doping level, with respect to immersion at room temperature without film expansion (sketch of PMA treatment in Figure 6-4, (a) and (b)). Regarding the work function, when using chlorobenzene or 1,2-dichlorobenzene mixed with PMA in 2-propanol, changes of 0.27 ± 0.02 eV and 0.28 ± 0.05 eV are measured, respectively (Figure 6-4 (c)). The normalized change of transmittance reveals bleaching of the main absorption band up to 20% and an emerging absorption band in the near that could be correlated to polaron absorption (Figure 6-4 (d)). These changes are comparable to those reported for PMA-immersed P3HT [68].

6.3 Summary

In this chapter, the free volume in polymer films and its role in solution-based electrical *p*-type doping using PMA are studied. Polymer film free volume was controlled using two approaches. One is based on heating both the PMA solution and the film prior to immersion. The second is based on coating the polymer film with a liquid blend that contains PMA solution and a swelling solvent. ^{31}P NMR and FTIR experiments indicate that the Keggin structure appears to be preserved throughout the doping process. Results show that increasing free volume is important to provide enough diffusivity for the PMA Keggin structure to penetrate into the polymer film and dope it electrically.

CHAPTER 7. CONCLUSIONS AND FUTURE WORK

7.1 Conclusions

First, an alternative, stable solvent to dissolve PMA that also enables electrical *p*-type doping of organic semiconductors down to a limited depth from the surface is reported. It is concluded that the use of nitromethane as the solvent of PMA is not critical to enable electrical *p*-type doping of organic semiconducting films. Instead, acetonitrile, when used to dissolve the polyoxometalate, produces organic films with comparable optical and electrical properties than those immersed in PMA dissolved in nitromethane.

Most importantly, the dopant profile resulting from immersion of conjugated polymer films into PMA-nitromethane is reproduced if such films are immersed into a solution of PMA dissolved in acetonitrile, as evidenced from mass spectrometry. Furthermore, OPV devices with a photoactive layer immersed into PMA-acetonitrile for 1 min showed increased stability (that is, a delayed appearance of an s-shape in the four quadrant of the *J-V* characteristic under 1-sun illumination), when exposed to atmosphere conditions, compared to reference devices fabricated using PMA in nitromethane.

The morphological characterization of PMA immersed P3HT films using GIWAXS showed that crystalline phases inside these films become altered following PMA doping. The data suggests that dopant molecules allocate in between polymer lamellae down to a limited depth from the surface. Yet, immersion time does not change the location of dopants within P3HT crystalline phases. While doping level progresses with immersion time as evidenced by the intensity of the signal corresponding to PMA in GIWAXS

measurements, doping appears to saturate before 10 minutes of immersion time, in line with previous findings. Additionally, it is concluded that both crystalline and amorphous phases of P3HT films become electrically *p*-type doped, as supported by UV-Vis-NIR spectroscopy and sheet resistance measurements of regiorandom and regioregular P3HT films.

At this point, the PMA doping technique was shown to be strongly dependent on the choice of solvent, particularly nitromethane and acetonitrile. It was hypothesized that such dependency might come from (1) a dominant chemical interaction between solvent and PMA nanoclusters, which would modify the Keggin structure of PMA; or (2) a mass transport process, in which infiltration of solvent molecules into the available space of conjugated polymer films may play a role in facilitating electrical *p*-type doping with PMA.

The first hypothesis was discarded, as ^{31}P NMR and FTIR experiments indicate that the Keggin structure of PMA appears to be preserved throughout the doping process. Thus, the second hypothesis to explain the solvent dependency of PMA doping was addressed. To this end, the free volume of conjugated polymer films and its influence in solution-based electrical *p*-type doping using PMA were investigated.

Films of the conjugated polymer PBDB-T were expanded, and their optoelectronic properties were measured following PMA doping. The free volume was varied by either heating the films and solutions, or through a new method based on solvent swelling. Results showed an increase in their work function by up to 0.37 eV and changes in their spectroscopic transmittance comparable to those reported for PMA-immersed P3HT films. Yet, if PBDB-T films were not expanded, electrical doping only increased the work

function by 0.14 eV and only negligible changes in their transmittance spectra were observed. It is concluded that by expanding conjugated polymer films, it is possible to increase their doping level following PMA doping. The infiltration of dopant and solvent molecules into the available space of these films provides a possible explanation to the previously observed solvent dependency of the technique. It is concluded that the free volume of conjugated polymer films is important to enable the PMA Keggin structure to penetrate into the film and dope it electrically.

7.2 Future Work

To extend the scope and scale of applications of electrical *p*-type doping of conjugated polymer films and bulk heterojunctions with PMA, several topics may be explored in the future.

First, it is desirable to elucidate the cause behind the accelerated but seemingly reversible degradation that takes places on PMA doped OPVs exposed to air. It remains unclear whether this degradation is in any way caused or accelerated by PMA.

Also, no fundamental physical limit has been found to extend the use of PMA doping to OPV devices with ternary or quaternary photoactive layers. That is, two ‘acceptor-like materials’ (or sometimes referred to as ‘electron-transport materials’) and one ‘donor-like material’ (or sometimes referred to as ‘hole-transport material’), vice versa, or two of each kind, inside the photoactive layer.

Furthermore, this doping technique might enable to simplify the fabrication of state-of-the-art OPV devices with power conversion efficiencies over 15% [124-127]. Yet, to

evaluate this hypothesis it is critical to test whether PMA doping degrades state-of-the-art materials like 3,9-bis(2-methylene-(3-(1,1-dicyanomethylene)-indanone))-5,5,11,11-tetrakis(4-hexylphenyl)-dithieno[2,3-d:2’,3’-d’]-s-indaceno[1,2-b:5,6-b’]dithiophene or ITIC, and also 2,2'-((2Z,2'Z)-((12,13-bis(2-ethylhexyl)-3,9-diundecyl-12,13-dihydro-[1,2,5]thiadiazolo[3,4-e]thieno[2",3’’:4’,5']thieno[2',3':4,5]pyrrolo[3,2-g]thieno[2',3':4,5]thieno[3,2-b]indole-2,10-diyl)bis(methanylylidene))bis(5,6-difluoro-3-oxo-2,3-dihydro-1H-indene-2,1-diylidene))dimalononitrile (or simply ‘BTP-4F’ or ‘Y6’), when these materials are in the solid state.

From a fundamental perspective, it would be useful to propose a model that fully explains the doping mechanism and provides insights to design other *p*-type and *n*-type dopants, either for OPV devices or other organic electronic platforms. Such a model should describe how PMA nanoclusters penetrate the surface of conjugated polymer films, diffuse into the free volume of such films and ultimately become entrapped, forming a seemingly stable doping profile at room temperature. While it is likely that the entrapment of PMA nanoclusters is caused by the charge transfer reaction that leads to *p*-type electrical doping as evidenced in previous work [68], at this point this claim is merely speculative.

Last, from a fabrication perspective, it would be desirable to incorporate the PMA doping technique into a process that manufactures OPV modules with areas larger than 0.1 cm^2. Since several of such processes replace vacuum-evaporated Ag contacts with slot-die coated Ag nanowires [128, 129], it might be possible to assess the impact of incorporating PMA doping in a vacuum-free fabrication process. These actions would aim at assessing whether PMA doping is compatible with industrial manufacturing.

7.3 Publications and Patents

[1] **F.A. Larrain**, T.-Y. Huang, C.H. Borca, C. Fuentes-Hernandez, H. Yan, S.A. Schneider, W.F. Chou, V.A. Rodriguez-Toro, H.-G. Steinruck, C. Cao, C. David Sherrill, B. Kippelen & M.F. Toney, *Morphology of organic semiconductors electrically doped from solution using phosphomolybdic acid*. Chemistry of Materials, 2019. **31(**17): p. 6677–6683.

[2] Y. Park, C. Fuentes-Hernandez, X. Jia, **F.A. Larrain**, J. Zhang, S.R. Marder & B. Kippelen, *Measurements of the field-effect electron mobility of the acceptor ITIC.* Organic Electronics, 2018. **58**: p. 290-293.

[3] **F.A. Larrain**, C. Fuentes-Hernandez, W.-F. Chou, V.A. Rodriguez-Toro, T.-Y. Huang, M.F. Toney & B. Kippelen, *Stable solvent for solution-based electrical doping of semiconducting polymer films and its application to organic solar cells*. Energy and Environmental Science, 2018. **11**: p. 2216-2224.

[4] H.K. Kim, A.S. Hyla, P. Winget, H. Li, C.M. Wyss, A.J. Jordan, **F.A. Larrain**, J.P. Sadighi, C. Fuentes-Hernandez, B. Kippelen, J.-L. Brédas, S. Barlow & S.R. Marder, *Reduction of the Work Function of Gold by N-Heterocyclic Carbenes*. Chemistry of Materials, 2017. **29**(8): p. 3403–3411.

[5] V.A. Kolesov, C. Fuentes-Hernandez, W.-F. Chou, N. Aizawa, **F.A. Larrain**, M. Wang, A. Perrotta, S. Choi, S. Graham, G.C. Bazan, T.-Q. Nguyen, S.R. Marder & B. Kippelen, *Solution-based electrical doping of semiconducting polymer films over a limited depth*. Nature Materials, 2017. **16**: p. 474-480.

[6] V. A. Kolesov, B. Kippelen, N. Aizawa, S. R, Marder, C. Fuentes-Hernandez, J. Kido, **F. A. Larrain**, W.-F. Chou, *Devices with Organic Semiconductor Layers*

Electrically-Doped Over a Controlled Depth. Patent Application PCT/US16/35790, application number 15/735,549. Filed on June 3, 2016.

[7] S. Choi, C. Fuentes-Hernandez, C.-Y. Wang, T.M. Khan, **F.A. Larrain**, Y. Zhang, S. Barlow, S.R. Marder & B. Kippelen, *A Study on Reducing Contact Resistance in Solution-Processed Organic Field-Effect Transistors*. ACS applied materials & interfaces, 2016. **8**(37): p. 24744–24752.

[8] S. Choi, **F.A. Larrain**, C.-Y. Wang, C. Fuentes-Hernandez, W.-F. Chou & B. Kippelen, *Self-forming electrode modification in organic field-effect transistors*. Journal of Materials Chemistry C, 2016. **4**: p. 8297-8303.

APPENDIX A.

Table A-1. Hansen solubility parameters of various solvents.

	Hansen Space (as in HsPiP 5.0.04)				NFPA 704		
Solvent	δD	δP	δH	Distance to NM	Health	Flammability	Instability
Nitromethane (NM)	15.8	18.8	6.1	-	2	3	4
Acetonitrile	15.3	18	6.1	1.28	2	3	0
Dimethyl sulfoxide	18.4	16.4	10.2	7.04	2	2	0
Dimethylformamide	17.4	13.7	11.3	7.96	2	2	0
2-methoxyethanol	16	8.2	15	13.85	3	2	2
2-propanol	15.8	6.1	16.4	16.35	1	2	1
Ethanol	15.8	8.8	19.4	16.64	2	3	0

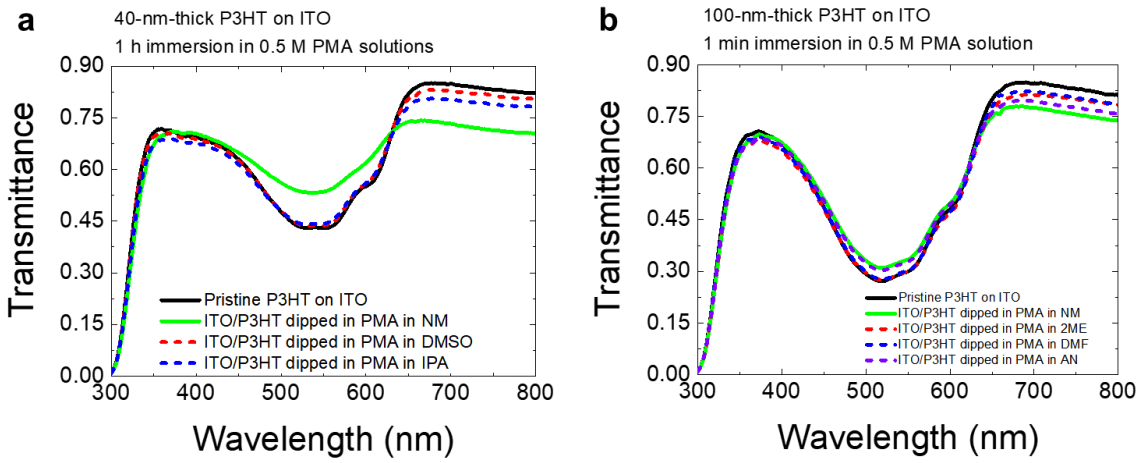

Figure A-1. Spectroscopic transmittance spectra of P3HT dipped in PMA solutions. (a) 40 nm- thick P3HT films immersed for 1 h into PMA dissolved in various solvents. (b) 100 nm-thick P3HT films immersed for 1 min into PMA dissolved in various solvents.

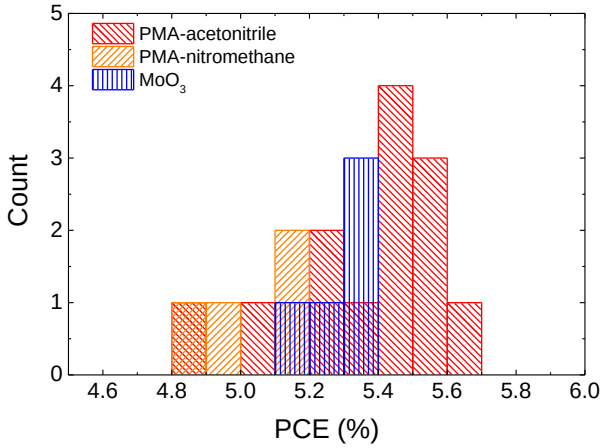

Figure A-2. Histogram of OPV's PCE, comparing doping with PMA in acetonitrile or PMA in nitromethane with the use of MoO_3.

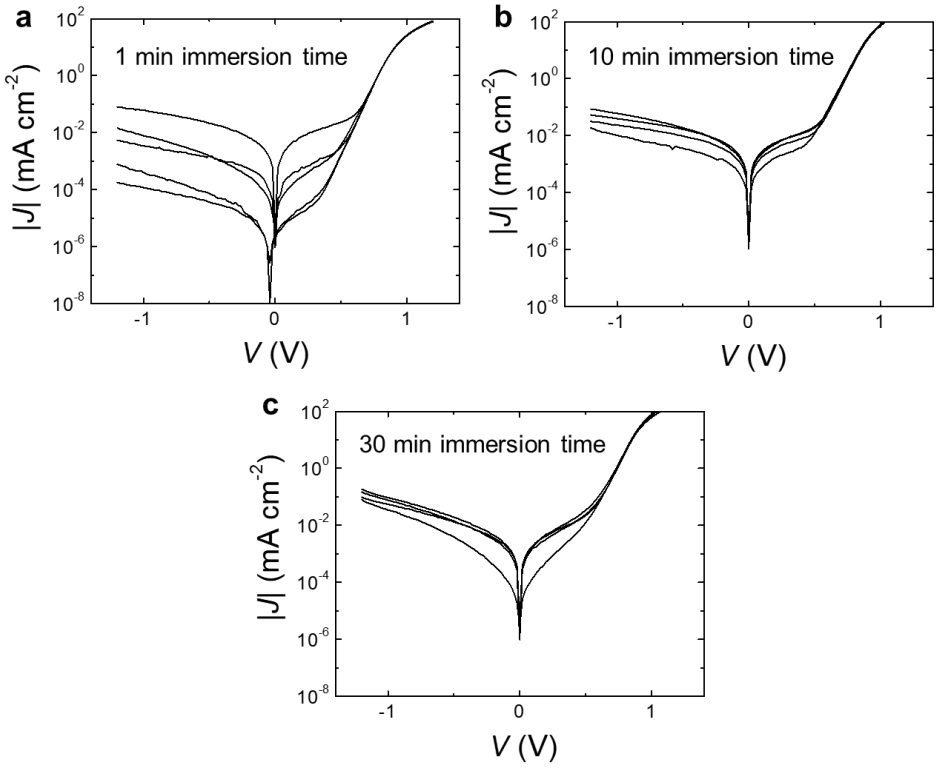

Figure A-3. *J-V* characteristics of OPV devices doped with PMA-acetonitrile for various times measured in the dark and at room temperature.

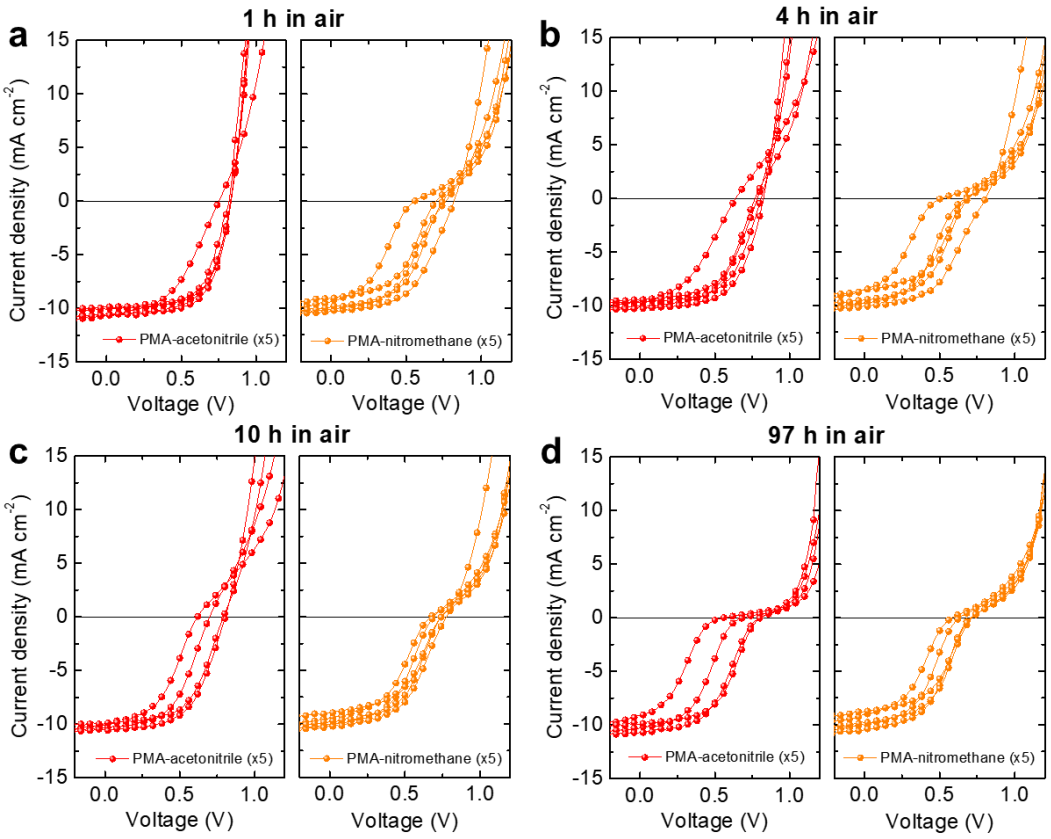

Figure A-4. *J-V* characteristics of OPV devices doped with PMA-acetonitrile or PMA-nitromethane, measured under 1-sun illumination, after air exposure.

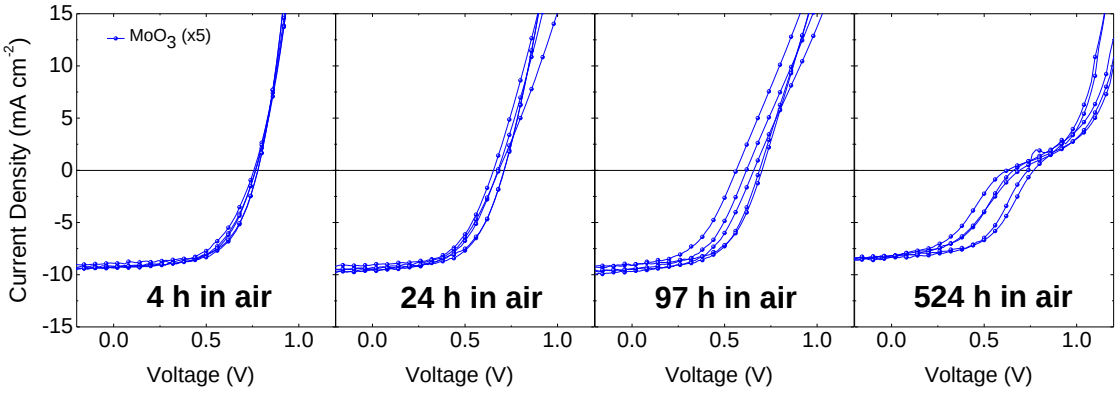

Figure A-5. *J-V* characteristics of OPV devices with a 10 nm-thick MoO_3 layer to favor hole collection measured under 1-sun illumination after air exposure.

APPENDIX B.

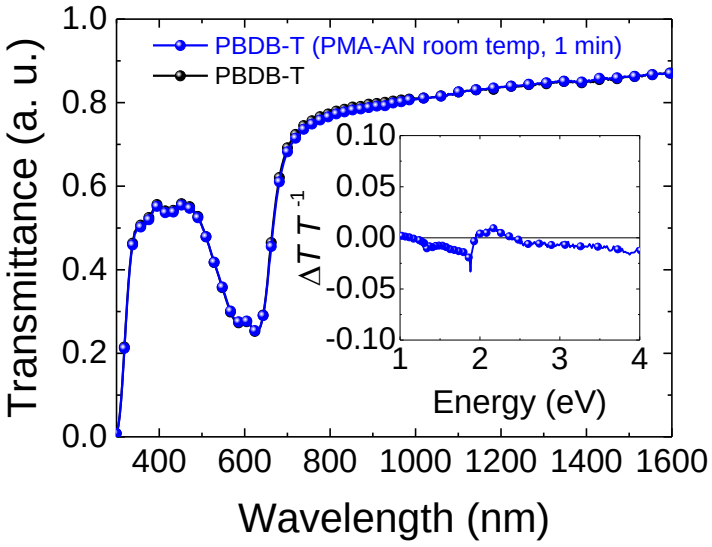

Figure B-1. Transmittance and WF changes of a PBDB-T film after immersion into a 0.5 M PMA-acetonitrile solution at room temperature for 1 min.

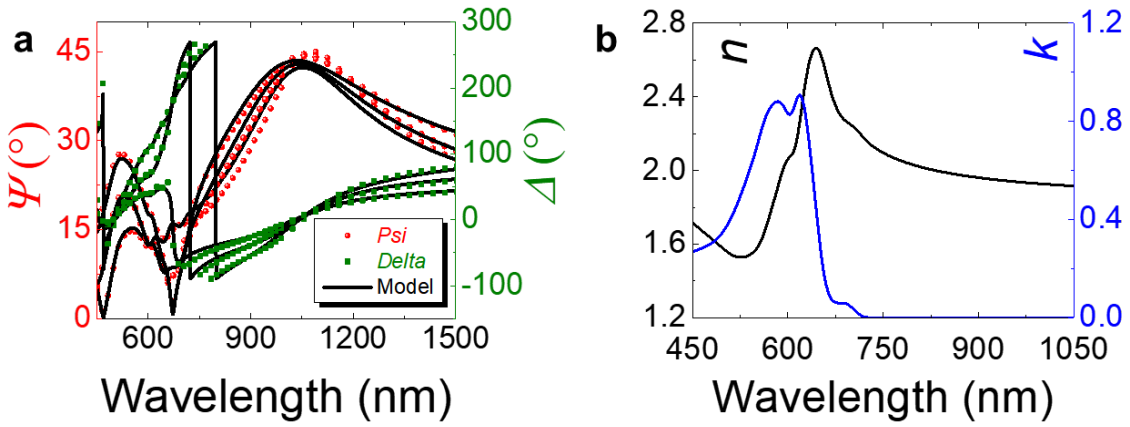

Figure B-2. (a) Ellipsometry measurements of a film of PBDB-T on glass. (b) Optical constants modeled using variable angle spectroscopic ellipsometry.

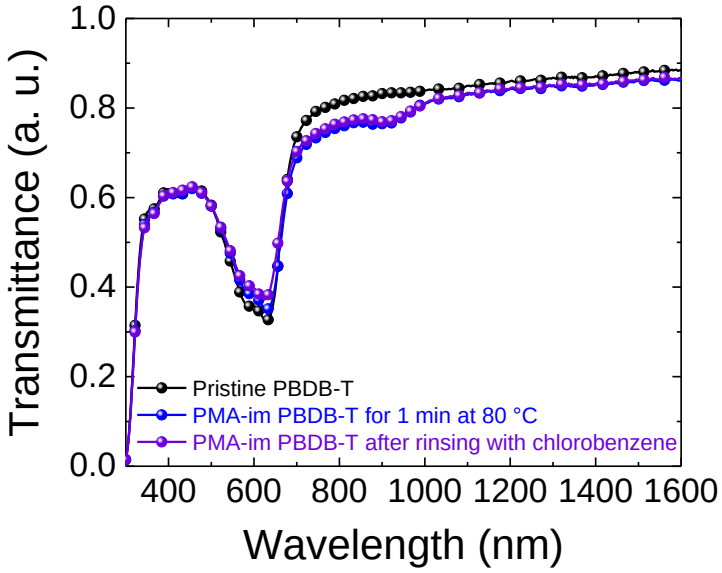

Figure B-3. Reduction of solubility to chlorobenzene of a PBDB-T film immersed into PMA-acetonitrile at 80 ºC for 1 min.

REFERENCES

[1] IEA (2018), World Energy Outlook 2018, Paris, https://www.iea.org/reports/world-energy-outlook-2018

[2] Haegel, N.M., et al., *Terawatt-scale photovoltaics: Transform global energy*. Science, 2019. **364**(6443), p. 836-838.

[3] UNCC. *Status of ratification of the Paris agreement*. 2020 [cited 2020 June 8th]; Available from: https://unfccc.int/process/the-paris-agreement/status-of-ratification.

[4] Haegel, N.M., et al., *Terawatt-scale photovoltaics: trajectories and challenges.* Science, 2017. **356**(6334), p. 141-143.

[5] Becquerel, A.E., *Recherches sur les effets de la radiation chimique de la lumiere solaire au moyen des courants electriques.* Comptes Rendus de L´Academie des Sciences, 1839. **9**, p. 145-149.

[6] Becquerel, A.E., *Memoire sur les Effects d'Electriques Produits Sous l'Influence des Rayons Solaires.* Comptes Rendus de l'Academie des Sciences, 1839. **9**, p. 561-567.

[7] Adams, W.G. and R.E. Day, *The Action of Light on Selenium.* Proceedings of the Royal Society of London, 1877. **25**, p. 113-117.

[8] Chapin, D.M., C.S. Fuller, and G.L. Pearson, *A new silicon p-n junction photocell for converting solar radiation into electrical power.* Journal of Applied of Physics, 1954. **25**, p. 676-677.

[9] NREL (2020), Best research-cell efficiency chart, Denver, https://www.nrel.gov/pv/cell-efficiency.html

[10] Green, M.A., A. Ho-Baillie, and H.J. Snaith, *The emergence of perovskite solar cells.* Nature Photonics, 2014. **8**(7), p. 506-514.

[11] FirstSolar. *First Solar Series 6*. 2020 [cited 2020 June 8th]; Available from: http://www.firstsolar.com/-/media/First-Solar/Technical-Documents/Series-6-Datasheets/Series-6-Datasheet.ashx.

[12] Heliatek. [cited 2020 June 8th]; Available from: heliatek.com.

[13] InfinityPV. [cited 2020 June 8th]; Available from: infinitypv.com.

[14] RaynergyTek. [cited 2020 June 8th]; Available from: raynergytek.com.

[15] Solar, M.-K. [cited 2020 June 8th]; Available from: m-kopa.com.

[16] SolarWindow. [cited 2020 June 8th]; Available from: solarwindow.com.

[17] Tang, C.W., *Two-layer organic photovoltaic cell.* Applied Physics Letters, 1986. **48**(2), p. 183-185.

[18] Espinosa, N., et al., *Solar cells with one-day energy payback for the factories of the future.* Energy & Environmental Science, 2012. **5**(1), p. 5117-5132.

[19] Darling, S.B. and F. You, *The case for organic photovoltaics.* RSC Advances, 2013. **3**(39), p. 17633-17648.

[20] Ostfeld, A.E. and A.C. Arias, *Flexible photovoltaic power systems: integration opportunities, challenges and advances.* Flexible and Printed Electronics, 2017. **2**(1):013001, p. 1-24.

[21] Zamarayeva, A.M., et al., *Flexible and stretchable power sources for wearable electronics.* Science Advances, 2017. **3**(6):e1602051, p. 1-10.

[22] Mathews, I., et al., *Technology and Market Perspective for Indoor Photovoltaic Cells.* Joule, 2019. **3**(6), p. 1415-1426.

[23] Chang, S.-Y., et al., *Transparent Polymer Photovoltaics for Solar Energy Harvesting and Beyond.* Joule, 2018. **2**(6), p. 1039-1054.

[24] Krebs, F.C., et al., *Manufacture, integration and demonstration of polymer solar cells in a lamp for the "Lighting Africa" initiative.* Energy & Environmental Science, 2010. **3**(5), p. 512-525.

[25] Woodyard, J.R., *Nonlinear circuit device utilizing germanium*, U.S. Patent 2,530,110, Nov. 14, 1950.

[26] Sparks, M. and G.K. Teal, *Method of making p-n junctions in semiconductor materials*, U.S. Patent 2,631,356, March 17, 1953.

[27] Chizinsky, G., B. Farms, and E. Simon, *Controlled doping of semiconductors*, U.S. Patent 3,574,009, April 6, 1971.

[28] Shirakawa, H., et al., *Synthesis of electrically conducting organic polymers: halogen derivatives of polyacetylene, (CH)x.* Journal of the Chemical Society, Chemical Communications, 1977. **474**, p. 578-580.

[29] Basescu, N., et al., *High electrical conductivity in doped polyacetylene.* Nature, 1987. **327**, p. 403-405.

[30] Genies, E.M. and A.A. Syed, *Polypyrrole and poly-N-methylpyrrole - an electrochemical study in aqueous medium.* Synthetic metals, 1984. **10**, p. 21-30.

[31] Kobayashi, M., et al., *The electronic and electrochemical properties of poly(isothianaphthene).* The Journal of Chemical Physics, 1985. **82**(12), p. 5717-5723.

[32] Macdiarmid, A.G., et al., *"Polyaniline": Interconversion of Metallic and Insulating Forms.* Molecular Crystals and Liquid Crystals, 1985. **121**, p. 173-180.

[33] Sato, M.-a., S. Tanaka, and K. Kaeriyama, *Soluble conducting polythiophenes.* Journal of the Chemical Society, Chemical Communications, 1986. **235**, p. 873-874.

[34] Frommer, J.E. and R.L. Elsenbaumer, *Simultaneous polymerization, doping and solubilization of heterocyclic polymers, solutions and cast articles*, U.S. Patent 4,599,194, July 8, 1986.

[35] Jen, K.-Y.A. and R.L. Elsenbaumer, *Solution processible forms of neutral and electrically conductive poly(substituted heterocycles)*, U.S. Patent 4,711,742, Dec. 8, 1987.

[36] Barlow, S., et al., *Electrical Doping of Organic Semiconductors with Molecular Oxidants and Reductants*, in *Conjugated Polymers: Properties, Processing, and Applications*, J.R. Reynolds, B.C. Thompson, and T.A. Skotheim, Editors. 2019, CRC Press.

[37] Olthof, S., et al., *Ultralow doping in organic semiconductors: evidence of trap filling.* Physical Review Letters, 2012. **109**(17):176601, p. 1-5.

[38] Kao, K.C., *Dielectric Phenomena in Solids*. 2004: Academic Press. 579.

[39] Hwang, J., A. Wan, and A. Kahn, *Energetics of metal–organic interfaces: New experiments and assessment of the field.* Materials Science and Engineering: R: Reports, 2009. **64**, p. 1-31.

[40] So, F., et al. *A comprehensive and unified picture of energy level alignment at interfaces with organic semiconductors*, in *SPIE Organic Photonics + Electronics*. 2016. San Diego, California.

[41] Jacobs, I.E. and A.J. Moule, *Controlling Molecular Doping in Organic Semiconductors.* Advanced Materials, 2017. **29**(42):1703063, p. 1-39.

[42] Pingel, P. and D. Neher, *Comprehensive picture of p-type doping of P3HT with the molecular acceptor F4TCNQ.* Physical Review B, 2013. **87**(11):115209, p. 1-9.

[43] Koech, P.K., et al., *Synthesis and Application of 1,3,4,5,7,8-Hexafluorotetracyanonaphthoquinodimethane (F6-TNAP): A Conductivity Dopant for Organic Light-Emitting Devices.* Chemistry of Materials, 2010. **22**(13), p. 3926-3932.

[44] Mendez, H., et al., *Charge-transfer crystallites as molecular electrical dopants.* Nature Communications, 2015. **6**:8560, p. 1-11.

[45] Zhang, F. and A. Kahn, *Investigation of the High Electron Affinity Molecular Dopant F6-TCNNQ for Hole-Transport Materials.* Advanced Functional Materials, 2018. **28**(1):1703780.

[46] Tietze, M.L., et al., *Fermi level shift and doping efficiency in p-doped small molecule organic semiconductors: A photoelectron spectroscopy and theoretical study.* Physical Review B, 2012. **86**(3):035320, p. 1-12.

[47] Mendez, H., et al., *Doping of organic semiconductors: impact of dopant strength and electronic coupling.* Angewandte Chemie International Edition, 2013. **52**(30), p. 7751-7755.

[48] Salzmann, I., et al., *Molecular Electrical Doping of Organic Semiconductors: Fundamental Mechanisms and Emerging Dopant Design Rules.* Accounts of Chemical Research, 2016. **49**(3), p. 370-378.

[49] Würfel, P., *Physics of solar cells: from principles to new concepts*. 2005: Wiley-VCH Verlag GmbH & Co. KGaA, Weinheim. 186.

[50] Kahn, A., *Fermi level, work function and vacuum level.* Materials Horizons, 2016. **3**(1), p. 7-10.

[51] Hill, T.L., *An introduction to statistical thermodynamics*. 1986, New York: Dover Publications, Inc. 544.

[52] Oehzelt, M., N. Koch, and G. Heimel, *Organic semiconductor density of states controls the energy level alignment at electrode interfaces.* Nature Communications, 2014. **5**:4174, p. 1-8.

[53] Yang, J.-P., et al., *Origin and role of gap states in organic semiconductor studied by UPS: as the nature of organic molecular crystals.* Journal of Physics D: Applied Physics, 2017. **50**(42):423002, p. 1-45.

[54] Akaike, K., *Advanced understanding on electronic structure of molecular semiconductors and their interfaces.* Japanese Journal of Applied Physics, 2018. **57**(3S2):03EA03, p. 1-16.

[55] Brédas, J.-L., et al., *Molecular understanding of organic solar cells: the challenges.* Accounts of Chemical Research, 2009. **42**(11), p. 1691-1699.

[56] Kippelen, B. and J.-L. Brédas, *Organic photovoltaics.* Energy & Environmental Science, 2009. **2**(3), p. 251-261.

[57] Coropceanu, V., et al., *Charge-transfer electronic states in organic solar cells.* Nature Reviews Materials, 2019. **4**, p. 689-707.

[58] Pope, M.T. and A. Muller, *Polyoxometalate chemistry: an old field with new dimensions in several disciplines.* Angewandte Chemie International Edition, 1991. **30**, p. 34-48.

[59] Adamczyk, L., et al., *Effective Charge Transport in Poly(3,4-ethylenedioxythiophene) Based Hybrid Films Containing Polyoxometallate Redox Centers.* Journal of the Electrochemical Society, 2005. **152**(3), p. E98-E103.

[60] Gómez-Romero, P., et al., *Hybrid organic–inorganic nanocomposite materials for application in solid state electrochemical supercapacitors.* Electrochemistry Communications, 2003. **5**(2), p. 149-153.

[61] Otero, T.F., S.A. Cheng, and F. Huerta, *Hybrid Materials Polypyrrole/PW12O403-. 1. Electrochemical Synthesis, Kinetics and Specific Charges.* Journal of Physical Chemistry B, 2000. **104**, p. 10522-10527.

[62] Zhu, Y., et al., *A cost-effective commercial soluble oxide cluster for highly efficient and stable organic solar cells.* Journal of Material Chemistry A, 2014. **2**(5), p. 1436-1442.

[63] Palilis, L.C., et al., *Solution processable tungsten polyoxometalate as highly effective cathode interlayer for improved efficiency and stability polymer solar cells.* Solar Energy Materials and Solar Cells, 2013. **114**, p. 205-213.

[64] Alaaeddine, M., et al., *Enhancement of photovoltaic efficiency by insertion of a polyoxometalate layer at the anode of an organic solar cell.* Inorganic Chemistry Frontiers, 2014. **1**(9), p. 682-688.

[65] Jia, X., et al., *Highly efficient low-bandgap polymer solar cells with solution-processed and annealing-free phosphomolybdic acid as hole-transport layers.* ACS Applied Materials & Interfaces, 2015. **7**(9), p. 5367-5372.

[66] Vasilopoulou, M., et al., *Annealing-free highly crystalline solution-processed molecular metal oxides for efficient single-junction and tandem polymer solar cells.* Energy & Environmental Science, 2015. **8**, p. 2448-2463.

[67] Aizawa, N., et al., *Simultaneous cross-linking and p-doping of a polymeric semiconductor film by immersion into a phosphomolybdic acid solution for use in organic solar cells.* Chemical Communications, 2016. **52**(19), p. 3825-3827.

[68] Kolesov, V.A., et al., *Solution-based electrical doping of semiconducting polymer films over a limited depth.* Nature Materials, 2017. **16**(4), p. 474-480.

[69] Smits, F.M., *Measurement of Sheet Resistivities with the Four-point Probe.* The Bell System Technical Journal, 1957. p. 711-718.

[70] Ilavsky, J., *Nika: software for two-dimensional data reduction.* Journal of Applied Crystallography, 2012. **45**(2), p. 324-328.

[71] Oosterhout, S.D., et al., *Mixing Behavior in Small Molecule:Fullerene Organic Photovoltaics.* Chemistry of Materials, 2017. **29**(7), p. 3062-3069.

[72] Lu, C.-K. and H.-F. Meng, *Hole doping by molecular oxygen in organic semiconductors: Band-structure calculations.* Physical Review B, 2007. **75**(23):235206, p. 1-6.

[73] Heimel, G., et al., *Design of Organic Semiconductors from Molecular Electrostatics.* Chemistry of Materials, 2011. **23**(3), p. 359-377.

[74] Duong, D.T., et al., *The chemical and structural origin of efficient p-type doping in P3HT.* Organic Electronics, 2013. **14**(5), p. 1330-1336.

[75] Lussem, B., et al., *Doped Organic Transistors.* Chemical Reviews, 2016. **116**(22), p. 13714-13751.

[76] Dai, A., et al., *Investigation of p-dopant diffusion in polymer films and bulk heterojunctions: Stable spatially-confined doping for all-solution processed solar cells.* Organic Electronics, 2015. **23**, p. 151-157.

[77] Wang, C., et al., *Optical measurement of doping efficiency in poly(3-hexylthiophene) solutions and thin films.* Physical Review B, 2015. **91**(8):085205, p. 1-7.

[78] Li, J., et al., *Measurement of Small Molecular Dopant F4TCNQ and C60F36 Diffusion in Organic Bilayer Architectures.* ACS Appl Mater Interfaces, 2015. **7**(51), p. 28420-28428.

[79] Walzer, K., et al., *Highly Efficient Organic Devices Based on Electrically Doped Transport Layers.* Chemical Reviews, 2007. **107**, p. 1233−1271.

[80] Lim, K.-G., et al., *Universal energy level tailoring of self-organized hole extraction layers in organic solar cells and organic–inorganic hybrid perovskite solar cells.* Energy & Environmental Science, 2016. **9**(3), p. 932-939.

[81] Kim, H., et al., *On-Fabrication Solid-State N-Doping of Graphene by an Electron-Transporting Metal Oxide Layer for Efficient Inverted Organic Solar Cells.* Advanced Energy Materials, 2016. **6**(12):1600172, p. 1-8.

[82] Gao, W. and A. Kahn, *Controlled p doping of the hole-transport molecular material N,N′-diphenyl-N,N′-bis(1-naphthyl)-1,1′-biphenyl-4,4′-diamine with tetrafluorotetracyanoquinodimethane.* Journal of Applied Physics, 2003. **94**(1), p. 359-366.

[83] Chan, C.K., et al., *Decamethylcobaltocene as an efficient n-dopant in organic electronic materials and devices.* Organic Electronics, 2008. **9**(5), p. 575-581.

[84] Kröger, M., et al., *P-type doping of organic wide band gap materials by transition metal oxides: A case-study on molybdenum trioxide.* Organic Electronics, 2009. **10**(5), p. 932-938.

[85] Qi, Y., et al., *A Molybdenum Dithiolene Complex asp-Dopant for Hole-Transport Materials: A Multitechnique Experimental and Theoretical Investigation.* Chemistry of Materials, 2010. **22(**2), p. 524-531.

[86] Qi, Y., et al., *Solution doping of organic semiconductors using air-stable n-dopants.* Applied Physics Letters, 2012. **100**(8):083305, p. 1-4.

[87] Guo, S., et al., *n-Doping of Organic Electronic Materials using Air-Stable Organometallics.* Advanced Materials, 2012. **24**(5), p. 699-703.

[88] Fuzell, J., et al., *Optical Dedoping Mechanism for P3HT:F4TCNQ Mixtures.* The Journal Of Physical Chemistry Letters, 2016. **7**(21), p. 4297-4303.

[89] Li, J., et al., *The effect of thermal annealing on dopant site choice in conjugated polymers.* Organic Electronics, 2016. **33**, p. 23-31.

[90] Jacobs, I.E., et al., *Direct-Write Optical Patterning of P3HT Films Beyond the Diffraction Limit.* Advanced Materials, 2017. **29(**2):1603221, p. 1-8.

[91] Po, R., et al., *From lab to fab: how must the polymer solar cell materials design change? – an industrial perspective.* Energy & Environmental Science, 2014. **7**(3), p. 925-943.

[92] Zhang, S., et al., *Green-solvent-processable organic solar cells.* Materials Today, 2016. **19**(9), p. 533-543.

[93] Brown, P.J., et al., *Optical spectroscopy of field-induced charge in self-organized high mobility poly(3-hexylthiophene).* Physical Review B, 2001. **63(**12):125204, p. 1-11.

[94] Brown, P.J., et al., *Effect of interchain interactions on the absorption and emission of poly(3-hexylthiophene).* Physical Review B, 2003. **67**(6):064203, p. 1-16.

[95] Verploegen, E., et al., *Effects of Thermal Annealing Upon the Morphology of Polymer-Fullerene Blends.* Advanced Functional Materials, 2010. **20**(20), p. 3519-3529.

[96] Proctor, C.M. and T.-Q. Nguyen, *Effect of leakage current and shunt resistance on the light intensity dependence of organic solar cells.* Applied Physics Letters, 2015. **106**(8):083301, p. 1-4.

[97] Zhou, Y., et al., *Direct correlation between work function of indium-tin-oxide electrodes and solar cell performance influenced by ultraviolet irradiation and air exposure.* Physical Chemistry Chemical Physics, 2012. **14(**34), p. 12014-12021.

[98] Sirringhaus, H., et al., *Two-dimensional charge transport in self-organized, high-mobility conjugated polymers.* Letters to Nature, 1999. **401**, p. 685-688.

[99] Murrey, T.L., et al., *Additive solution deposition of multi-layered semiconducting polymer films for design of sophisticated device architectures.* Journal of Materials Chemistry C, 2019. **7**(4), p. 953-960.

[100] Kido, J. and T. Matsumoto, *Bright organic electroluminescent devices having a metal-doped electron-injecting layer*. Applied Physics Letters, 1998. **73**(20), p. 2866-2868.

[101] Blochwitz, J., et al., *Low voltage organic light emitting diodes featuring doped phthalocyanine as hole transport material.* Applied Physics Letters, 1998. **73**(6), p. 729-731.

[102] Tiwari, S.P., et al., *Pentacene organic field-effect transistors with doped electrode-semiconductor contacts.* Organic Electronics, 2010. **11**(5), p. 860-863.

[103] Singh, S., et al., *Reduction of contact resistance by selective contact doping in fullerene n-channel organic field-effect transistors.* Applied Physics Letters, 2013. **102**(15):153303, p. 1-4.

[104] Choi, S., et al., *A Study on Reducing Contact Resistance in Solution-Processed Organic Field-Effect Transistors.* ACS Applied Materials & Interfaces, 2016. **8**(37), p. 24744-24752.

[105] Quinn, J.T.E., et al., *Recent progress in the development of n-type organic semiconductors for organic field effect transistors.* Journal of Materials Chemistry C, 2017. **5**(34), p. 8654-8681.

[106] Lin, X., et al., *Beating the thermodynamic limit with photo-activation of n-doping in organic semiconductors.* Nature Materials, 2017. **16**(12), p. 1209-1215.

[107] Maennig, B., et al., *Organic p-i-n solar cells.* Applied Physics A: Materials Science & Processing, 2004. **79**(1), p. 1-14.

[108] Chan, C.K., et al., *Influence of chemical doping on the performance of organic photovoltaic cells.* Applied Physics Letters, 2009. **94**(20):203306, p. 1-3.

[109] Dai, A., et al., *Enhanced Charge-Carrier Injection and Collection Via Lamination of Doped Polymer Layers p-Doped with a Solution-Processible Molybdenum Complex.* Advanced Functional Materials, 2014. **24**(15), p. 2197-2204.

[110] Veysel Tunc, A., et al., *Molecular doping of low-bandgap-polymer:fullerene solar cells: Effects on transport and solar cells.* Organic Electronics, 2012. **13**(2), p. 290-296.

[111] Zhang, Y., et al., *Molecular doping enhances photoconductivity in polymer bulk heterojunction solar cells.* Advanced Materials, 2013. **25**(48), p. 7038-7044.

[112] Reiser, P., et al., *Dopant Diffusion in Sequentially Doped Poly(3-hexylthiophene) Studied by Infrared and Photoelectron Spectroscopy.* The Journal of Physical Chemistry C, 2018. **122**(26), p. 14518-14527.

[113] Saska, J., et al., *A Freely Soluble, High Electron Affinity Molecular Dopant for Solution Processing of Organic Semiconductors.* Chemistry of Materials, 2019. **31**(5), p. 1500-1506.

[114] Rocchiccioli-Deltcheff, C., et al., *Catalysis by 12-Molybdophosphates.* Journal of Catalysis, 1996. **164**(0358), p. 16-27.

[115] Sadakane, M. and E. Steckhan, *Electrochemical properties of polyoxometalates as electrocatalyst.* Chemical Reviews, 1998. **98**(1), p. 219-237.

[116] Rocchiccioli-Deltcheff, C. and M. Fournier, *Catalysis by Polyoxometalates.* Journal of the Chemical Society, Faraday Transactions, 1991. **87**(24), p. 3913-3920.

[117] Vidoeski, B., et al., *Raman study of the interactions between highly ordered pyrolytic graphite (HOPG) and polyoxometalates: The effects of acid concentration.* Journal of the Serbian Chemical Society, 2016. **81**(7), p. 777-787.

[118] Chang, Y.-M., W.-F. Su, and L. Wang, *Influence of photo-induced degradation on the optoelectronic properties of regioregular poly(3-hexylthiophene).* Solar Energy Materials and Solar Cells, 2008. **92**(7), p. 761-765.

[119] Tamanai, A., S. Beck, and A. Pucci, *Mid-infrared characterization of thiophene-based thin polymer films.* Displays, 2013. **34**(5), p. 399-405.

[120] V. Molefe, F., et al., *Spectroscopic investigation of charge and energy transfer in P3HT/GO nanocomposite for solar cell applications.* Advanced Materials Letters, 2017. **8**(3), p. 246-250.

[121] Leng, C.Z. and M.D. Losego, *Vapor phase infiltration (VPI) for transforming polymers into organic–inorganic hybrid materials: a critical review of current progress and future challenges.* Materials Horizons, 2017. **4**(5), p. 747-771.

[122] Franeker, J.J., et al., *Depositing Fullerenes in Swollen Polymer Layers via Sequential Processing of Organic Solar Cells.* Advanced Energy Materials, 2015. **5**(14):1500464, p. 1-10.

[123] Cho, Y., et al., *Ternary Organic Photovoltaics Prepared by Sequential Deposition of Single Donor and Binary Acceptors.* ACS Applied Materials & Interfaces, 2018. **10**(33), p. 27757-27763.

[124] Cui, Y., et al., *Over 16% efficiency organic photovoltaic cells enabled by a chlorinated acceptor with increased open-circuit voltages.* Nature Communications, 2019. **10**(1):2515, p. 1-8.

[125] Fan, B., et al., *Achieving over 16% efficiency for single-junction organic solar cells.* Science China Chemistry, 2019. **62**(6), p. 746-752.

[126] Yuan, J., et al., *Single-Junction Organic Solar Cell with over 15% Efficiency Using Fused-Ring Acceptor with Electron-Deficient Core.* Joule, 2019. **3**(4), p. 1140-1151.

[127] Liu, Q., et al., *18% Efficiency organic solar cells.* Science Bulletin, 2020. **65**(4), p. 272-275.

[128] Lucera, L., et al., *Printed semi-transparent large area organic photovoltaic modules with power conversion efficiencies of close to 5 %.* Organic Electronics, 2017. **45**, p. 209-214.

[129] Maisch, P., et al., *Shy Organic Photovoltaics: Digitally Printed Organic Solar Modules With Hidden Interconnects.* Solar RRL, 2018. **2**(7):1800005, p. 1-9.